Time resolved temperature and pressure based methodology for direct and indirect combustion noise separation

Wenjie Tao

NNT : 2016SACLC009

THÈSE DE DOCTORAT DE L'UNIVERSITÉ PARIS-SACLAY

préparée à CentraleSupélec

ÉCOLE DOCTORALE N°579
Sciences mécaniques et énergétiques, matériaux et géosciences.

Spécialité Combustion.

présentée par

Wenjie TAO

Time resolved temperature and pressure based methodology for direct and indirect combustion noise separation

Méthodologie pour la séparation du bruit direct et indirect de combustion basée sur les mesures de température et de pression résolues dans le temps

Thèse soutenue à Châtenay-Malabry le 25 janvier 2016

Composition du jury:

M. Franck NICOUD	Université de Montpellier	Président du jury
M. Christophe BAILLY	Ecole Centrale de Lyon	Rapporteur
M. Frank SIMON	ONERA Toulouse	Rapporteur
M. Friedrich BAKE	DLR	Examinateur
M. François VUILLOT	ONERA Châtillon	Examinateur
M. Sébastien DUCRUIX	CNRS	Co-encadrant de thèse
M. Thierry SCHULLER	Ecole Centrale Paris	Co-encadrant de thèse
M. Franck RICHECOEUR	Ecole Centrale Paris	Directeur de thèse

Laboratoire d'Érgétique Moléculaire et Macroscopique, Combustion, CNRS, CentraleSupélec.

Abstract

The present work addresses the question of indirect combustion noise measurement. Indirect combustion noise is generated by the acceleration of entropy waves in the final part of combustion chambers where the cross section area decreases due to the presence of a nozzle or turbine blades. Practically, this noise coexists with the direct noise emitted by the flame heat release oscillations. The challenge addressed here is the development of a practical strategy to quantify experimentally indirect noise and to discriminate it from direct noise. The configuration retained for the study is a test bench with a converging-diverging nozzle. The indirect noise generation is located at the nozzle so that the strategy relies on nozzle transfer functions. The first chapter defines the nozzle transfer functions used in the study and makes connections with existing literature about theoretical and numerical quantifications of them. The second chapter introduces the experimental configuration, called TAFG, developed to generate and measure coherent acoustic and entropic waves. This bench is used to validate the strategy in a situation with ideal signals generated by a loudspeaker. A parametric study is performed to evaluate the most appropriate operating point. Acoustic pressure is measured with microphones and entropy waves are recovered from temperature measurements. The third chapter details how the raw signals are decomposed to evaluate the incident pressure and entropy waves. The fourth chapter closes the first part of the study by describing the post-processing strategy then testing it on high-fidelity acoustic simulations and the TAFG bench. The second part focuses on the use of the post-processing technique to discriminate noise sources from Large Eddy Simulations of a turbulent combustion test bench operated at EM2C. The code AVBP is used for the simulation. Simulations are validated on experimental data then raw signals are processed to quantify the direct and indirect noise sources. The present study relies on theoretical, experimental and numerical investigations that, when put together, lead to an original strategy to separate direct and indirect noise from simple pressure and temperature measurements at the wall of any combustor.

Résumé

Les nuisances sonores émises par des moteurs aéronautiques, couramment désignées comme le bruit de moteur, est un enjeu environnemental de plus en plus préoccupant pour les riverains des aéroports. À cause de la forte croissance du transport aérien des passagers, de strictes réglementations sur les émissions sonores des avions ont été imposées aux aéroports ainsi qu'à l'industrie aéronautique.

Le bruit d'un moteur civil à réaction provient principalement de la soufflante, la chambre de combustion et le jet. Tandis qu'une réduction significative du bruit de jet et de soufflante a été atteinte, le bruit de combustion devient le bruit de fond qui empêche d'abaisser davantage du bruit de moteur.

La combustion contribue au bruit de moteur en termes de bruit direct et indirect. Le bruit direct est lié aux fluctuations de taux de dégagement de chaleur de la flamme. Ces fluctuations produisent également des inhomogénéités dans l'écoulement, par exemple les poches chaudes ou froides du à la combustion inhomogène, qui sont transportées par l'écoulement et peuvent être converties en bruit quand elles interagissent avec un gradient de vitesse généralement induit par des éléments à la sortie de la chambre de combustion tel qu'une tuyère. Ce mécanisme est appelé le bruit de combustion indirect.

Les contributions directes et indirectes du bruit de combustion coexistent dans de nombreuses applications et des activités de recherche ont été menées afin d'évaluer ces niveaux de bruit. Les approches analytiques et numériques ont permis de calculer ces deux types de contributions à partir des sources de bruit modélisées ou issues de la simulation numérique de combustion. Plusieurs résultats ont montré que le bruit de combustion direct est dominant dans le champ lointain, alors que le bruit de combustion indirect peut dominer le bruit direct dans le champ proche de la chambre de combustion. Cependant, peu d'études expérimentales ont été effectuées afin de discrimination les deux types de contributions.

Cette thèse a ainsi pour l'objective de développer une méthodologie expérimentale pour déterminer des contributions directes et indirectes du bruit de

combustion à partir de mesures simultanées des fluctuations de pression et de température. Elle consiste à déterminer les sources de bruit direct et indirect dans l'écoulement en amont de la tuyère ainsi que les fonctions de transfert de la tuyère. La méthodologie est d'abord validée à partir d'un cas numérique calculé par un code dédié, où une tuyère est soumise aux forçages simultanés d'une onde acoustique et d'une onde d'entropie. La validation est obtenue par la comparaison aux fonctions de transfert analytiques de la tuyère.

Un dispositif expérimental bien contrôlé qui génère simultanément des fluctuations de pression et de température sans introduire la combustion, appelé TAFG, est développé pour la validation expérimentale de la méthodologie. La TAFG fonctionne avec une configuration de *jet-in-crossflow*, où des jets chauds sont injectés transversalement dans l'écoulement principal à une température relativement basse par rapport à l'écoulement principal. Un haut-parleur est employé pour créer les fluctuations de pressions dans l'écoulement et ainsi faire varier la quantité de mouvement des jets. Ceci produit les fluctuations de température qui peuvent être l'origine du bruit indirect lorsque l'écoulement est accéléré dans un convergent à la sortie du TAFG.

Enfin, cette méthodologie est appliquée pour analyser les contributions directes et indirectes du bruit dans un cas plus complexe avec combustion. L'écoulement réactif dans un brûleur à l'échelle laboratoire équipé d'une tuyère amorcée à la sortie de la chambre de combustion a été résolu grâce à un code de simulation numérique aux grandes échelles AVBP. Les champs instantanés issus de la LES ont ensuite été post traités pour obtenir les signaux temporels de fluctuations de pressions et de température à la sortie de la chambre. Les signaux numériques à différentes positions le long de l'axe de la chambre ont été finalement analysés par la méthodologie proposée afin de déterminer les sources directes et indirectes du bruit ainsi que les fonctions de transfert de la tuyère.

Contents

Abstract iii

Résumé v

Nomenclature xix

Introduction 1

I Separation of entropy generated noise in an acoustically perturbed nozzle 15

1 Nozzle transfer functions 17
- 1.1 Analytical solutions of nozzle transfer functions . . . 17
  - 1.1.1 Compact nozzle without shock . . . 19
  - 1.1.2 Compact nozzle with shock . . . 21
- 1.2 Transfer transfer functions of a subsonic nozzle accounting for nozzle outlet impedances . . . 21
- 1.3 Effect of downstream boundary condition . . . 23

2 The Temperature and Acoustic Fluctuations Generator 27
- 2.1 Experimental setup . . . 27
  - 2.1.1 Working principle . . . 27
  - 2.1.2 Diagnostic techniques . . . 28
- 2.2 Setting up the frequency range . . . 31
- 2.3 Parametric study of TAFG performance . . . 35
  - 2.3.1 Influence of jets and mainstream mass flow rates . . . 36
  - 2.3.2 Influence of the modulation frequency . . . 39
- 2.4 Analytical ratio of indirect to direct noise level in the TAFG setup 39

3 Experimental methods for determining upstream waves 43
- 3.1 Procedure for reconstructing upstream perturbation variables . 44
- 3.2 Measurement of the reflection coefficient by Two- and Three-Microphone Method (TMM) . . . 45

3.2.1 Two-Microphone Method . . . 45
3.2.2 Three-Microphone Method . . . 47
3.3 Compensation of temperature fluctuations measurement by Two-Thermocouple Method (TTM) . . . 48
3.3.1 Review of previous works . . . 48
3.3.2 Estimation of time constants with the transfer function of thermocouples . . . 52
3.3.3 Reconstruction of temperature signals . . . 54
3.4 Determination of the upstream perturbation variables in the TAFG setup . . . 58

4 Separation of direct and indirect noise contributions 61
4.1 Separation method for direct and indirect noise contributions . 61
4.2 Numerical validation of the diff-R method by the SUNDAY code 64
4.2.1 Sensitivity to signal noise . . . 66
4.2.2 Effects of finite-amplitude convective velocity fluctuations 67
4.3 Experimental separation of indirect and direct nozzle reflection coefficients . . . 70
4.3.1 Operating conditions and measurement quality . . . 70
4.3.2 Measurement of the nozzle reflection coefficients with the diff-R method . . . 73
4.4 Conclusion . . . 73

II Analysis of combustion noise in a laboratory-scale burner using Large Eddy Simulation 77

5 LES of the CESAM-HP Burner 79
5.1 An introduction to Large Eddy Simulation . . . 79
5.2 Computational domain . . . 81
5.2.1 The CESAM-HP burner . . . 81
5.2.2 Computational domain and the unstructured mesh . . . 84
5.3 The LES code: AVBP . . . 86
5.3.1 Subgrid scale model (SGS) . . . 86
5.3.2 Combustion model . . . 86
5.3.3 Numerical method . . . 87
5.3.4 Boundary conditions . . . 87
5.3.4.1 General inlet, outlet and wall boundary conditions 87
5.3.4.2 Homogeneous coupled boundary condition for the perforated plate . . . 88
5.3.4.3 Heat loss on the combustion chamber walls . . 91

6 Numerical characterisation of the CESAM-HP burner 93
6.1 Overview of LES simulations . . . 93

6.2 Flow characterisation . . . 96
6.2.1 Non reacting flow velocity fields . . . 96
6.2.2 Reacting flow velocity fields . . . 97
6.2.3 Swirl number in reactive LES simulations . . . 98
6.3 Thermoacoustic characterisation . . . 101
6.4 Numerical analysis of the self-sustained combustion instability . 105
6.4.1 Intermittent flash back in the injector . . . 105
6.4.2 DMD analysis of LES fields . . . 108
6.4.2.1 Dynamic mode decomposition . . . 108
6.4.2.2 DMD results . . . 109
6.4.3 Conclusion . . . 109
6.5 Analysis of the temperature fields at the end of combustion chamber . . . 112
6.5.1 Time-resolved LES fields in the cross sections at the chamber-end . . . 112
6.5.2 Extraction of 1D time series . . . 113

7 Combustion noise analysis 117
7.1 From 2D LES fields to 1D time series . . . 117
7.2 Combustion noise analysis using LES simulations . . . 119
7.3 Combustion noise analysis with the diff-R method . . . 120
7.3.1 Computations of $\mathcal{R}$ and H_{sa} . . . 122
7.3.2 Determination of upstream acoustic and entropy waves . 123
7.3.3 Determination of indirect noise contribution . . . 123
7.4 Conclusion . . . 125

Conclusion 127

A Quasi-steady analysis of the TAFG setup 131

B Mesh size adaptation for the jet by a 2D LES test 135

C Linear acoustic analysis the CESAM-HP burner 139
C.1 Two-cavity model . . . 139
C.2 Five-cavity model . . . 141
C.3 Results and discussion . . . 142

References 154

List of Tables

2.1 Nozzle geometries 29
2.2 Optimised operation conditions of the TAFG setup 39

3.1 Estimation of time constants using signals at 10 Hz modulation 54
3.2 Input parameters for TTM reconstruction methods 56
3.3 Upstream perturbation variables at the inlet of the nozzle with the flow and modulation conditions 60

4.1 Inlet and outlet Mach numbers and the analytical direct and indirect nozzle reflection coefficient for the three operating conditions 70

5.1 CESAM-HP reactive operating conditions, mean pressure and temperature measured at axial position x_4 83
5.2 Experimental and numerical heat losses on the chamber walls for the operation condition op16-0-2-85 91

C.1 Chose operating point 143
C.2 Summary of acoustic modes obtained experimentally and analytically with the two-cavity and five-cavity models 143
C.3 Interpretation of acoustic modes 143

List of Figures

1 Aircraft noise sources breakdown (Dobrzynski 2010) 1
2 Typical turbofan noise contribution and noise spectrum (Sensiau 2013) 2
3 Typical breakdown of turbofan noise sources between 2000 and 2025 (Sensiau 2013) 2

1.1 Schematic view of the reflection and transmission of acoustic and entropy waves when they enter the nozzle. Constant cross section zones are delimited by vertical line. The second subscripts u, d, s in wave notations stand for respectively the contributions to the sound field due to the incident acoustic wave from upstream, the incident acoustic wave from downstream and the entropy wave. 20
1.2 Schematic view of forced response of nozzle with shock 22
1.3 Waves in ducted system with a nozzle 22
1.4 Evolution of $\mathcal{R}_a, \mathcal{T}_a, \mathcal{R}_s$ and $\mathcal{T}_s$ as a function of frequency for three different downstream boundary conditions. Blue line: anechoic termination; Green line: open pipe termination with $L =$ 126.5 mm; Red line: open pipe termination with $L = 0$ mm. . . 25

2.1 Components of the temperature and acoustic fluctuation generator (TAFG) 29
2.2 Pressure and temperature sensors 30
2.3 Position of measurements. The grey area corresponds to the numerical calculation domain for the code SUNDAY 30
2.4 Signals of the dynamic pressure, velocity and temperature . . . 32
2.5 Schematic view of the experimental configuration to measure $\mathcal{R}_a$ and R_L 33
2.6 Experimental (symbols) and analytical (black-line) reflection coefficients R_L and $\mathcal{R}_a$ for frequencies between 10 and 1000 Hz of the nozzle D06 extended by a 126.5 mm duct. The analytical value of $\mathcal{R}_a$ is obtained using the experimentally determined R_L. 34
2.7 Root-mean-square of temperature fluctuations as a function of the mass flow rate of the mainstream $\dot{m}_1$ and the jets $\dot{m}_2$. $f =$ 10 Hz. Nozzle D12. 37

2.8 Evolution of the mean temperature as a function of the jet-to-maintream mass flow rate ratio. $f = 10$ Hz. Nozzle D12. 37
2.9 Influence of the jet-to-maintream mass flow rate ratio $\dot{m}_2/\dot{m}_1$ on the normalised amplitude of temperature fluctuations. $f =$ 10 Hz. Nozzle D12. 37
2.10 Influence of the mean flow velocity on the normalised amplitude of temperature fluctuations at constant jet-to-maintream mass flow rate ratio. $f = 10$ Hz. Nozzle D12. 37
2.11 Root-mean-square temperature fluctuations T_{rms} and modulation level $u_{\text{rms}}/u_{\text{mean}}$ as a function of the forcing frequency for the optimized operating conditions. 40
2.12 Ratio of indirect to direct noise level upstream of the nozzle η_u in the TAFG setup based on analytical values for $\mathcal{R}_a$ and $\mathcal{R}_s$ and on an estimation of $|\sigma/P_u^+| = 10$. 41

3.1 Schematic for the measurement of the upstream waves at the inlet of the nozzle 43
3.2 Schematic view of the Two- and Three-Microphone Method . . 45
3.3 Reflection coefficients at the outlet of the cylindrical tube. M_u =0.002 47
3.4 Real (left) and imaginary (right) part of the transfer functions of thermocouple 2 to 1. ◯: D12-1. △: D12-2. □: D06-1 53
3.5 Estimation of thermocouple time constants by LS method (left column) and DE method (right column) for the cases D12-1 (top), D12-2 (middle), D06-1 (bottom). Red symbols: τ_1. Blue symbols: τ_2. The mean value is traced in black line with annotations on the right border of the figures. All input signals have been smoothed with Savitzky-Golay filter. 55
3.6 Reconstructed gas temperature using different methods in the operating condition D12-2 at 10 Hz modulation 57
3.7 Root-mean-square value of the temperature fluctuations as a function of modulation frequency. Black symbols: original signals. Red symbols: reconstructed signals. ◯: D12-1. △: D12-2. □: D06-1 58
3.8 Modulus and phase angle of the complex ratio $H_{sa} = \sigma/P_u^+$. . . 59

4.1 Schematic view of waves and measurements in the upstream domain of the nozzle. The grey area corresponds to the numerical calculation domain for the code SUNDAY 62
4.2 Sensitivity of analytical reflection coefficient $\mathcal{R}_a$ as a function of relative variation of Mach number M_u for nozzles D12 and D06. 63
4.3 Reflection coefficients obtained from SUNDAY simulations with the diff-R method. Results are compared to analytical values in black bars. 66

4.4 Direct (left) and indirect (right) nozzle reflection coefficients obtained from SUNDAY simulations with the diff-R method. Results are compared to analytical values of $\mathcal{R}_a$ and $\mathcal{R}_s$ in black bars. Error bars are obtained from 1000 runs with random noise signals. 67
4.5 Experimental and numerical signals from SUNDAY for the experimental case NO.1. 68
4.6 Phase difference $\Delta\phi_{12}$ between entropy waves at x_1 and x_2 (left axis) and convective velocity modulation level u'/u at x_2 (right axis) as a function of time. dashed-line: linear simulation; black-line: nonlinear simulation. 69
4.7 Direct (left) and indirect (right) reflection coefficients measured by the diff-R method in the case with finite-amplitude convective velocity fluctuations. 70
4.8 Signal-to-noise ratio of pressure and temperature measurements 71
4.9 Analytical direct reflection coefficient $\mathcal{R}_a$ and the reflection coefficients $\mathcal{R}(\sigma = 0)$ at nozzle inlet calculated using ideal and noisy signals. The case number corresponds to those in Table 3.3.Error bars are obtained from 1000 runs with random noise signals. . . 72
4.10 Indirect reflection coefficient $\mathcal{R}_s$ calculated analytically and by the diff-R method using ideal and noisy signal. The case number corresponds to those in Table 3.3. Error bars are obtained from 1000 runs with random noise signals. 72
4.11 Modulus (left) and phase angle (right) of the nozzle reflection coefficient $\mathcal{R}$ for configurations D12-1 (top), D12-2 (middle) and D06-1 (bottom). Analytical $\mathcal{R}_a$ (black-line), $\mathcal{R}(\sigma \neq 0)$ (◯) and $\mathcal{R}(\sigma = 0)$ (×). 74
4.12 Indirect reflection coefficient $\mathcal{R}_s$. D12-1: analytical (dashed-line), experimental (◯). D12-2: analytical (black-line), experimental (△). D06-1: analytical (dash-dotted-line), experimental (□). 75
4.13 Ratio of indirect to direct noise level upstream of the nozzle η_u for the three optimised operation conditions 75

5.1 Turbulent energy spectrum plot as a function of wave numbers. DNS, RANS and LES are summarised in terms of spectral frequency range. k_C is the cut-off wave number used in LES (log-log diagram) (Poinsot and Veynante 2005) 80
5.2 Schematic view of the CESAM-HP burner 83
5.3 The perforated plate used in ICS. The grey area corresponds to the discharge plane of the jet. Unit in mm. 83
5.4 Computational domain for the reactive LES 85
5.5 View of the unstructured mesh of the computational domain . . 85

5.6 Acoustic properties of the perforated plate with a back cavity from LES (symbols) and analytical modified Howe's model (line). Case op16-0-2-85 90

6.1 Overview of reactive LES simulations. Pressure (top), axial velocity (middle) and temperature (bottom) signals are recorded by a probe at $(x, y, z) = (140, 0, 0)$ mm from reactive LES simulations. 94
6.2 Time-averaged LES temperature field superposed with axial velocity for three operation conditions. 95
6.3 Axial velocity field from time-averaged non reactive simulation of the case op16-0-2-85 in the plane $Z = 0$. Black lines indicates negative axial velocity $u < 0$. 96
6.4 Mean and RMS velocity profiles for the non reactive case op16-0-2-85. LES (line) and PIV (symbols). 97
6.5 Mean and RMS velocity profiles for the reactive case op13-5-0-85. LES (line) and PIV (symbols). 99
6.6 Mean and RMS velocity profiles for the reactive case op16-2-0-85. LES (line) and PIV (symbols). 99
6.7 Schematic view of the calculation of swirl number in the injector 100
6.8 Swirl number along the center axis of the injector. The tangential injection extends from $x = -117.5$ mm to $x = -72.5$ mm. . . . 100
6.9 Evolution of pressure and volume-integrated heat release rate from the LES of case op16-2-0-85 101
6.10 Sound pressure level measured at $x_4 = 122.5$ mm for the three operation conditions. LES (black) and Experiments (red). . . . 103
6.11 Experimental signal coherence factor of two wall pressure sensors in the combustion chamber located at position x_2 and x_4 104
6.12 A snapshot of axial velocity from the 2D LES test of the jet in the case op13-5-0-85 showing the flapping movement of the jet. 104
6.13 Sound pressure level from the LES simulations. 106
6.14 LES snapshots of temperature field for case op16-2-0-85. The green zone corresponds to the flow with non positve axial velocity $u \leq 0$. Snaptshot numbers are shown in the pressure signal from probe located at $(x, y, z) = (0, 0, 0)$, and also in volume integrated heat release rate. The time interval between 2 snapshots is 1 ms. 107
6.15 Axial velocity, pressure and temperature amplitude spectrum from DMD analysis of instantaneous field in longitudinal plane $z = 0$. Amplitude calculated using the L^2-norm of the modes in median plane devided by square-root of the nodal points. Case op16-2-0-85 110
6.16 Fluctuating temperature field in longitudinal plane $z = 0$ from the DMD mode at 129 Hz for case op16-2-0-85 111

6.17 Interpolation grid. Eight 70×70 mm^2 transversal planes starting from $x = 87.5$ to $x = 136.5$ mm with an equal distance of 7 mm and discretized by square grids of 2×2 mm^2. 113
6.18 Mean (left) and root-mean-square (right) temperature field of the transverse planes on $x = 87.5$ mm (top), $x = 122.5$ mm (middle) and $x = 136.5$ mm (bottom). From interpolated LES simulations of the op16-2-0-85 case. 114
6.19 Normalised surface-averaged pressure and temperature fluctuations at $x = 122.5$ mm from LES simulations 116
6.20 Amplitude spectrum of total and acoustic temperature fluctuations at $x = 122.5$ mm. 116
6.21 Amplitude spectrum of surface-averaged temperature fluctuations at $x = 122.5$ mm. LES (black line) and LIV (red line). . . 116

7.1 Schematic view of the 1D configuration for combustion noise analysis. 1st plane at $x = 87.5$ mm, 8th plane at $x = 136.5$ mm 118
7.2 Cross-correlation of surface-averaged pressure fluctuations with surface-averaged temperature fluctuations, temperature fluctuations measured at $(y, z) = (0, 0)$ and its corrected version by the C_{00} factor. For the case op16-2-0-85 and on the tranversal plane at $x = 136.5$ mm. C_{00} factor is integrated over all nodal points in the plane. 119
7.3 Amplitude spectrum of normalised acoustic and entropy waves upstream of the nozzle at $x = 136.5$ mm determined (a) directly from LES simulations using characteristic wave decomposition and (b) with the diff-R method. 121
7.4 Sound pressure level of direct and indirect noise contribution in the acoustic feedback of the nozzle calculated (a) directly from LES simualtions using characteristic wave decomposition and analytical compact nozzle transfer functions and (b) with the diff-R method. 121
7.5 Nozzle reflection coefficient and the complex ratio of incident entropy to acoustic waves. Lower frequency limit is 10 Hz. Line: Characteristic wave decomposition. Symbols: diff-R method. . . 123
7.6 Amplitude spectrum of entropy wave from diff-R method using cross section averaged temperature fluctuations, temperature fluctuations measured at $(y, z) = (0, 0)$ and its corrected version by the C_{00} factor. For the case op16-2-0-85 and on the tranversal plane at $x = 136.5$ mm. C_{00} factor is integrated over all nodal points in the plane. 124
7.7 Indirect nozzle reflection coefficients calculated (a) directly from LES simulations using characteristic wave decomposition and (b) with the diff-R method. Lower frequency limit is 100 Hz. 125

A.1 Schematic view of the cross flow jets injecting to the main stream 132

B.1 Enlarged view of the 0.4 mm mesh for the 2D test of the jet . . 137
B.2 Axial velocity profile along y-direction 138
B.3 Axial velocity along jet center line 138

C.1 Model of th burner as a. two and b.five cavities. Unit in mm . 140
C.2 Schematic drawing of the Pressurized Impedance Measurement System (PIMS) adapted from Lamraoui et al. (2011). 142
C.3 Sound pressure level measured by pressure sensors in PIMS and combustion chamber adapted from Mazur et al. (2015) 142
C.4 Reflection coefficient in the feeding line meausured at a radial distance of 60 mm from the injector axis. 142

Nomenclature

The following file gives the nomenclature :
Roman symbols:

c	Sound speed
c_p	Specific heat
f	Frequency
f_s	Sampling frequency
H_{xy}	Transfer function of signal y to signal x
k	Wave number
k	Constant factor in the expression of thermocouple time constant
m	Exponential of wire diameter in the expression of thermocouple time constant
$\dot{m}$	Mass flow rate
M	Mach number
p	Pressure
P^+	Normalised acoustic wave propagating in the flow direction
P^-	Normalised acoustic wave propagating opposite to the flow direction
$\mathcal{R}$	Reflection coefficient
s	Entropy
s	TMM microphone interspacing
S_{xx}	Spectral density of signal x
S_{xy}	Cross spectral density between signal x and y
$\mathcal{T}$	Transmission coefficient
T	Temperature
T_g	TTM true gas temperature
T_w	TTM thermocouple temperature
u	Flow velocity
V	Flow speed
Z_0	Characteristic impedance
Z_r	Radiative impedance

Greek symbols:

α	Ratio of thermocouple time constants
γ	Specific heat ratio
δ	End correction
ρ	Volumetric mass density
σ	Normalised entropy wave
τ	Thermocouple time constant
ω	Angular frequency

Superscripts:

$\hat{}$	Fourier transform
$\bar{}$	Temporal mean
$'$	Fluctuating component
or	TMM original configuration
sw	TMM switched configuration

Subscripts:

av	Spatial average
rms	Root-mean-square
a	Quantity related to acoustic
s	Quantity related to entropy
d	Quantity downstream of the nozzle
u	Quantity upstream of the nozzle
i	Wave number k_i of the acoustic wave propagating in the flow direction
r	Wave number k_r of the acoustic wave propagating opposite to the flow direction

Abbreviations :

LES	Large sddy simulation
LIV	Laser interferometric Vibrometer
PIV	Particle Image Velocimetry
RMS	Root mean square
SNR	Signal to noise ratio
TAFG	Temperature and Acoustic Fluctuations Generator
TMM	Three-microphone method
TTM	Two-thermocouple method

Introduction

Communities near airports suffer increasing exposure to noise pollution as the increase of air transportation. This brings more restrictions and regulations on noise emission of aircraft during the take-off, approach and landing phases. Reducing aircraft noise has thus become the focus of many industrial and research activities. This thesis treats the noise generated by the combustion process in the aeroegines and proposes methods for measuring the direct and indirect combustion noise.

Aircraft noise sources

Figure. 1 shows different noise sources for long and short range aircraft during the approach phase. Airframe noise results from the interaction of turbulent flow with solid bodies such as flaps, slats, landing gear and airfoil. It is more important than noise radiated from the propulsion system, since the engine is throttled down at the approach phase. However, engine noise becomes the main contribution of aircraft noise during take-off and landing (Groeneweg et al. 1991).

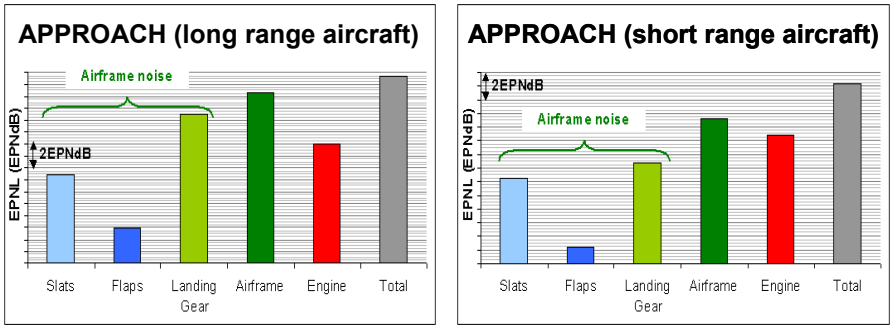

Source: Airbus

Figure 1: *Aircraft noise sources breakdown (Dobrzynski 2010)*

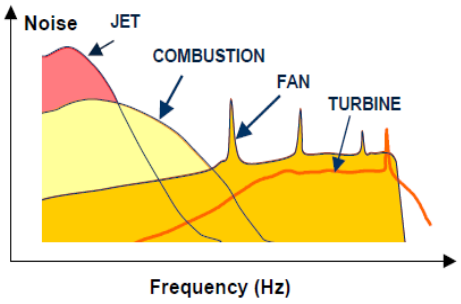

Figure 2: *Typical turbofan noise contribution and noise spectrum (Sensiau 2013)*

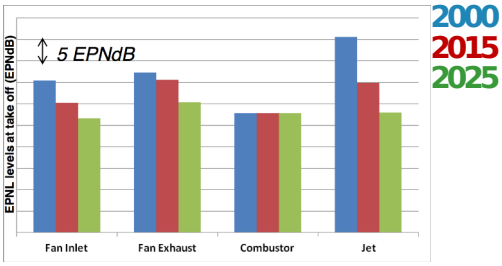

Figure 3: *Typical breakdown of turbofan noise sources between 2000 and 2025 (Sensiau 2013)*

Microphone-array techniques are often used to characterise the location, level and frequency of noise sources in jet engines (Blacodon 2009; Miles 2010). By these methods, different noise sources in a modern turbofan have been identified and characterised in Fig. 2. Jet noise emits from the turbulent mixing of the engine exhaust with the ambient air. From the 1970s great achievement has been done in the reduction of jet noise (see Fig. 3). This is made possible by high bypass ratio engines. Further achievement can be made by new concepts such as ultra-high bypass ratio turbofans. However, this introduces another important noise contribution: the fan noise. Fan noise features a broadband spectrum superposed with some tonal pitches related to the turbomachinary system (see Fig. 2). It is also considered as the most important broadband noise contribution of turbofan engines (Enghardt 2015). Research on the reduction of fan noise has been motivated for decades and as high as 5 EPNdB has been achieved from 2000 (see Fig. 3). While fan noise and jet noise have been largely reduced, combustion noise becomes the noise floor that has to be lowered in order to reduce the total engine noise.

Combustion noise

General introduction on combustion noise

Combustion noise has been found as an excess noise source when engine is running at low RPM (Revolutions Per Minute) regime (Bushell 1971). At high exhaust speeds, it is usually masked by jet noise. Combustion noise is a broadband noise in low frequency range typically between 100 and 2 000 Hz and it is weakly attenuated by acoustic liners. Recent microphone-array measurement of a commercial CFM56-5B engine showed that most of combustion noise sound power radiates towards downstream of the engine at 120 to 130° to the flow direction (Sensiau 2013). In terms of energy loss due to conversion

into acoustic power, combustion noise sound power typically takes up 10^{-6} to 10^{-5} of the thermal input of a well-functioning engine, such a small fraction does not deteriorate much engine efficiency (Strahle 1978).

The relative contribution of combustion noise to the total engine noise emission has remained low until recently, when new combustion concepts such as lean-premixed (LPM) combustion, or lean-premixed prevaporized (LPP) combustion for liquid fuels and rich-burn quick-quench lean-burn (RQL) combustion have been introduced. These new combustion chambers have been designed for the purpose of reducing NOx emissions, but they intrinsically induce flame extinction near lean condition (Lefebvre 1977; Huang and Yang 2009) and thereby generates large heat release rate fluctuations by flame surface destruction (Ducruix et al. 2003). The unsteady heat input from turbulent combustion gives rise to acoustic, temperature and velocity fluctuations in the vicinity of the combustion zone. This generates acoustic, entropy and vorticity waves travelling at different speeds and directions in the combustion chamber (Cumpsty 1979). Coupling mechanisms between these waves have been identified (Howe 1998) and their interactions have two major consequences.

The first one refers to combustion instability, when the acoustic feedback from components downstream of the combustion chamber interferes with the inflow conditions upstream of the combustion region in a constructive way that synchronised pressure oscillations are produced in the combustion chamber (Truffin and Poinsot 2005). Combustion instabilities usually happen at the resonant frequencies of the device and can heavily damage the combustion facility in extreme cases. The produced sound pressure level in this case can be as high as 200 dB and it is usually not considered together with combustion noise issues.

The second consequence is augmented combustion noise emission by the enhancement of system resonances (Candel et al. 2009), from which one makes the distinction between direct combustion noise and indirect combustion noise (Strahle 1978; Candel et al. 2009; Dowling and Mahmoudi 2015).

- **Direct combustion noise** results from the unsteady heat release rate of turbulent combustion.

- **Indirect combustion noise** is the acoustic disturbances generated when the vorticity and entropy inhomogeneities produced by turbulent combustion are accelerated in components downstream of the combustion chamber such as nozzles or turbine blades.

The different mechanisms generating direct and indirect combustion noise have been well described in the literature, for example in Strahle (1978); Crighton et al. (1992); Candel et al. (2009), the following only gives a summary of previous works on the theory of combustion noise.

Theory of combustion noise

Direct combustion noise has been extensively studied in the literature for unbounded turbulent flames. Many early experimental investigations (Smith and Kilham 1963; Thomas and Williams 1966; Price et al. 1969; Shivashankara et al. 1974) have observed that the noise radiation from free turbulent combustion in the far field is highly correlated with the rate of change of the overall heat release in the flame zone . The mechanisms behind this phenomenon was later described by Strahle (1978) with an analytical relation linking the far field pressure perturbations with the unsteady heat release rate in the flame zone. This relation has been corrected by a modern approach of combustion noise Crighton et al. (1992) and revisited by Candel et al. (2009) in Eq. (1).

$$p'(r,t) = \frac{\gamma - 1}{4\pi r c_0^2 r} \int_{V_c} \frac{\partial \dot{Q}}{\partial t} \left(\mathbf{r_0}, t - \frac{r}{c_0} \right) dV(\mathbf{r_0}) \tag{1}$$

In this expression, γ is the specific heat ratio, c_0 is the ambient uniform sound speed, $\dot{Q}$ is the volumetric heat release rate in the combustion zone of volume V_c and $\frac{r}{c_0}$ is the time delay between the noise source and the far field observation point.

The classical theory of combustion noise, represented by Eq. (1), has been derived closely following Lighthill's analogy for aerodynamic sound (Lighthill 1952). Instead of solving the full flow dynamics, the turbulent flame is considered as a distribution of monopole sound sources generated by the unsteady change of reaction rate in the flame zone. The interactions between the turbulent flow and the sound field generated by this flow, such as convection, refraction or diffraction are already included in the source term (Bogey et al. 2003; Bailly et al. 2010). This theory is valid for low Mach flow, which is the case in most applications in order to maintain combustion. It applies to far field sound produced from a compact flame zone, meaning that the length scale of the flame zone L is negligible compared to the acoustic wavelength $\lambda \gg L$ and the distance from the observation point to the compact flame zone $r \gg \lambda$.

It is now worth examining the near field sound production from turbulent flames, since this is relevant to the sound pressure inside a combustion chamber. This issue has been handled by Candel et al. (2009) through an inhomogeneous wave equation Eq. (2) derived from the conservation equations of mass, species,

momentum and energy governing a low Mach number $M \ll 1$ reacting flow.

$$\begin{aligned}\nabla^2 p - \frac{1}{c_0^2}\frac{\partial^2 p}{\partial t^2} = &- \rho_0 \frac{\partial}{\partial t}\left(\frac{\dot{Q}}{\rho c_p T}\right) \\ &- \rho_0 \nabla u : \nabla u - \rho_0 \nabla \cdot \left[\left(\frac{1}{\rho} - \frac{1}{\rho_0}\right)\nabla p\right] \\ &- \rho_0 \frac{\partial}{\partial t}\left[W \frac{\partial}{\partial t}\left(\frac{1}{W}\right)\right] + \rho_0 \frac{\partial}{\partial t}\left[\left(\frac{1}{\rho c^2} - \frac{1}{\rho_0 c_0^2}\right)\frac{\partial p}{\partial t}\right] \end{aligned} \quad (2)$$

This equation approximates the wave equation obtained by Crighton et al. (1992) in the low Mach number limit by neglecting sound produced from viscous dissipation, heat diffusion and molecular diffusion in the reacting flow. Similar equation has also been deduced in Bailly et al. (2010) by extending both Phillips' (Phillips 1960) and Lilley's (Lilley et al. 1972) equation to reactive flows in the low Mach number limit.

It is noted that to this point both Eq. (1) and (2) are established for unconfined combustion, or when the interactions between flame produced pressure field and the source terms are weak (Candel et al. 2009). For most low Mach number systems undergoing stable combustion, it is generally assumed that the system is isobaric and that pressure fluctuation level is small compared to the mean pressure (Poinsot and Veynante 2005). Pressure waves reflected back from boundaries towards the combustion region are also scattered by the flame (Lieuwen and Cho 2005). The separation of noise sources in Eq. (2) are generally justified.

Eq. (2) separates explicitly five source terms in the right hand side. The direct combustion noise source appears in the first term. It is related to the heat release rate fluctuations and constitutes the principle contribution to the far field sound pressure, as shown in Eq. (1). The fourth term shows the sound production by non-isomolar combusion. This term becomes relevant for example in oxygen enhanced combustion (Truffaut et al. 1998), but is negligible in air-breathing combustion due to the specie dilution by nitrogen (Lieuwen 2012). The fifth term should be also very small in low Mach number flows since $\rho c^2 = \gamma p$ is quasi-constant through the combustion region (Candel et al. 2009). The remaining two terms are responsible for indirect combustion noise generation (Crighton et al. 1992; Howe 1998). The sound pressure associated with the two terms are usually weak in free combustion compared to that generated by the unsteady heat release (Candel et al. 2009). However, it becomes competitive with direct contributions in confined combustion and when the flow is accelerated within solid boundaries such as nozzles or turbine blades (Howe 2010). The term $\rho_0 \nabla u : \nabla u$, corresponding to Lighthill's aerodynamic sound source (Lighthill 1952) associated with the Reynolds stress, is responsible for sound generation when vorticity inhomogeneities are accelerated (Dowling and

Mahmoudi 2015). The last term in Eq. (2) is responsible for sound generation when flow regions with a local density significantly different from the surrounding such as entropy spots generated by uneven combustion, interacts with a pressure gradient (Dowling and Mahmoudi 2015).

In most applications turbulent combustion takes place in confined combustor equipped with flow-accelerating elements. The acoustic radiation from the combustor therefore has both direct and indirect contributions. While it is generally admitted that direct combustion noise prevails in the far field (Strahle 1978; Candel et al. 2009), this is less justified for the near field. For that it is necessary to examine in detail indirect noise generation when vorticity and entropy fluctuations are accelerated.

Sound generation by accelerated flow inhomogeneities

Many works have been contributed to analyse the interaction between flow inhomogeneities produced from turbulent combustion in a flow-accelerating element such as nozzle and turbine blades. Tsien (1952) first characterized analytically nozzle responses to one dimensional axial pressure and velocity perturbations by a transfer function defined as the ratio of mass flow perturbations to pressure perturbations at the entrance of the nozzle, or equally by the ratio $\left(\frac{\rho'}{\rho}+\frac{u'}{u}\right)/\frac{p'}{p}$, as a function of the oscillation frequency. Crocco and Cheng (1951) later introduced the concept of the specific admittance ratio $\alpha=\frac{u'}{u}/\frac{\rho'}{\rho}$ for studying the role of nozzle in combustion instabilities. They obtained an analytical solution for a subsonic nozzle in the entire frequency range under the hypothesis of isentropic small-amplitude perturbations and determined experimentally the admittance of a choked nozzle from pressure and velocity measurements made at the nozzle inlet. Bell et al. (1973) examined experimentally the admittance of a nozzle mounted on a classical impedance tube facility. The standing-wave pattern that was superimposed on a mean flow velocity in the impedance tube was measured by a 10-microphone array to calculate the nozzle admittance using a linear regression method on the measured pressure amplitudes.

These early investigations implied a global characterisation of the acoustic impedance of the nozzle. In order to differentiate elementary mechanisms accounting for the global acoustic behavior of the nozzle, flow inhomogeneities resulting from turbulent combustion have been synthesized into acoustic, entropy and vorticity modes (Chu and Kovásznay 1958) and examined separately when these modes interact with a nozzle (see for example Marble and Candel (1977); Moase et al. (2007)) or with turbine blades (see for example Cumpsty (1979); Mishra and Bodony (2013)). While acoustic fluctuations propagate

at the speed of sound relative to the flow motion, entropy and vorticity fluctuations are transported by the flow. According to the theory of combustion noise, a conversion of entropy and vorticity fluctuations into acoustic disturbances takes place when there is a change in the mean flow velocity. In linear regime, the sound converted from accelerated entropy and vorticity fluctuations superpose straightforwardly to the acoustic field.

Concerning vorticity generated sound, a comprehensive theory of the vortex sound was given in Howe (2003). Recently Howe (2010) also gave an analytical solution for sound generation when vorticity fluctuations are produced by flow separation in a diffuser. Hulshoff et al. (2001) examined numerically the sound production of a vortex as it passes through a nozzle and found that the vortex circulation, initial position, and mean flow Mach number are the primary factors influencing the amplitude and phase of the sound produced. In experimental domain, vorticity fluctuations were generated artificially in Kings et al. (2011) by altering circumferential air-injections through pulsed valves. The intensity of the measured vortex sound was found to increase with the intensity of the steady swirling flow. This subject is not treated further in the thesis, which will focus on entropy generated noise. For clarity, the term *indirect combustion noise* denotes only *entropy generated noise* in the rest of the work.

When entropy perturbations are considered, Marble and Candel (1977) simplified the problem by considering the nozzle as compact, i.e. its length is small compared to the acoustic and entropy disturbance wavelengths. They considered incoming one-dimensional linear perturbations of pressure and temperature, and compute analytically the reflection and transmission coefficients of a compact nozzle with jump conditions. Results show that, at the nozzle location, the incident acoustic wave is transmitted and reflected and an additional acoustic disturbance is generated due to the acceleration of entropy waves. In the compact approximation limit, the nozzle transfer function depends only on the nozzle inlet and outlet Mach numbers.

For larger nozzles, featuring a length that cannot be neglected with respect to acoustic and entropy wavelengths, Marble and Candel (1977) extended their work for finite-length supercritical nozzles by assuming 1D linear velocity distribution (Tsien 1952) in the nozzle. Moase et al. (2007) gave the analytical forced response of a choked nozzle and supersonic diffuser with a normal shock by considering the flow in the nozzle as multiple connected segments with linear steady velocity. An 1D linear piecewise analytical model modified from Moase's work was later developed by Giauque et al. (2012) and applied to the shape optimization of the nozzle in terms of generating low indirect combustion noise contributions in Giauque et al. (2013). Stow et al. (2002) showed that at moderate compactness ratio a simple choked nozzle can be represented by a constant cross section duct with an effective length that is terminated

by the choked boundary condition. This effective length is independent of the type of flow perturbation (acoustic or entropy) and can be calculated using a general mean velocity profile in the nozzle. Goh and Morgans (2011) later proposed to calculate the effective lengths separately for acoustic and entropy disturbances in supersonic nozzles. Durán and Moreau (2013) recently gave an analytical solution for finite-length nozzles using flow invariants and Magnus expansion, which can be generalised to any velocity profile and to both subsonic or supersonic conditions in the nozzle.

These developments were carried out in the linear regime with small-amplitude pressure, velocity and temperature disturbances. For waves with finite amplitudes propagating through a supersonic diffuser, Moase et al. (2007) found that the interaction of the disturbances with the shock resulted in strong non-linear effects such as unchoke, unstart and *over-choke*. They predicted the critical amplitude of the disturbances causing the three non-linear effects and showed that the nozzle/diffuser responded strongly linearly when the disturbances were below the critical amplitude. Huet and Giauque (2013) recently suggested the use of a nozzle describing function in which acoustic waves are written in their Riemann invariant form. In this description, the extended nozzle describing function for entropy noise is a function of the entropy wave amplitude. Predictions with this formalism have been validated numerically in both subsonic and supersonic nozzles with finite amplitude waves.

Role of entropy wave on thermoacoustic instabilities

It is now worth examining combustion thermoacoustic instabilities by including entropy wave propagation and entropy noise contribution.

Classical works on combustion instability analysis, for example Yang and Anderson (2008); Poinsot and Veynante (2005), usefully consider zero-Mach number flow and therefore exclude the convection of entropy wave. However, Dowling (1995) found that the unstable modes in a generic model combustor with an open end differed significantly as the flow Mach number increased. In the presence of a mean flow, the frequency of the first mode at a moderate temperature ratio across the heat release input zone can be as two times smaller than in the no flow case. Similar results have also been observed in the analysis of unstable mode of a model rocket combustor with and without entropy wave (Yu et al. 2010; Sisco et al. 2011). Dowling (1995) also found that the unstable mode frequency is very sensitive to the heat release spatial distribution and little change occurred for a compact heat release zone much smaller than the acoustic and entropy wavelengths. In aeronautical engines, the combustion chamber is optimized to be as short as possible and combustion takes place

over a large volume of the chamber. The effect of entropy wave propagation on combustor thermoacoustic instabilities can not be ignored.

Consider now the conversion of accelerated entropy disturbances into sound in the downstream region of a combustor. There are two possible consequences, depending essentially on the outlet impedance of the combustor. When the reflection coefficient is small enough, entropy generated noise is essentially transmitted out of the chamber. This can be considered as an open-loop mechanism where entropy perturbations are converted into sound, which is then radiated in the surrounding environment. This issue has already been discussed in terms of indirect combustion noise. When the reflection coefficient of the combustor outlet increases, a coupling mechanism between the acoustic field and entropy fluctuations may also take place leading to amplified entropy disturbances at specific discrete frequencies. This feedback results in a resonant loop, called rumble (Eckstein et al. 2004), where synchronized pressure and temperature oscillations increase in the chamber until a limit cycle is reached.

The role of entropy waves on the development of rumble instabilities has been investigated in many studies, but without providing definitive conclusions. Zhu et al. (2001) observed a self-sustained low frequency (50-120 Hz) instability in a liquid-fuel combustor equipped with spray atomizers and chocked on its downstream side. Analysis of the instability mechanism took into consideration the entropy mode and its convection time in the combustor was found to be close to the rumble period. Eckstein et al. (2006) compared the rumble instability frequency of a RQL combustor with an outlet open to the atmosphere and with a choked Venturi nozzle. Self-excited instabilities occurred in both cases and had comparable pressure amplitudes and frequencies, proving that the entropy mode was not the primary cause of the onset and sustainment of the rumble instability observed in this combustor. The different observations made by Zhu et al. (2001) and Eckstein et al. (2006) may be due to the dispersion of hotspots between the flame region where they are produced and the combustion chamber outlet due to turbulent mixing in the RQL combustor. Dispersion and dissipation of entropy waves were later considered in the analysis of Goh and Morgans (2013). These authors found that the convected entropy mode can destabilize or stabilize a combustor depending on the flow configurations. Motheau et al. (2014) analysed the convection and reflection of entropy fluctuations to examine their impact on combustion instabilities within combustors featuring complex geometries. They defined a delayed entropy-coupled boundary condition (DECBC), which sums up acoustic and entropy contributions to the reflected acoustic wave inside the chamber to represent the acoustic feedback from the nozzle on the pressure sound field inside the combustor. The two contributions are linked with the incident velocity fluctuations upstream of the flame by time-delayed models for acoustic and entropy waves and the respective reflection coefficients. This method naturally extends one dimensional analytical

models to the simulation of these interactions within 3D geometries (Dowling and Stow 2003). The DECBC then provides the acoustic-entropy interaction condition for simulations with an Helmholtz solver (zero-Mach approach) and yielded unstable modes which were in good agreement with LES (Large Eddy Simulation) results of the same model combustor. In their approach, the nozzle response to acoustic and entropy incident waves were shown to be essential in predicting successfully the correct combustion instability frequency.

For conclusion, there are evidences that entropy waves may have an influence on the combustion chamber stability even if many other parameters influence its dynamics. A description of the acoustic-entropy coupled feedback appears necessary to predict combustion instabilities in combustion chambers equipped with nozzles.

Motivations and objectives of the thesis

The mechanisms from which indirect combustion noise is generated are well known both analytically and numerically. The corresponding experiments remain however a great challenge. To study indirect combustion noise alone, it is necessary to generate temperature fluctuations without any other acoustic source. Attempts have been made in early investigations by Zukoski and Auerbach (1976) with clever setups generating entropy fluctuations by periodical heat addition to the air flow. The more recent Entropy Wave Generator (EWG) (Bake et al. 2009) uses an electrical heating module to produce a hot air column that is transported downstream through a convergent-divergent nozzle. Results for the entropy induced pressure wave propagating in the downstream direction through the nozzle and for the amplitude of temperature fluctuations agreed with theoretical predictions, although numerical simulations of the EWG setup in supersonic cases (Leyko et al. 2009) and subsonic cases (Durán et al. 2013; Giauque et al. 2012) showed that reflections from the EWG outlet and direct noise generated by the electrical heating system both contribute to pressure fluctuations in the discharge flow.

It appears to be very difficult to generate pure indirect noise without introducing any additional acoustic disturbance. It is then worth examining experimental methods aiming at characterizing entropy noise when other noise contributions are present at the same time in the flow. This type of problem has only been addressed in a limited number of investigations, that generally rely on a separation of incoherent contributions to the noise field. Muthukrishnan, Strahle, and Neale (1978) carried out experiments on real engines to separate the entropy induced noise spectrum from total combustion noise inside the combustor. This was realized by correlating the pressure signals recorded

outside and inside the combustion chamber. Comparisons of the two noise spectra recorded showed a transition of dominance from direct noise to entropy noise when the combustor outlet is choked. This method is however not valid in low frequency range where the noise level is the largest because in this frequency range acoustic and temperature fluctuations have a strong coherence. This coherence has been reported as an important error factor in measuring the transfer function of a choked nozzle in a stable combustion chamber (Hield and Brear 2008). Therefore the present work aims at developing an experimental strategy to measure the acoustic and entropic impedances of a nozzle that is submitted to low frequency highly coherent pressure and temperature fluctuations as is often the case in combustion chambers.

Meanwhile, there are evidences showing the coupling between acoustic and entropy waves during self-sustained thermoacoustic oscillations. The analytical and numerical models used for that purpose need as inputs a correct description of the acoustic and entropic impedances of the combustion chamber outlet. This constitutes the second motivation for the development of a methodology allowing the separation of synchronized acoustic and entropy harmonic disturbances. The validation of this method represents one of the objectives of the thesis.

Thesis organisation

The thesis is divided into two parts.

Part I is dedicated to the experimental and numerical validation of diff-R method to measure direct and indirect nozzle transfer functions. It incorporates four chapters:

- **Chapter 1** first summarises the existing analytical work on compact nozzle transfer functions. The transfer function of a subsonic compact nozzle accounting for the nozzle outlet impedance condition are then derived from the previous works. The obtained analytical solutions serve as the reference for the validation of separation methodology.

- **Chapter 2** presents the experimental setup TAFG, which generates simultaneous pressure and temperature fluctuations in a tube flow that is accelerated by a convergent nozzle at the outlet of the tube. The performance of the TAFG setup in terms of the amplitude of the generated temperature fluctuations is given from a parametric study of the setup by changing the mass flow rates and the modulation frequency.

- **Chapter 3** focuses on the experimental methods for measuring nozzle

reflection coefficients and the acoustic and entropy waves upstream of the nozzle. Three-microphone method is used to measure the nozzle reflection coefficients and Two-thermocouple method is used to compensate temperature fluctuations measured by a single thermocouple with finite response time.

- **Chapter 4** proposes the method to measure the direct and indirect transfer functions of the nozzle, called diff-R. The method is first applied to a numerical case calculated by a dedicated solver and then to experimental measurements. The method is validated numerically by comparing with the analytical nozzle transfer functions and some discussions on the limit of the method are given in the end to explain the differences between experimental and analytical nozzle transfer functions.

Part II is dedicated for the analysis of combustion noise in a laboratory scale combustor using Large Eddy Simulation and the diff-R method. It is composed of three chapters:

- **Chapter 5** introduces first the Large Eddy Simulation method and the CESAM-HP burner, a lean-premixed swirl-stabilised combustor with a choked nozzle at the combustion chamber outlet. It then gives the numerical configurations, models and boundary conditions used in the LES of the combustor by the high-fidelity LES code AVBP.

- **Chapter 6** presents the LES results by comparing with experimental results from three aspects, including aerodynamic, thermoacoustic and temperature fluctuations approaching the nozzle. Especially the self-sustained combustion instability is analysed using LES and dynamic mode decomposition technique.

- **Chapter 7** evaluates the downstream propagating acoustic and entropy waves from pressure and temperature time series at different positions along the combustor center axis that are converted from 2D LES fields. The diff-R method is then applied to separate direct and indirect noise contributions in the upstream propagation acoustic wave and to determinate the indirect nozzle transfer function.

Conferences and publications associated with this thesis

Tao, W., Schuller, T., Ducruix, S., and Richecoeur, F. (2013). Development of a noise generator dedicated to direct and indirect combustion noise separation. Proceedings of the European Combustion Meeting 2013.

Tao, W., Mazur, M., Huet, M., and Richecoeur, F. (2015). Indirect combustion noise contributions in a gas turbine model combustor with a choked nozzle. Presented at the 9th Mediterranean Combustion Meeting. Accepted for publication in a special issue in Combustion Science and Technology.

Tao, W., Huet, M., Schuller, T., and Richecoeur, F. (2015). Separation of entropy generated noise in acoustically perturbed nozzles. Submitted to the Journal of Sound and Vibration.

Mazur, M., Tao, W., Scouflaire, P., Richecoeur, F., and Ducruix, S. (2015). Experimental and Analytical Study of the Acoustic Properties of a Gas Turbine Model Combustor With a Choked Nozzle. In Volume 4B: Combustion, Fuels and Emissions (p. V04BT04A001). ASME. http://doi.org/10.1115/GT2015-43013

Kings, N., Tao, W., Scouflaire, P., Richecoeur, F., and Ducruix, S.(2015). Experimental and numerical investigation of direct and indirect combustion noise contributions in a lean premixed laboratory swirled combustor. Submitted to ASME 2016 Turbo Expo.

Kings, N., Tao, W., Mazur, M., Scouflaire, P., Richecoeur, F., and Ducruix, S. (2015). Experimental and numerical determination of temperature fluctuations within a swirled premixed laboratory combustor. Submitted to the 36th International Symposium on Combustion.

Part I

Separation of entropy generated noise in an acoustically perturbed nozzle

Chapter 1

Nozzle transfer functions

The main objective of this part of the thesis is the validation of an experimental method allowing to separate direct and indirect noise contributions to the pressure field in the near field of a nozzle when it is submitted to simultaneous acoustic and entropy disturbances. For that the concept of nozzle transfer function is used in this work and a compact nozzle has been employed in our experiments, because it's analytical transfer functions are well documented in the literature. This chapter first summarises previous works on nozzle transfer functions. In the next step, the analytical transfer function of a subsonic nozzle taking account of nozzle downstream boundary conditions are deduced from the previous works. The deduced subsonic nozzle transfer functions will serve as a reference during experimental explorations.

1.1 Analytical solutions of nozzle transfer functions

Linear models are well-known efficient tool to investigate unsteady combustion and flows (Yang and Anderson 2008; Culick 2006; Poinsot and Veynante 2005). In theses models, the flow quantities are usually decomposed into temporal-mean and time-varying values such as in Eq. (1.1).

$$\Phi(\mathbf{x}, t) = \Phi(\mathbf{x}) + \Phi'(\mathbf{x}, t) \tag{1.1}$$

By supposing small amplitude of the fluctuations compared to the mean quantity, flow perturbations are synthesized into pressure, entropy and vorticity modes which propagate independently and are only coupled in the acceleration region within the nozzle (Chu and Kovásznay 1958). While pressure and entropy are scalar quantities, vorticity is a three dimensional vector. Vorticity disturbances are not discussed in the thesis.

For an one-dimensional adiabatic, non-viscous and non-reacting unsteady flow presenting small-amplitude perturbations, the flow motions are governed by linearised Euler equations (LEE) Marble and Candel (1977); Moase et al. (2007); Giauque et al. (2012); Durán and Moreau (2013):

$$\left\{\frac{\partial}{\partial t}+u\frac{\partial}{\partial x}\right\}\left(\frac{p'}{\gamma p}\right)+u\frac{\partial}{\partial x}\left(\frac{u'}{u}\right)=0 \tag{1.2}$$

$$\left\{\frac{\partial}{\partial t}+u\frac{\partial}{\partial x}\right\}\left(\frac{u'}{u}\right)+\frac{c^2}{u}\frac{\partial}{\partial x}\left(\frac{p'}{\gamma p}\right)+\left(2\frac{u'}{u}-(\gamma-1)\frac{p'}{\gamma p}-\frac{s'}{c_p}\right)\frac{\partial u}{\partial x}=0 \tag{1.3}$$

$$\left\{\frac{\partial}{\partial t}+u\frac{\partial}{\partial x}\right\}\left(\frac{s'}{c_p}\right)=0 \tag{1.4}$$

Here ρ, u, p, c stand for mean density, velocity, pressure and sound speed, the primed terms stand for perturbations of the corresponding quantities.

Consider now the same flow passing a nozzle. The flow can be divided into three zones: zones upstream and downstream of the nozzle where the mean flow velocity is constant ($\partial u/\partial x = 0$), and the zone in the nozzle where the mean flow velocity varies as the change of nozzle cross section. In both zones upstream and downstream of the nozzle, the solutions of the LEE are well known and acoustic and entropy waves are written in familiar forms by harmonic decomposition under the $e^{i\omega t}$ convention (Eqs. (1.6)-(1.7)).

$$\frac{p'}{\gamma p}=\mathrm{Re}\left[e^{i\omega t}\left(P^+e^{-i\frac{\omega}{c+u}x}+P^-e^{i\frac{\omega}{c-u}x}\right)\right] \tag{1.5}$$

$$\frac{u'}{c}=\mathrm{Re}\left[e^{i\omega t}\left(P^+e^{-i\frac{\omega}{c+u}x}-P^-e^{i\frac{\omega}{c-u}x}\right)\right] \tag{1.6}$$

$$\frac{s'}{c_p}=\mathrm{Re}\left[e^{i\omega t}\left(\sigma e^{-i\frac{\omega}{u}x}\right)\right] \tag{1.7}$$

where $P^+=\frac{1}{2}(p'/\gamma p+u'/c), P^-=\frac{1}{2}(p'/\gamma p-u'/c)$ and σ are the characteristic waves in the flow.

The waves upstream and downstream of the nozzle are matched with the solution inside the varying section zone of the nozzle. This allows to deduce nozzle transfer functions. Different matching conditions have been established in the literature depending on the nozzle geometry.

The analytical solutions of the LEE in finite-length nozzle were well studied in (Marble and Candel 1977; Moase et al. 2007; Giauque et al. 2012). In these works, linear velocity profiles in the nozzle (Tsien 1952) have been used in common for spatial integration of the LEE. For general velocity profiles, an alternative approach by considering the nozzle as piecewise succession of compact segments with constant velocity inside has also been developed and

validated by different Eulerian solvers (Giauque et al. 2012; Durán and Moreau 2013). Whereas the analytical solutions of finite-length nozzles are nozzle-dependant, the analytical solutions for compact nozzles are quite general and have been widely applied in literature. They are categorised below depending on the presence of shock.

1.1.1 Compact nozzle without shock

When the nozzle is compact, meaning that the length of the nozzle is negligible compared to the entropy and acoustic wavelengths, it can be considered as a discontinuity in the flow (Marble and Candel 1977). The geometry of the nozzle is not seen by the forcing waves, whereas it determines the discharge Mach number M_d. This allows to match the perturbation equations of mass flow rate:

$$\frac{\dot{m}'}{\dot{m}} = \frac{1}{M}\frac{u'}{c} + \frac{p'}{\gamma p} - \frac{s'}{c_p} \tag{1.8}$$

the total temperature:

$$\frac{T_t'}{T_t} = \frac{1}{1+\frac{1}{2}(\gamma-1)M^2}\left[(\gamma-1)\frac{p'}{\gamma p} + (\gamma-1)M\frac{u'}{c} + \frac{s'}{c_p}\right] \tag{1.9}$$

and entropy:

$$\frac{s'}{c_p} = \frac{T'}{T} - (\gamma-1)\frac{p'}{\gamma p} \tag{1.10}$$

on both side of the nozzle by the following jump conditions:

$$\left(\frac{\dot{m}'}{\dot{m}}\right)_u = \left(\frac{\dot{m}'}{\dot{m}}\right)_d \tag{1.11}$$

$$\left(\frac{T_t'}{T_t}\right)_u = \left(\frac{T_t'}{T_t}\right)_d \tag{1.12}$$

$$\left(\frac{s'}{c_p}\right)_u = \left(\frac{s'}{c_p}\right)_d \tag{1.13}$$

where the subscripts u, d stand for the upstream and downstream region of the nozzle respectively. Now the LEE are closed, the solutions are examined separately for the flow configurations without shock illustrated in Fig. 1.1, as in Marble and Candel (1977). The last configuration (see Fig. 1.1(c)) corresponds to the special case of subsonic nozzles, when downstream perturbations propagate to the upstream through the nozzle. In the particular case of choked nozzle, the mass flow rate is inversely proportional to the root mean square of total temperature of the flow. Based on this unique characteristic of choked

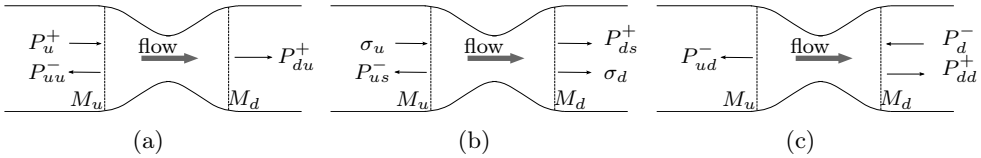

Figure 1.1: *Schematic view of the reflection and transmission of acoustic and entropy waves when they enter the nozzle. Constant cross section zones are delimited by vertical line. The second subscripts u, d, s in wave notations stand for respectively the contributions to the sound field due to the incident acoustic wave from upstream, the incident acoustic wave from downstream and the entropy wave.*

nozzle, Eq. (1.14) is derived from the perturbation equation for mass flow rate (Eq. (1.11)) and total temperature (Eq. (1.12)). It holds both at inlet and outlet of the nozzle (Marble and Candel 1977).

$$\frac{u'}{c} - \frac{\gamma}{2} M \frac{p'}{\gamma p} + \frac{1}{2} M \frac{\rho'}{\rho} = 0 \tag{1.14}$$

From the compact nozzle solutions given in Marble and Candel (1977), the direct (due to acoustic) and indirect (due to entropy) reflection and transmission coefficients of the subsonic nozzle write:

$$R_u = \frac{P_{uu}^-}{P_u^+} = \left(\frac{M_d - M_u}{M_d + M_u}\right)\left(\frac{1 + M_u}{1 - M_u}\right)\left[\frac{1 - \frac{1}{2}(\gamma - 1) M_u M_d}{1 + \frac{1}{2}(\gamma - 1) M_u M_d}\right] \tag{1.15}$$

$$T_u = \frac{P_{du}^+}{P_u^+} = \left(\frac{2M_d}{M_d + M_u}\right)\left(\frac{1 + M_u}{1 + M_d}\right)\left[\frac{1 + \frac{1}{2}(\gamma - 1) M_d^2}{1 + \frac{1}{2}(\gamma - 1) M_u M_d}\right] \tag{1.16}$$

$$R_d = \frac{P_{dd}^+}{P_d^-} = -\left(\frac{M_d - M_u}{M_d + M_u}\right)\left(\frac{1 - M_d}{1 + M_d}\right)\left[\frac{1 - \frac{1}{2}(\gamma - 1) M_u M_d}{1 + \frac{1}{2}(\gamma - 1) M_u M_d}\right] \tag{1.17}$$

$$T_d = \frac{P_{du}^-}{P_d^-} = \left(\frac{2M_d}{M_d + M_u}\right)\left(\frac{1 - M_d}{1 - M_u}\right)\left[\frac{1 + \frac{1}{2}(\gamma - 1) M_u^2}{1 + \frac{1}{2}(\gamma - 1) M_u M_d}\right] \tag{1.18}$$

$$R_s = \frac{P_{us}^-}{\sigma} = -\left(\frac{M_d - M_u}{1 - M_u}\right)\left[\frac{\frac{1}{2} M_u}{1 + \frac{1}{2}(\gamma - 1) M_u M_d}\right] \tag{1.19}$$

$$T_s = \frac{P_{ds}^+}{\sigma} = \left(\frac{M_d - M_u}{1 + M_d}\right)\left[\frac{\frac{1}{2} M_d}{1 + \frac{1}{2}(\gamma - 1) M_u M_d}\right] \tag{1.20}$$

For supercritical nozzles, the direct and indirect nozzle reflection coefficients are determined only by the approaching flow, so they are dependent only on

the inlet Mach number M_u, as shown below:

$$R_u^{choke} = \frac{1 - \frac{1}{2}(\gamma - 1)M_u}{1 + \frac{1}{2}(\gamma - 1)M_u} \tag{1.21}$$

$$R_s^{choke} = -\frac{\frac{1}{2}M_u}{1 + \frac{1}{2}(\gamma - 1)M_u} \tag{1.22}$$

1.1.2 Compact nozzle with shock

When a shock is present in the diffuser part of the nozzle, the problem is complicated by the nature of the shock, and also the interaction of the shock with acoustic and entropy waves. But since the nozzle is choked in this case, the reflected waves are not affected by the shock, meaning that the solutions for R_u (Eq. (1.21)) and R_s (Eq. (1.22)) are still validated.

For small-amplitude flow perturbations, the Mach number upstream of the shock is not affected and is determined solely by the nozzle geometry. In this case, the well-known jump condition of a normal shock are use to match the waves on both side of the shock, which depends only on the Mach number relative to the shock (Marble and Candel 1977). Consider now only P_u^+ wave forcing the nozzle (see Fig. 1.2). Right upstream of the shock, the incident wave P_i^+ is related to P_u^+ by Eq. (1.21). The matching conditions for the waves in the supersonic and subsonic region upstream and downstream of the shock were given in Eq. (1.23) and (1.24) (Moase et al. 2007; Leyko et al. 2009; Leyko et al. 2011). Eq. (1.24) supports the fact that entropy fluctuations are generated when acoustic perturbations interacts with the shock.

$$\begin{aligned}(1 + M_s^2 + 2M_s M_d^2)P_i^+ + (1 + M_s^2 - 2M_s M_d^2)P_i^- = \\ (1 + M_s^2 + 2M_s^2 M_d)P_d^+ + (1 + M_s^2 - 2M_s^2 M_d)P_d^-\end{aligned} \tag{1.23}$$

$$\sigma_d = (P_d^+ + P_d^- - P_i^+ - P_i^-)(\gamma - 1)\frac{(M_s^2 - 1)^2}{(\gamma - 1)M_s^4 + 2M_s^2} \tag{1.24}$$

where M_s is the approaching Mach number relative to the shock.

1.2 Transfer transfer functions of a subsonic nozzle accounting for nozzle outlet impedances

The schematic view of the tube terminated by a nozzle used in the experiments is illustrated in Fig. 1.3. The nozzle is located at x_n and is submitted to incoming acoustic wave P_u^+ and entropy wave σ. In response, a reflected P_u^- and

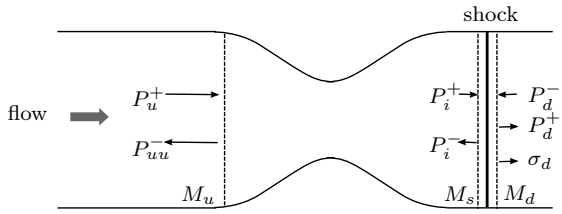

Figure 1.2: *Schematic view of forced response of nozzle with shock*

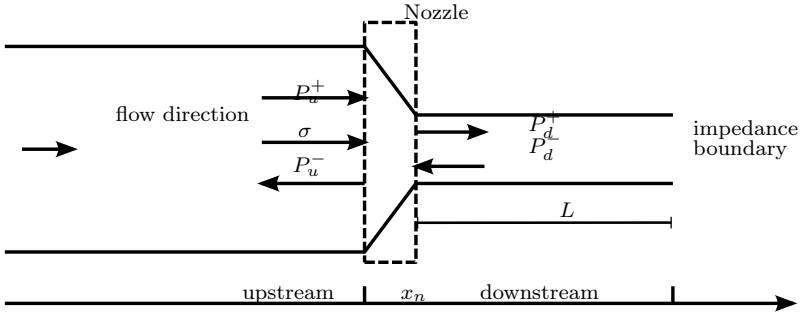

Figure 1.3: *Waves in ducted system with a nozzle*

a transmitted P_d^+ pressure wave are generated upstream and downstream the nozzle respectively. In the experiments inspected in this work, there also exists a pressure wave P_d^- downstream of the nozzle due to reflection at the boundary condition downstream the nozzle. For a subsonic nozzle, this disturbance propagates towards the nozzle and can also generate a contribution to the sound field upstream the nozzle. According to the noise generation mechanisms described by Marble and Candel (1977), waves likes P_u^- and P_d^+ have thus direct and indirect contributions from incident acoustic pressure waves and entropy waves. These pressure variables can be decomposed as:

$$P_u^- = P_{uu}^- + P_{ud}^- + P_{us}^- \tag{1.25}$$
$$P_d^+ = P_{du}^+ + P_{dd}^+ + P_{ds}^+ \tag{1.26}$$

The second subscripts u, d, s in the wave notations stand for the contributions to the sound field due to the incident acoustic wave from upstream, the incident acoustic wave from downstream and the entropy wave, respectively.

In the studied system, the nozzle is open to the atmosphere . This has to be taken into account. For simplicity one can represent the downstream section of the nozzle by an open pipe. The impedance boundary condition on the pipe outlet can be characterised by the reflection coefficient R_L with L the length

of the duct. R_L is by definition:

$$R_L = \frac{P_d^-}{P_d^+} \exp(-i(k_i + k_r)L) \tag{1.27}$$

where $k_i = \omega/c(1+M_d), k_r = \omega/c(1-M_d)$ denote the wave number of the incident acoustic and reflected acoustic wave. Combining Eq. (1.26), (1.27), (1.19) and (1.32), the following linear system can be written:

$$\begin{bmatrix} 1 & 0 & -T_d \\ 0 & 1 & -R_d \\ 0 & R_L e^{ik_i L} & -e^{-ik_r L} \end{bmatrix} \begin{bmatrix} P_u^- \\ P_d^+ \\ P_d^- \end{bmatrix} = \begin{bmatrix} R_u & R_s \\ T_u & T_s \\ 0 & 0 \end{bmatrix} \begin{bmatrix} P_u^+ \\ \sigma \end{bmatrix} \tag{1.28}$$

An inversion of the square matrix on the left hand side of Eq. (1.28) yields the expressions of total reflected and transmitted acoustic waves P_u^- and P_d^+:

$$P_u^- = \left[R_u - \frac{R_L T_u T_d e^{ik_i L}}{R_L R_d e^{ik_i L} - e^{-ik_r L}} \right] P_u^+ + \left[R_s - \frac{R_L T_s T_d e^{ik_i L}}{R_L R_d e^{ik_i L} - e^{-ik_r L}} \right] \sigma \tag{1.29}$$

$$P_d^+ = \left[\frac{T_u e^{-ik_r L}}{R_L R_d e^{ik_i L} - e^{-ik_r L}} \right] P_u^+ + \left[\frac{T_s e^{-ik_r L}}{R_L R_d e^{ik_i L} - e^{-ik_r L}} \right] \sigma \tag{1.30}$$

An identification in these equations provides the direct acoustic and entropy induced contributions to the sound field on both sides of the nozzle, from which we can define:

$$\mathcal{R}_a = R_u - \frac{R_L T_u T_d e^{ik_i L}}{R_L R_d e^{ik_i L} - e^{-ik_r L}} \tag{1.31}$$

$$\mathcal{T}_a = \frac{T_u e^{-ik_r L}}{R_L R_d e^{ik_i L} - e^{-ik_r L}} \tag{1.32}$$

$$\mathcal{R}_s = R_s - \frac{R_L T_s T_d e^{ik_i L}}{R_L R_d e^{ik_i L} - e^{-ik_r L}} \tag{1.33}$$

$$\mathcal{T}_s = \frac{T_s e^{-ik_r L}}{R_L R_d e^{ik_i L} - e^{-ik_r L}} \tag{1.34}$$

where the subscript a and s stand for acoustic and entropy contributions. $\mathcal{R}_a$ and $\mathcal{T}_a$ characterize the reflection and transmission of the acoustic wave from upstream of the nozzle. For convenience, $\mathcal{R}_s$ and $\mathcal{T}_s$ are called the indirect reflection and transmission coefficients and they characterise the acoustic waves propagating toward upstream and downstream of the nozzle generated by entropy fluctuations.

1.3 Effect of downstream boundary condition

The expressions in Eqs. (1.31)-(1.34) show that for a subsonic nozzle, the gain and the phase of the nozzle transfer functions are dependent of the boundary

conditions downstream of the nozzle (R_L, L). So two kinds of boundary conditions are investigated here. Descriptions of these terminations are based on the way they can be realised in practical experiments.

- **Anechoic boundary condition:** It refers to a non reflective boundary condition downstream of the nozzle. Such termination can be realised by connecting a wave guide to the nozzle outlet. The transmitted wave P_u^+ is gradually attenuated due to the viscous dissipation and completely vanishes after a distance of 50 m. The reflection coefficients on this type of boundary are therefore equal to 0 for all frequencies. In the absence of the wave P_d^-, the previously defined transfer functions $\mathcal{R}_a, \mathcal{T}_a, \mathcal{R}_s$ and $\mathcal{T}_s$ are actually identical to those given by Marble and Candel (1977), as in Eq. (1.15), (1.16), (1.19) and -(1.20).

- **Open boundary condition:** It refers to a reflective boundary condition downstream of the nozzle, and can be realised by connecting an open pipe with variable length to the nozzle discharge. For a cylindrical duct that is open to the atmosphere traversed by a low Mach number bias flow, it is known that the acoustic radiation in the vicinity of the duct exhaust is planar and can be characterised by the radiative impedance Z_r (Morse and Ingard 1970; Rienstra and Hirschberg 2013). For low frequencies f corresponding to small Helmholtz number ka with $k = 2\pi f/c$ and a the duct radius, Z_r is equal to (Levine and Schwinger 1948):

$$Z_r = \frac{1}{4}(ka)^2\rho c + ik\delta \tag{1.35}$$

  For small duct radius and frequencies ($ka \to 0$), Z_r approximates to its imaginary part $ik\delta$. δ, or the *end correction*, which indicates a fictitious distance from the duct outlet where there is a pressure node. It takes account of the inertia of the air column in the compact region near the duct exhaust. The value of δ varies from $0.61a$ to $8a/3\pi$ for unflanged and flanged circular ducts respectively (Levine and Schwinger 1948; Nomura et al. 1960). Then the reflection coefficient R_L is related to the radiative impedance Z_r by:

$$R_L = \frac{Z_r/Z_0 - 1}{Z_r/Z_0 + 1} \tag{1.36}$$

  where $Z_0 = \rho c$ is the characteristic impedance of the flow.

Using the different boundary conditions, the gain and the phase angle of the direct and indirect nozzle transfer functions are traced in Fig. 1.4 for frequencies between 0 Hz to 1000 Hz. A set of typical parameters encountered during the experimental explorations are used as input: the diameter of the constant

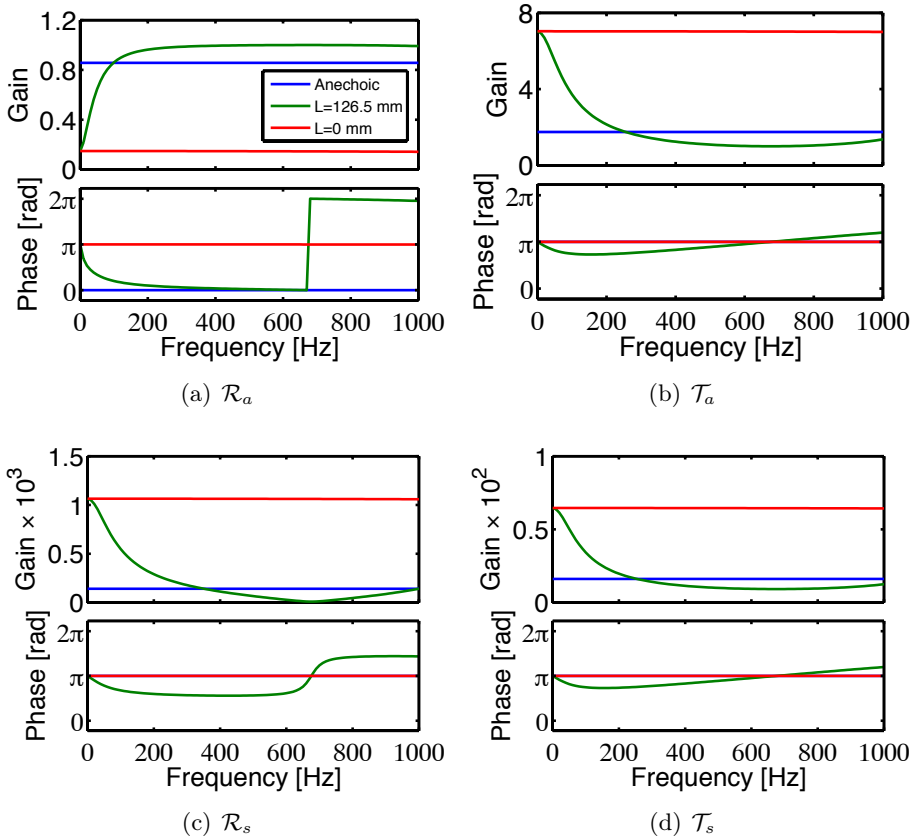

(a) $\mathcal{R}_a$ (b) $\mathcal{T}_a$

(c) $\mathcal{R}_s$ (d) $\mathcal{T}_s$

Figure 1.4: *Evolution of $\mathcal{R}_a, \mathcal{T}_a, \mathcal{R}_s$ and $\mathcal{T}_s$ as a function of frequency for three different downstream boundary conditions. Blue line: anechoic termination; Green line: open pipe termination with $L = 126.5$ mm; Red line: open pipe termination with $L = 0$ mm.*

section upstream and downstream of the nozzle are respectively 20 mm and 6 mm; the inlet and outlet Mach number $M_u = 0.005$ and $M_d = 0.061$. For frequencies up to 1000 Hz, the Helmholtz number associated with the radius of nozzle discharge plane is negligible ($ka < 0.06$) so that the end correction in (Levine and Schwinger 1948) $\delta = 0.61a$ is used to calculate R_L. For open boundary conditions, both $L = 0$ mm and $L = 126.5$ mm are calculated. The former corresponds to the case when the nozzle discharges freely to the atmosphere and the acoustic impedance in the vicinity of the nozzle outlet is approximated by the radiative impedance Z_r.

The direct and indirect transfer functions are invariant to the frequency change in anechoic and $L = 0$ mm cases, however, there is significant change in the gain of all the four transfer functions between the two boundary conditions. For the acoustic wave, there is less reflection and more transmission between an ane-

choic nozzle and a free discharging nozzle, whereas for the entropy wave, there is always more reflection and transmission. In the case when $L = 126.5$ mm, the gain of the four transfer functions shows rapid change at lower frequencies until it saturates at higher frequencies. The approximation at the very low frequencies between the cases when $L = 0$ mm and $L = 126.5$ mm is also observed for all the four transfer functions. This corresponds to the limit when $k_i L \to 0$ and $k_r L \to 0$.

These results show that the reflection from the downstream boundary of a subsonic nozzle largely affects the nozzle transfer functions. These reflections are indirectly induced by the acoustic and entropy wave approaching the nozzle, and they should be taken into account in the experiments that will be presented in the next chapter.

Chapter 2

The Temperature and Acoustic Fluctuations Generator

A test bench has been developed allowing to generate single frequency direct and indirect noise. Entropy fluctuations are generated by hot jets in cross flow where the mainstream is pulsated with a loudspeaker. The acoustic and entropy forcing is therefore highly coherent. Simultaneous pressure and temperature measurements are performed and they are used in this chapter to optimize the test bench in two directions. The first one aims to determine the range of forcing frequencies in which the measurement matches best with the analytic. The second one aims to obtain the amplitude of temperature fluctuations as high as possible by changing injection and modulation parameters.

2.1 Experimental setup

2.1.1 Working principle

The temperature and acoustic fluctuations generator (TAFG) is a system dedicated to simultaneously produce direct and indirect pressure waves with the help of a loudspeaker. As illustrated in Fig. 2.1(a), an enclosed loudspeaker is fixed at the bottom of the TAFG. The loudspeaker enclosure is vented to the upper region for the purpose of maintaining pressure equilibrium on both sides of the suspension membrane. This unit is used to modulate the air flow $\dot{m}_1$ injected at ambient temperature T_1 in the lower part of the setup. The main flow crosses a honeycomb and a converging nozzle before entering a secondary injection zone where air is injected by a series of jets in crossflow. Hot air

is injected through an annular distribution unit made of thirty 1.5-mm holes (Fig. 2.1(b)) and heated up to 200 °C. The acoustic modulation from the loudspeaker creates a pressure fluctuation at the outlet of the hot air injectors. The resulting small jet cross flows are thus modulated at the same frequency as the acoustic wave propagating through the main flow at ambient temperature. The pulsated secondary air flow being at a different temperature, temperature fluctuations are created and are convected by the main flow in the downstream direction. This flow goes through a 90-mm long tube terminated by a convergent nozzle (see Fig.2.1(c)) where entropy fluctuations are accelerated to generate entropy induced noise. Three different nozzles are tested that have the same length equal to 6 mm, but different outlet diameters of 20 mm (the diameter of circular tube meaning there is no acceleration of the flow), 12 mm and 6 mm. The loudspeaker is the direct acoustic source in the system, but it also allows to create synchronized temperature fluctuations. This configuration mimics a combustion chamber in the way that entropy waves and the pressure wave are highly coherent.

The maximum air supply of the primary and secondary injections are respectively 5.38 g/s and 3.59 g/s. For air temperature at 20 °C, this gives the maximum inlet Mach number $M_u = 0.099$ and the maximum outlet Mach number $M_d = 0.277$ for the nozzle D12 by supposing incompressible flow, whereas the nozzle D06 is choked at a mass flow rate of 6.76 g/s by supposing isentropic flow.

2.1.2 Diagnostic techniques

Synchronized sound pressure and temperature measurements are carried out in order the assess acoustic and entropy fluctuations generated in the TAFG system. Three pressure taps and three temperature slots are distributed along the 20-mm diameter tube shown in Fig. 2.1(c). The sensor positions used in this work are shown in Fig. 2.3.

Pressure fluctuations are measured by two B&K 1/4" microphones (see Fig. 2.2(a)) flush-mounted on the tube wall at positions x_1 and x_2. A third microphone of the same type is set at position x_1 in front of the first one as shown in Fig. 2.3. An inter-space of 70 mm is chosen between the positions x_1 and x_2 to determine the acoustic reflection coefficient of the tube with the Three-microphone technique which will be presented in Sec. 3.2.

Temperature is measured by two closely placed fast response K-type bare wire thermocouples (see Fig. 2.2(b)) with a bead diameter of 25 μm and 50 μm at position x_4. The reason for employing two thermocouples is to compensate the effects of the thermocouple response time, the principle of which will be

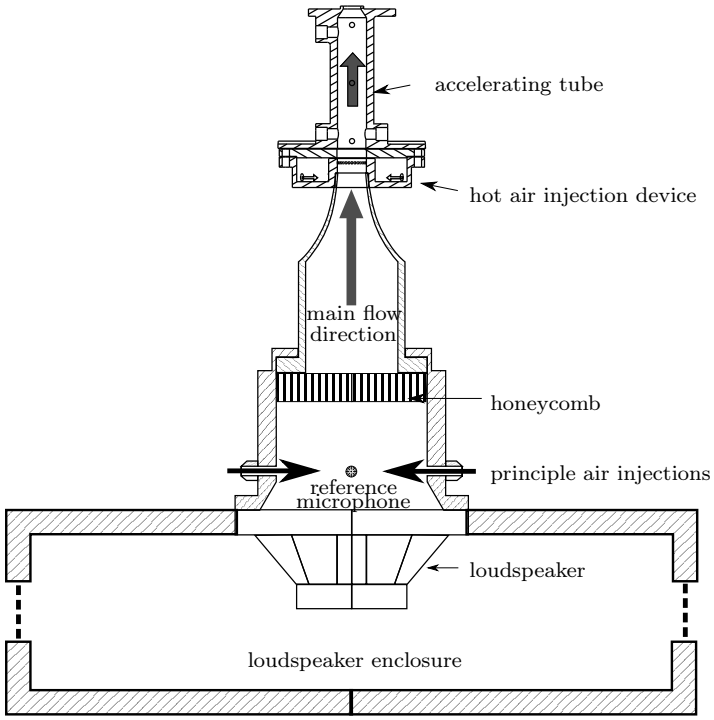

(a) The temperature and acoustic fluctuations generator (TAFG)

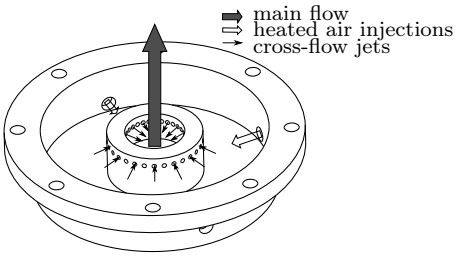

(b) Hot air injection device in a jets-in-crossflow configuration

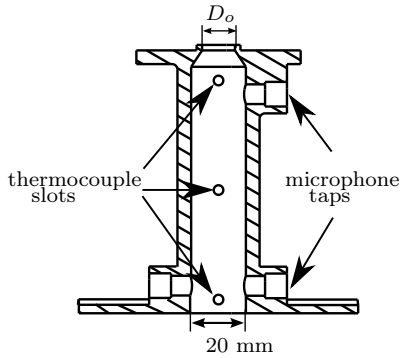

(c) Final tube ending with a converging nozzle to accelerate the flow

Table 2.1: *Nozzle geometries*

Nozzle name	Length [mm]	D_o [mm]
D20	6	20
D12	6	12
D06	6	06

Figure 2.1: *Components of the temperature and acoustic fluctuation generator (TAFG)*

(a) B&K 1/4" microphone

(b) Two-thermocouple sensor. Smaller wire diameter: 25 μm. Larger wire diameter: 50 μm

Figure 2.2: *Pressure and temperature sensors*

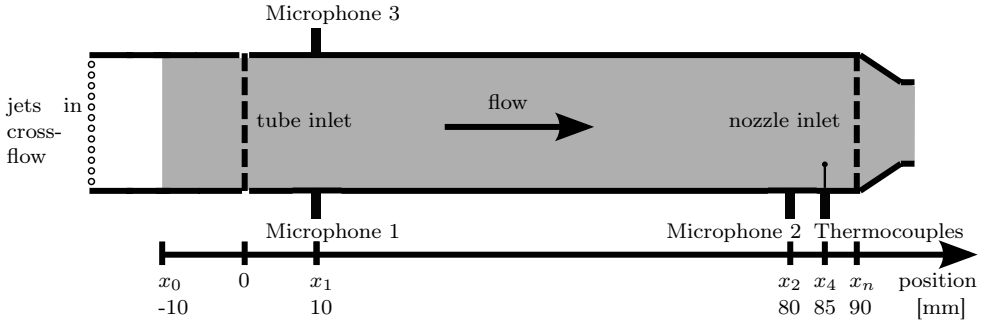

Figure 2.3: *Position of measurements. The grey area corresponds to the numerical calculation domain for the code SUNDAY*

presented in Sec. 3.3. Temperature is supposed to be uniform in each tube section. This assumption has been checked by measuring the temperature at different locations along the tube radius.

The velocity in the tube was also measured by a hot wire anemometer placed within the flow at ambient air temperature in a set of separate experiments. These measurements were used to keep constant the modulation level $u_{\text{rms}}/u_{\text{mean}}$ of the acoustic velocity perturbations independently of the forcing frequency.

Two examples of results are presented in Fig. 2.4 for two nozzles with different outlet diameters, different mass flow rates and forcing conditions. The dynamic pressure, velocity and the raw thermocouple signals are presented in this figure. These signals are recorded at a sampling rate of 8 192 Hz over a duration of 10 seconds. The pressure signals recorded feature clearly a sinusoidal shape at the modulation frequency. Periodic signals at the same fundamental frequency are also observed for the temperature and velocity signals presented even thought they feature a higher harmonic content and additional high-frequency perturbations reduce the signal-to-noise ratio.

Harmonic modulation frequencies up to 1000 Hz has been explored in the TAFG setup, however, only the very low frequencies between 10 to 100 Hz are retained in the thesis. The reasons are two-fold. On one hand the measured nozzle direct reflection coefficient $\mathcal{R}_a$ differs gradually from the compact solution (Eq. (1.31)) as the frequency increases. On the other hand it is difficult to generate high-amplitude temperature fluctuations for higher frequencies. These two effects are discussed separately in the next sections.

2.2 Setting up the frequency range

The frequency range in which the measured nozzle transfer functions are in good agreement with the compact solutions are explored in this section. To do so, the reflection coefficient at the inlet of the nozzle is measured when no crossflow jets are injected. In this case the measured reflection coefficient corresponds to the direct nozzle reflection coefficient $\mathcal{R}_a$ and can be compared to its analytical value in Eq. (1.31).

The measurement configuration is illustrated in Fig. 2.5. The direct reflection coefficient $\mathcal{R}_a$ is measured by Three-microphone method (TMM) which will be presented in Sec. 3.2. In order to characterise the outlet boundary condition downstream of the nozzle, the TMM is also applied to measure the reflection coefficient R_L. The discharge plan of the nozzle is then extended by a cylindrical duct in order to allow measurements downstream of the nozzle. The duct ends at a distance of $L = 126.5$ mm from the nozzle discharge and is open to the

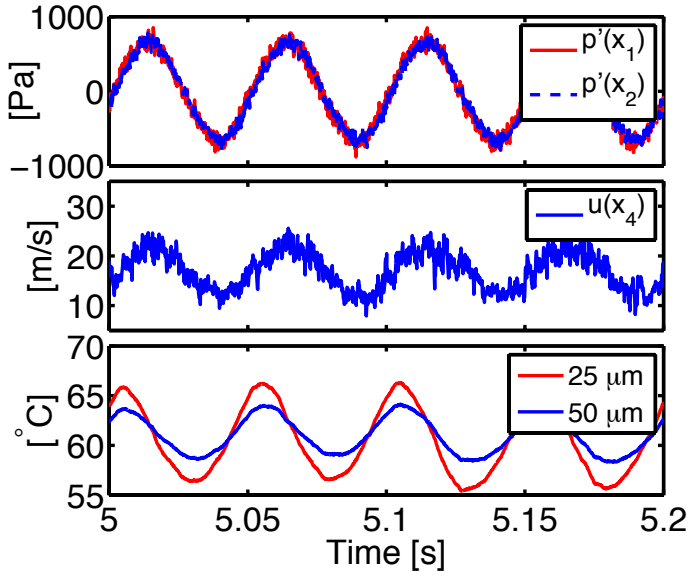

(a) Nozzle D12, $M_u = 0.050, u_{\text{rms}}/u_{\text{mean}} = 0.24$, modulation at f=20 Hz.

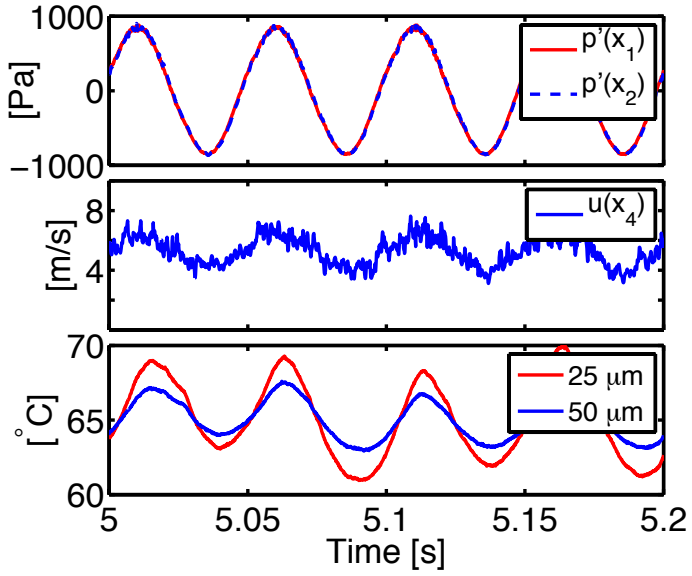

(b) Nozzle D06, $M_u = 0.016, u_{\text{rms}}/u_{\text{mean}} = 0.21$, modulation at f=20 Hz.

Figure 2.4: *Signals of the dynamic pressure, velocity and temperature*

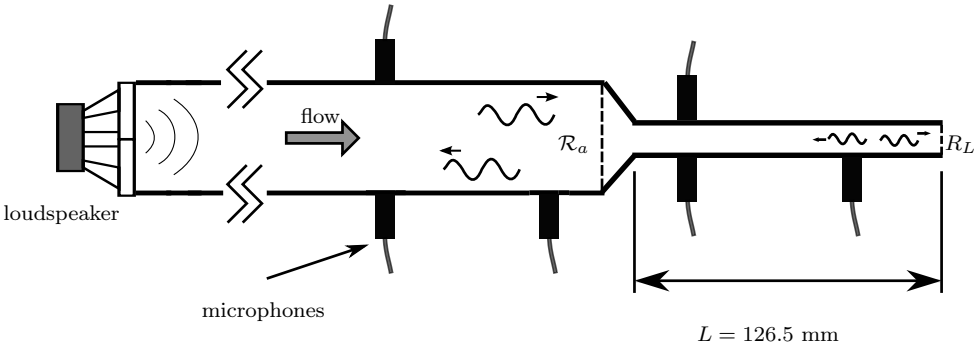

Figure 2.5: *Schematic view of the experimental configuration to measure $\mathcal{R}_a$ and R_L*

atmosphere. Same type of microphones were installed on the wall of the duct, with the same TMM measurement configuration as on the upstream side the nozzle. During the experiments, only the main air injection is used and the dry air temperature is at 20°C. The sound speed in this case is equal to 343.2 m/s. The bulk velocity of the approaching flow to the nozzle is equal to 1.89 m/s, giving the inlet and outlet Mach numbers $M_u = 0.005, M_d = 0.061$. The acoustic modulation amplitude $u_{\text{rms}}/u_{\text{mean}}$ measured at position x_4 is around 0.10 for frequencies up to 1000 Hz.

The gain and the phase angle of the reflection coefficient at a distance of $L = 126.5$ mm from the nozzle discharge plane are plotted in Fig. 2.6a together with the analytical values given by Levine and Schwinger (1948). The gain $|R_L|$ matches well with the analytic up to 200 Hz corresponding to a small Helmholtz number $ka = 0.01$. However, the difference between experimental and analytical results tends to increase with the frequency higher than 200 Hz. Although there is not measurement of the velocity profiles in the cross section of the duct, the increasing discrepancy at higher frequencies is suspected to result from the increasing damping of the acoustic wave by turbulent mixing in the bulk of the flow as the ratio of the thickness of the acoustic boundary layer to the thickness of the turbulent sublayer decreases with the frequency (Peters et al. 1993). The acoustic dissipation is however not treated in the Three-microphone method, and a variation in the gain of the reflection coefficient inside the duct should be expected in this case.

The measured reflection coefficient R_L is now used in Eq. (1.31) to calculate the analytical value of $\mathcal{R}_a$, which is compared to the experimental results in Fig. 2.6(b). In general, the measured direct reflection coefficient agrees well with the analytic, but slight difference in the gain appears for frequencies higher than 100 Hz. As mentioned before the gain of the reflection coefficient is not constant along the duct due to acoustic dissipations. This could explains the differences between the experimentally and analytically determined $\mathcal{R}_a$ as the frequency increases.

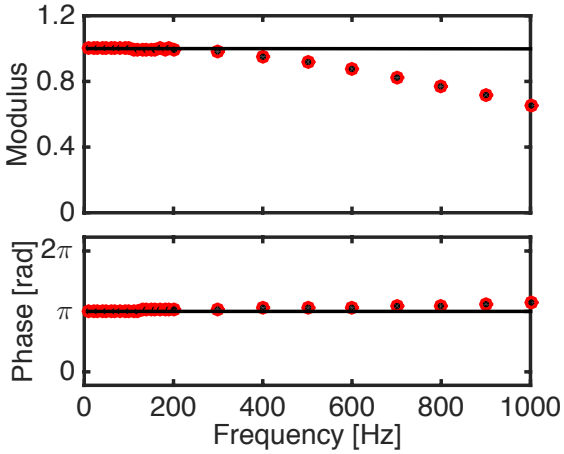

(a) R_L

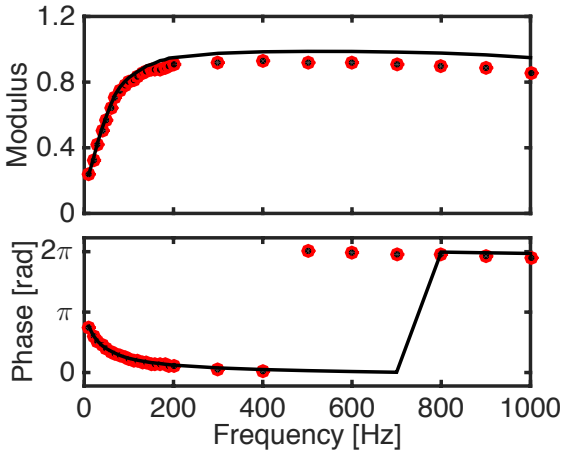

(b) $\mathcal{R}_a$

Figure 2.6: *Experimental (symbols) and analytical (black-line) reflection coefficients R_L and $\mathcal{R}_a$ for frequencies between 10 and 1000 Hz of the nozzle D06 extended by a 126.5 mm duct. The analytical value of $\mathcal{R}_a$ is obtained using the experimentally determined R_L.*

These experiments give one directive information: it is preferable to carry out measurements upstream of the nozzle at low-Mach numbers and at low frequencies in order to obtain good comparison with the analytical nozzle transfer functions. Therefore the frequency range is now set to 10 to 100 Hz. In the next section, a parametric study has been carried out to optimize the TAFG setup to generate simultaneously single-frequency pressure and temperature oscillations from 10 to 100 Hz with the highest amplitude.

2.3 Parametric study of TAFG performance

In order to generate temperature fluctuations as large as possible that can resist to dissipation in the flow, several parameters have been varied to investigate their influences on the resulting temperature fluctuations produced at the inlet of the nozzle. The performance of the system is here characterized by the ratio of the root-mean-square (RMS) to the mean value of the temperature signal measured by the 25 μm thermocouple at position x_4, designated by $T_{\text{rms}}/T_{\text{mean}}$, which indicates to some extent the level of entropy fluctuations that can be generated in the TAFG system (see Eq. (1.7)).

A list of controllable parameters in the TAFG setup are here given:

- The mass flow rate of the mainstream $\dot{m}_1$ and the jets $\dot{m}_2$.
- Loudspeaker modulation frequency
- The temperature of the crossflow jets T_2.
- Gain of the loudspeaker amplifier

In order to generate high temperature fluctuations, the gain of the loudspeaker amplifier was set to large values, giving a sound pressure level between 130 and 145 dB. This high level sound did produce harmonics in all the pressure and temperature signals, but it did not make the acoustic behaviour nonlinear. The gain of the amplifier was adjusted only slightly to keep constant sound pressure level in the system for different modulation frequencies. The temperature of the crossflow jets T_2 was also kept as large as possible in all the experiments. The air injection supplying the jets are heated constantly to 473 K in this study, but the actual temperature of the jets in the hot air injection device is lower than 393 K due to thermal losses. The parametric study in what follows will thus focus on the mass flow rates $\dot{m}_1, \dot{m}_2$ and the modulation frequency f.

2.3.1 Influence of jets and mainstream mass flow rates

Experiments are first conducted for the nozzle D12 by varying the mass flow rates of the mainstream and the jets, while the modulation frequency is set to 10 Hz.

The RMS of the temperature fluctuations is mapped to the 25 sets of mass flow rates $(\dot{m}_1, \dot{m}_2)$ in Fig. 2.7. By linear interpolation (colored contour) of the RMS values, Fig. 2.7 shows that for each mass flow rate of the mainstream there is an optimal mass flow rate for the jets corresponding to maximum T_{rms}.

The jets-in-crossflow has been extensively studied in the literature for its important application in combustion systems. Many works have been contributed to improve the turbulent mixing of the jets with the mainstream by varying the jet-to-mainstream momentum-flux ratio, the geometry, the number and the spacing of the jet orifices in a can or a circular duct (Vranos et al. 1991; Holdeman 1993; Hatch et al. 1995; Kroll et al. 2000). Among these parameters the jet-to-mainstream momentum-flux ratio is considered as the most important parameter influencing the penetration of the jets in the crossflow (Holdeman et al. 1996). For a given configuration of the duct and the jet orifices, Hatch et al. (1995) found that the mixture non-uniformity decreases as the increase of the jet-to-mainstream momentum-flux ratio. One should note that these studies have been conducted in the objective to obtain uniform mixture in the flow downstream of the jets, it is however not intended in the study here, which aims in the contrary to generate non-uniform mixture giving high-amplitude temperature fluctuations.

Since the mass flow rate controls directly the momentum-flux of the mainstream and the jets, the measurement results are now represented as a function of the jet-to-mainstream mass flow rate ratio. The measured mean gas temperature is first plotted against $\dot{m}_2/\dot{m}_1$ in Fig. 2.8. The evolution of T_{mean} can be properly fitted by the relation of equilibrium temperature $T = (\dot{m}_1 T_1 + \dot{m}_2 T_2)/(\dot{m}_1 + \dot{m}_2)$ for the mainstream temperature $T_1 = 286$ K and the jet temperature $T_2 = 384\ K$. Next, the normalised amplitude of temperature fluctuations is plotted against $\dot{m}_2/\dot{m}_1$ in Fig. 2.9, which shows a maximum at $\dot{m}_2/\dot{m}_1 = 0.32$. The general tendency of the relative amplitude was well predicted by a quasi-steady analysis of the TAFG test bench presented in Appendix A, which gives the

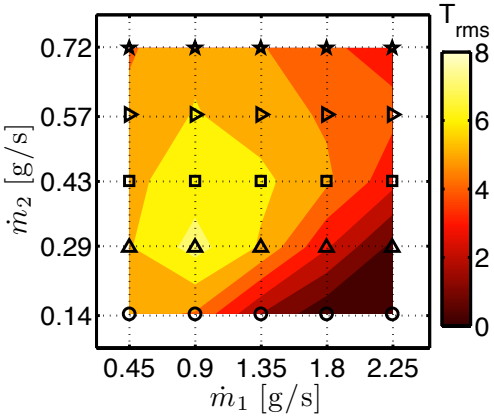

Figure 2.7: *Root-mean-square of temperature fluctuations as a function of the mass flow rate of the mainstream $\dot{m}_1$ and the jets $\dot{m}_2$. $f = 10$ Hz. Nozzle D12.*

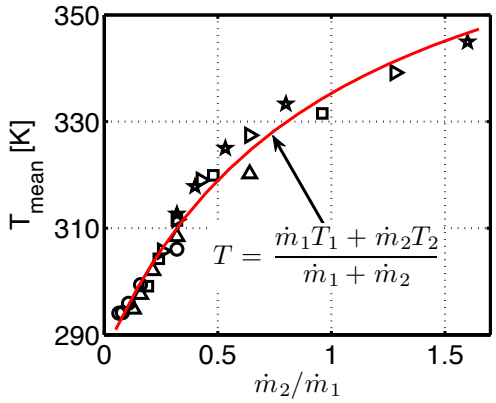

Figure 2.8: *Evolution of the mean temperature as a function of the jet-to-maintream mass flow rate ratio. $f = 10$ Hz. Nozzle D12.*

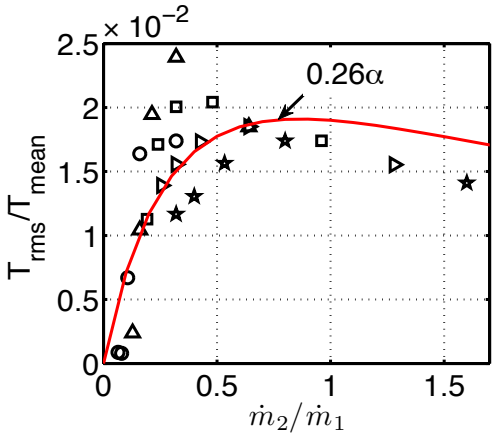

Figure 2.9: *Influence of the jet-to-maintream mass flow rate ratio $\dot{m}_2/\dot{m}_1$ on the normalised amplitude of temperature fluctuations. $f = 10$ Hz. Nozzle D12.*

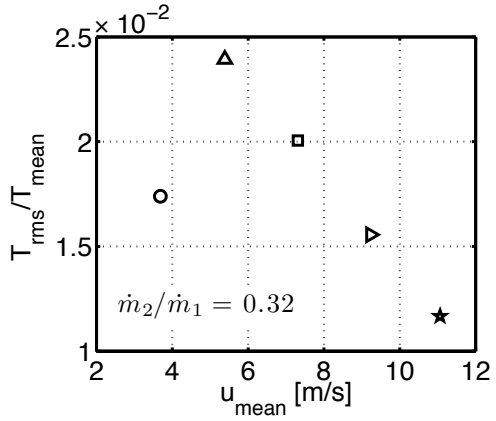

Figure 2.10: *Influence of the mean flow velocity on the normalised amplitude of temperature fluctuations at constant jet-to-maintream mass flow rate ratio. $f = 10$ Hz. Nozzle D12.*

following formulation for the observed dependency at zero-frequency limit:

$$\begin{aligned} &\frac{T_3'(t)}{T_3} = -\frac{1}{2}\alpha\frac{p'(t)}{\Delta p} \\ \text{with} \quad &\alpha = \frac{\dot{m}_2 T_2}{\dot{m}_1 T_1 + \dot{m}_2 T_2} - \frac{\dot{m}_2}{\dot{m}_1 + \dot{m}_2} \\ &T_3 = \frac{\dot{m}_1 T_1 + \dot{m}_2 T_2}{\dot{m}_1 + \dot{m}_2} \end{aligned} \tag{2.1}$$

Here $p'(t)$ is the pressure fluctuations in the mainstream, Δp is the pressure drop across the jets, T_1, T_2 are the mean gas temperatures of the mainstream and the jets, and T_3 is the temperature of the mixture in equilibrium. The temperature fluctuations are designated by $T_3'(t)$. The curve in Fig. 2.9 corresponds to α multiplied by a constant factor 0.26 obtained from least square optimizations.

However, large scattering of the normalised amplitude $T_{\text{rms}}/T_{\text{mean}}$ occurs for $\dot{m}_2/\dot{m}_1$ inferior to 0.5. This is suspected to be caused by the change of flow velocity. For illustration, the data at a constant jet-to-mainstream mass flow ratio $\dot{m}_2/\dot{m}_1 = 0.32$ are extract from Fig. 2.9, and examined in Fig. 2.10 as a function of the mean flow velocity u_{mean} measured in separated experiments without heating the jets. The normalised amplitude of temperature fluctuations first increases then drops continuously as the flow velocity increases. No measurements are here to support the mechanism underlying this drop, but it is conjectured that the level of turbulence within the main stream increases with the flow velocity. Turbulent fluctuations smooth out any organized stratifications of the temperature field produced by the unsteady hot cross-flow jets.

The series of data explorations shows that the performance of the TAFG setup is to the leading order determined by the jet-to-mainstream mass flow rate ratio at $f = 10$ Hz. This feature is used in the thesis to scale the experiments to higher flow velocities, or alternatively higher inlet Mach numbers M_u, which is necessary in order to keep low levels of the normalised convective velocity fluctuations $u_{\text{rms}}/u_{\text{mean}}$ and to avoid possible nonlinear behaviors in the TAFG setup. The ratio $\dot{m}_2/\dot{m}_1$ has been chosen around $\sqrt{T_1/T_2}$, the value corresponding to the maximum of α (see Appendix A).

This procedure has been carried out for different nozzle geometries and led to the choice of three optimal operating conditions summarised in Table 2.2. The ratio of jets-to-mainstream mass flow rate are close to unity in the three cases. The inlet Mach number when the mainstream and the jets are at the same temperature M_u^{cold} are measured by a hot wire.

Table 2.2: *Optimised operation conditions of the TAFG setup*

Configs.	$\dot{m}_1$ [g/s]	$\dot{m}_2$ [g/s]	$\dot{m}_2/\dot{m}_1$	T_{mean} [K]	M_u^{hot}	M_u^{cold}
D12-1	0.81	0.89	1.1	342	0.018	0.017
D12-2	2.69	2.69	1.0	333	0.053	0.050
D06-1	0.81	0.89	1.1	339	0.017	0.016
$*\ \frac{M_u^{\text{hot}}}{M_u^{\text{cold}}} = \frac{\rho^{\text{cold}}\sqrt{T^{\text{cold}}}}{\rho^{\text{hot}}\sqrt{T^{\text{hot}}}}$						

2.3.2 Influence of the modulation frequency

The three optimized cases in Table 2.2 are illustrated in Fig. 2.11, where the RMS values of the temperature fluctuations measured by the 25 μm thermocouple and the convective velocity modulation level $u_{\text{rms}}/u_{\text{mean}}$ are plotted as a function of the forcing frequency.

The modulation level of the convective velocity is relatively constant at 0.2 over the whole frequency range. For frequencies above 40 Hz the system generates temperature fluctuations less than 4 K. The hot air jets which is modulated in crossflow only respond to low frequency pressure excitations. Modifying the hole diameter of the hot air injection unit or the number of holes did not change drastically the response of the system. This phenomenon narrows the frequency range that can be used to generate large amplitude temperature fluctuations. However for forcing frequencies around 10 Hz, temperature fluctuation levels larger than 5 K rms can easily be obtained. This amplitude is theoretically large enough to produce a noticeable contribution to indirect noise as shown by Bodony (2009). After the compensation of temperature fluctuations by the Two-thermocouple method, the corresponding RMS values can reach as much as three times of the uncompensated ones (See 3.3).

2.4 Analytical ratio of indirect to direct noise level in the TAFG setup

The experimental conditions have been explored, the analytical direct and indirect nozzle reflection coefficients, $\mathcal{R}_a$ and $\mathcal{R}_s$ respectively can be calculated with the inlet and outlet Mach numbers reached in TAFG system according to Eq. (1.31) and (1.33). These reflection coefficients are next used to compare the relative level of direct P_{uu}^- and indirect P_{us}^- noise contributions in the near field upstream of the nozzle, which is indicated by η_u:

$$\eta_u = |\frac{P_{us}^-}{P_{uu}^-}| = |\frac{\mathcal{R}_s\sigma}{\mathcal{R}_a P_u^+}| = |\frac{\mathcal{R}_s}{\mathcal{R}_a}||\frac{\sigma}{P_u^+}| \tag{2.2}$$

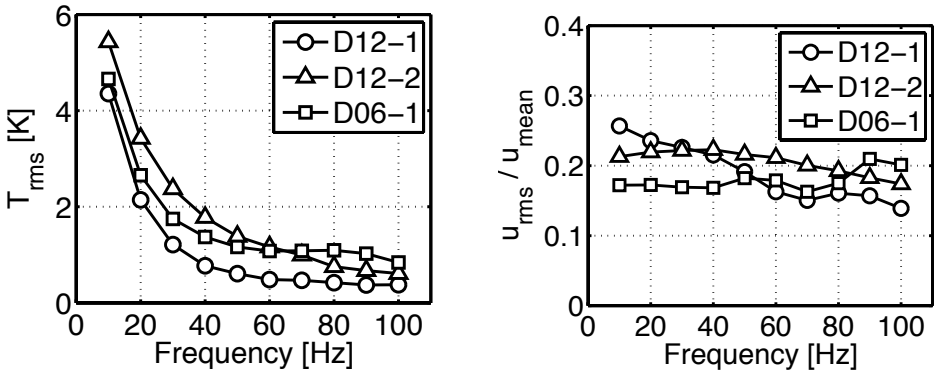

(a) RMS temperature fluctuations measured by the 25 μm thermocouple

(b) Convective velocity modulation level

Figure 2.11: *Root-mean-square temperature fluctuations T_{rms} and modulation level u_{rms}/u_{mean} as a function of the forcing frequency for the optimized operating conditions.*

Here $|\sigma/P_u^+|$ refers to the amplitude ratio of entropy wave to acoustic wave generated in the TAFG system.

The evolution of η_u for $|\sigma/P_u^+| = 10$ as a function of nozzle inlet and outlet Mach numbers is examined now in Fig. 2.12. In the subsonic nozzle the relative contribution of indirect noise increases as the flow accelerates, although it reached less than 50% in the figure, it tends to overweight the direct noise contributions as the entropy fluctuations augment.

The ratio η_u presented in Fig. 2.12 results from the analytical direct and indirect reflection coefficients of the nozzle combined with a moderate estimation of the ratio σ/P_u^+. For experimental evaluations of the ratio η_u, it is necessary to determine the acoustic and entropy waves upstream of the nozzle as well as the nozzle direct and indirect reflection coefficients. Experimental methods using simultaneous pressure and temperature measurement for these purposes are thus presented respectively in Chapter 3 and 4 of the thesis.

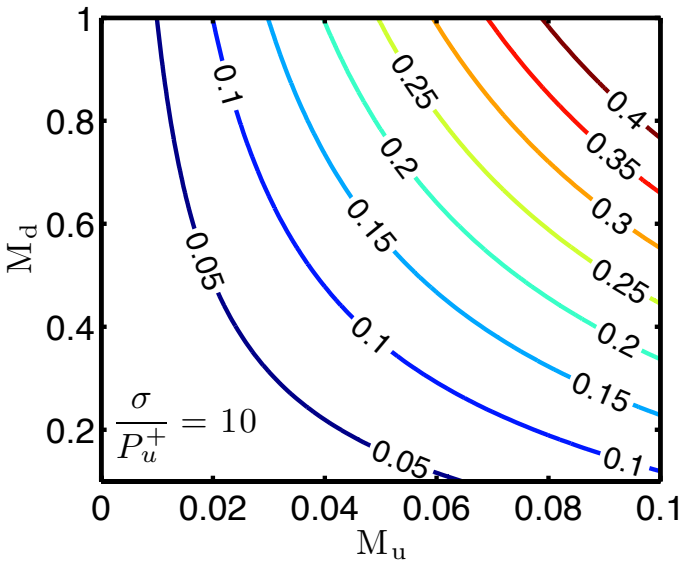

Figure 2.12: *Ratio of indirect to direct noise level upstream of the nozzle η_u in the TAFG setup based on analytical values for $\mathcal{R}_a$ and $\mathcal{R}_s$ and on an estimation of $|\sigma/P_u^+| = 10$.*

Chapter 3

Experimental methods for determining upstream waves

The objective of this chapter is to reconstruct the amplitudes of the incident and reflected acoustic waves and the entropy wave at the inlet of the nozzle, designated by P_u^+, P_u^- and σ respectively in Fig. 3.1, as well as the phase shift between these waves from simultaneous measurements of pressure and the temperature in the tube. The chapter first gives the necessary parameters to be measured in order to determine the acoustic and entropy waves. The employed experimental methods for measuring these parameters are then presented, which include the Three-microphone method for reflection coefficient measurement and the Two-thermocouple method for instantaneous gas temperature measurement. Particularly the proposed algorithm based on the transfer function of the two thermocouples gives a reasonable estimation of the thermocouple time constants. The time constants are also used to compensate the temperature measurement of a single thermocouple and the resulting root-mean-square values of temperature fluctuations reach as high as three times of the uncompensated ones shown in Fig. 2.11(a).

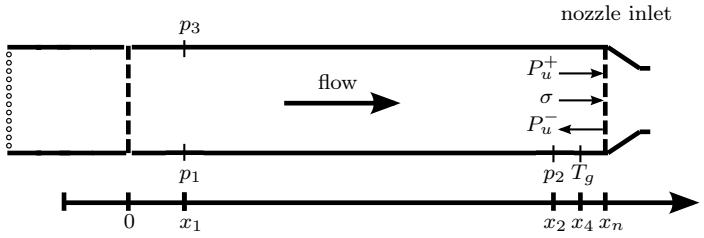

Figure 3.1: *Schematic for the measurement of the upstream waves at the inlet of the nozzle*

3.1 Procedure for reconstructing upstream perturbation variables

Figure 3.1 shows the pressure and temperature measurement positions and the waves $P_u^+.P_u^-, \sigma$ at the inlet of the nozzle to be determined from the measurements.

First by supposing plane wave propagation, the pressure measured at x_2 (see Fig. 2.3) is related to the acoustic waves P_u^+ and P_u^- by:

$$\hat{p}_2 = P_u^+ e^{-ik_i(x_2-x_n)} + P_u^- e^{ik_r(x_2-x_n)} \tag{3.1}$$

where k_i and k_r refer to the wave number of the progressive and regressive acoustic waves in the upstream region of the nozzle. Using the definition of the reflection coefficient at the inlet of the nozzle (x_n) $\mathcal{R} = P_u^-/P_u^+$ in the above expression, one has:

$$P_u^+ = \frac{\hat{p}_2}{e^{-ik_i(x_2-x_n)} + \mathcal{R}e^{ik_r(x_2-x_n)}} \tag{3.2}$$

$$P_u^- = \frac{\mathcal{R}\hat{p}_2}{e^{-ik_i(x_2-x_n)} + \mathcal{R}e^{ik_r(x_2-x_n)}} \tag{3.3}$$

The entropy fluctuations can be deduced from Eq. (1.7) established for small-amplitude fluctuations repeated below:

$$\frac{s'}{c_p} = \frac{T_g'}{\bar{T}_g} - \frac{\gamma-1}{\gamma}\frac{p'}{\bar{p}}$$

In this expression T_g stands for the true gas temperature. Writing pressure waves and entropy waves in conventional propagation form and replacing terms in Eq. 1.7, it is then possible to obtain the complex ratio of incident entropy and acoustic waves, defined as $H_{sa} = \sigma/P_u^+$, as a function of the complex ratio H_{42} between temperature and pressure fluctuations on position x_4 and x_2 respectively (see Fig. 2.3):

$$H_{42} = \frac{\hat{T}_g}{\hat{p}_2} = \frac{H_{sa}e^{-ik_s(x_4-x_n)} + (\gamma-1)(e^{-ik_i(x_4-x_n)} + \mathcal{R}e^{ik_r(x_4-x_n)})}{e^{-ik_i(x_2-x_n)} + \mathcal{R}e^{ik_r(x_2-x_n)}} \tag{3.4}$$

with k_s being the wave number of the entropy wave.

Eqs. (3.2), (3.3) and (3.4) have shown that the upstream variables P_u^+, P_u^-, σ can be determined from the nozzle reflection coefficient $\mathcal{R}$ and the complex ratio of temperature to pressure fluctuations H_{42}. The experimental methods for measuring the two parameters are presented in the next sections.

3.2 Measurement of the reflection coefficient by Two- and Three-Microphone Method (TMM)

A schematic view of the multiple-microphone method in the cylindrical tube of the TAFG setup is shown in Fig. 3.2. The reflection coefficient $\mathcal{R} = P_u^-/P_u^+$ at the nozzle inlet x_n in Fig. 3.2 is first determined by the Two-Microphone Method described by (Chung and Blaser 1980). A third reference microphone located also on axial position x_1 allows to increase the signal to noise ratio. This enhanced method is thus called the Three-Microphone Method. The original method presented in Chung and Blaser (1980) was established for no mean flow case. This section gives an extended version of Two- and Three-Microphone Methods to low Mach number bias flow.

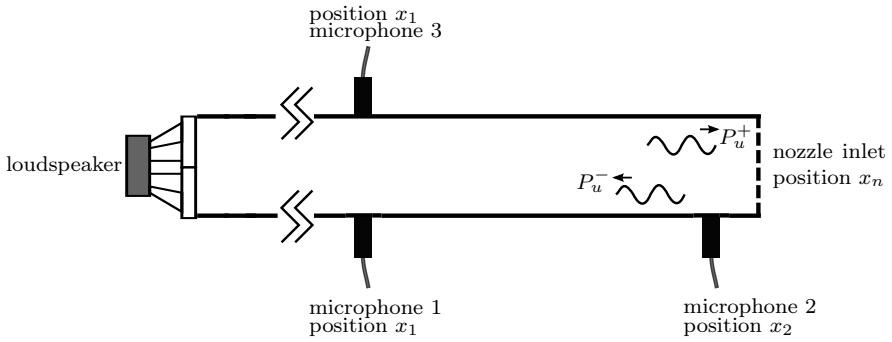

Figure 3.2: *Schematic view of the Two- and Three-Microphone Method*

3.2.1 Two-Microphone Method

The planar pressure wave p_1 and p_2 measured respectively on position x_1 and x_2 are conventionally decomposed into incident and reflected acoustic waves, and their Fourier transform $\hat{p}_1$ and $\hat{p}_2$ write:

$$\begin{aligned}\hat{p}_1 =& P_u^+ e^{-ik_i(x_1-x_n)} + P_u^- e^{ik_r(x_1-x_n)} \\ \hat{p}_2 =& P_u^+ e^{-ik_i(x_2-x_n)} + P_u^- e^{ik_r(x_2-x_n)}\end{aligned} \tag{3.5}$$

where k_i, k_r designate the wave numbers of progressive and regressive acoustic waves. From these expressions the reflection coefficient $\mathcal{R} = P_u^-/P_u^+$ at the nozzle inlet x_n can be deduced by writing the transfer function of pressure signals measured on two positions $H_{21} = \hat{p}_2/\hat{p}_1$, which gives:

$$\mathcal{R} = \frac{H_{21} - e^{-ik_i s}}{e^{ik_r s} - H_{21}} \cdot e^{-i(k_i+k_r)(x_1-x_n)} \tag{3.6}$$

where $s = x_2 - x_1$ is the inter-space of the two pressure sensors. In case of no bias flow, the reflection coefficient becomes undetermined if the sum of the propagation time of progressive and regressive acoustic waves in the distance s is equal to integer multiples of period of acoustic wave, or inverse of the frequency f. For a range of frequencies up to $f_{\max}$, the spacing s should be chosen such that $s \ll c/2f_{\max}$ in order to avoid indeterminacy of the reflection coefficient (Chung and Blaser 1980). This constraint can be extended to the flow at Mach number M_u, so that $s \ll c(1 - M_u^2)/2f_{\max}$. A second constraint, referring to the position of first pressure node from the plane where the reflection coefficient is measured, set the maximum distance of the microphones from x_n. For closed and open ends, this distance is equal to respectively quarter and half of the wave length. In the experiments $s = 70$ mm and $x_n - x_1 = 80$ mm, which satisfy both restrictions for a maximum frequency of 100 Hz.

In practice, the magnitude responses of the condenser-type microphones can be calibrated using a constant pressure-field generator, whereas their phase responses may differ. Therefore the measured pressure signals deviate from the true pressure wave due to different instrumental responses of these pressure sensors. This detriments the reflection coefficient measurements. Such errors, commonly designated as phase-mismatch errors, can be compensated by conducting two set of experiments. In the first set, measurement is carried out with the microphones set at their original location. The same measurement is then repeated by switching one microphone at location x_1 with the microphone set at location x_2. Using I_1 and I_2 to denote the impulsive response of microphones 1 and 2, the measured pressure signals in the two sets of experiments write:

$$\begin{aligned} &\text{original set :} && \hat{p}_1{}^{mes} = I_1\hat{p}_1, \quad \hat{p}_2{}^{mes} = I_2\hat{p}_2 \\ &\text{switched set :} && \hat{p}_1{}^{mes} = I_2\hat{p}_1, \quad \hat{p}_2{}^{mes} = I_1\hat{p}_2 \end{aligned}$$

The corresponding transfer functions of the pressure signals in two positions write:

$$\begin{aligned} &\text{original set :} && H_{21}{}^{or} = \frac{I_2}{I_1}H_{21} \\ &\text{switched set :} && H_{21}{}^{sw} = \frac{I_1}{I_2}H_{21} \end{aligned} \tag{3.7}$$

Taking the average of the transfer functions measured in the two sets of experiments, the instrumental responses vanish and the corrected transfer function reads:

$$H_{21} = \sqrt{H_{21}{}^{or} \cdot H_{21}{}^{sw}} \tag{3.8}$$

Experiments have been carried out to measure the reflection coefficient on the outlet of the cylindrical tube (D20). These measurements are done to validate

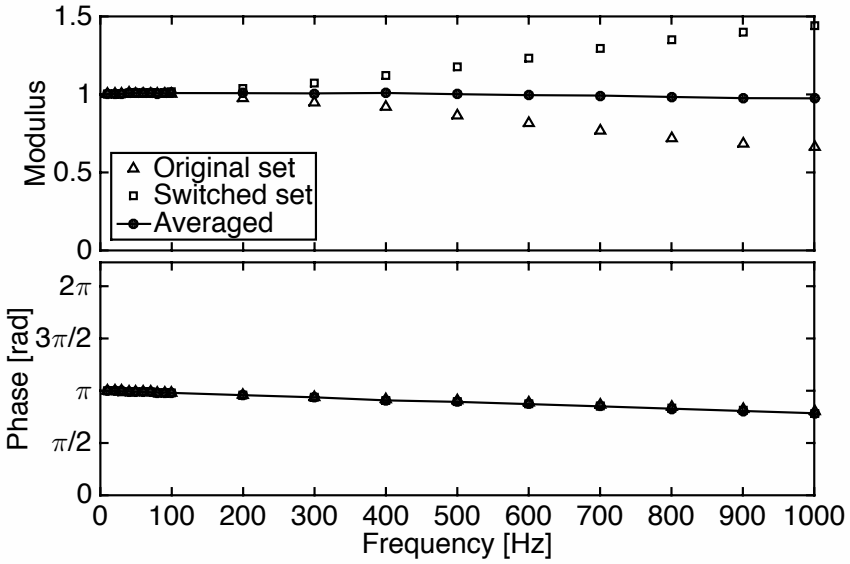

Figure 3.3: *Reflection coefficients at the outlet of the cylindrical tube.* $M_u = 0.002$

the method. The gain and the phase angle of the reflection coefficient measured by the Two-Microphone Method with and without microphone switching are summarised in Fig. 3.3. In the two sets of experiment, the differences in the gain of the reflection coefficient increases with the modulation frequency. The averaged gain equals to 1 and drops slightly as the frequency increases, which is in good agreement with the radiative impedance of an open circular duct (see Eq. 1.27). The values of the phase angle are similar with or without the correction of microphone phase-mismatch errors.

3.2.2 Three-Microphone Method

In the TAFG system, turbulence is generated in the flow passing the cylindrical tube and interferes with the microphones. The pressure signals may also include flow-induced pressure fluctuations in addition to the acoustic contribution from loudspeaker forcing. This reduces the measurement accuracy of the transfer function H_{21}. The Three-Microphone Method is implemented in order to remove the noise effects.

The reference microphone 3 is fixed at position x_1 (see Fig. 3.2) before and after switching the positions of microphone 1 and 2. Assuming that flow noise is uncorrelated on different measurement positions, they are equivalent to white noise in the pressure signals. This assumption has been verified and shown satisfied for low Mach number flows (Åbom 1988). Thus the transfer function

H_{21} without noise contamination can be recovered from the corrupted one ${H_{21}}^c$ by:

$$H_{21} = {H_{21}}^c \cdot C \tag{3.9}$$

where C is the coherence factor determined from the coherence function of the three microphones signals C_{12}, C_{23} and C_{31}:

$$C = \frac{C_{23}}{C_{12}C_{31}} \tag{3.10}$$

Combined with the microphone switching technique, the transfer function H_{21} measured by Three-Microphone Methods writes:

$$H_{21} = \sqrt{{H_{21}}^{or} C^{or} \cdot {H_{21}}^{sw} C^{sw}} \tag{3.11}$$

3.3 Compensation of temperature fluctuations measurement by Two-Thermocouple Method (TTM)

3.3.1 Review of previous works

The dynamic response of common thermocouples depends on the wire material, diameter and connectors. In a time-varying temperature field, it is generally necessary to compensate the temperature signals for these effects. The difference between the wire temperature T_w and the real gas temperature T_g can be established in Eq. 3.12 based on energy balance (Kar et al. 2004).

$$T_g - T_w = \frac{\rho_w C_w d}{4h}\frac{\partial T_w}{\partial t} - \frac{\kappa_w d}{4h}\frac{\partial^2 T_w}{\partial x^2} + \frac{\varepsilon_w \sigma_{\mathrm{SB}}}{h}(T_w^4 - T_{surr}^4) \tag{3.12}$$

Here:

ρ_w = wire density (kg/m^3)

C_w = heat capacity of wire (J/kg/K)

h = heat transfer coefficient (W/m^2/K)

κ_w = thermal conductivity of wire (W/m/K)

ε_w = emissivity of wire

σ_{SB} = Stefan-Boltzmann constant

On the right-hand side of Eq. 3.12:

- $\frac{\rho_w C_w d}{4h}\frac{\partial T_w}{\partial t}$ is the dynamic error due to the finite mass of thermocouple.
- $-\frac{\kappa_w d}{4h}\frac{\partial^2 T_w}{\partial x^2}$ is the error due to the conductive heat transfer along the wire.
- $\frac{\varepsilon_w \sigma_{\mathrm{SB}}}{h}(T_w^4 - T_{surr}^4)$ is the error due to the radiative heat transfer from the wire to the connectors.

In this work, the thermocouples are designed with fine long wires and the flow temperature is relatively low. Conductive and radiative errors are minimized and negligible compared to the convective heat transfer. So Eq. 3.12 can be simplified to :

$$\frac{dT_w}{dt} = \frac{1}{\tau}(T_g - T_w) \tag{3.13}$$

where τ is the thermocouple time constant equal to $\rho_w C_w d/4h$. Accounting only for the convective effects, the natural time constant of a thermocouple writes (Forney and Fralick 1995b):

$$\tau = k d^{2-m} V^{-m} \tag{3.14}$$

where k is a coefficient dependent of the fluid and the wire properties, V is the flow speed and m is the exponential of the Reynolds number in Nüsselt correlation. $m = 0.5$ if the thermocouple works under forced convection regime and $m = 0.25$ under natural convection regime (Taine and Iacona 2011). The time constant of the 25 μm K-type thermocouple calibrated by the provider and in dry air at temperature 38^{o}C is 50 ms in still air and 4 ms at 18.5 m/s flow speed. It is noted that the above equation for τ is derived from the empirical equation of Nüsselt number in a steady flow and that time constant may also change with temperature. The time constant induces both amplitude attenuation and time lag in the measurement with respect to the true gas temperature. It is thus necessary to compensate these effects in order to evaluate H_{42} in Eq. 3.4 with accuracy.

Two-Thermocouple Method (TTM) have been widely used to estimate thermocouple time constant and to reconstruct gas temperature. It usually involves two closely placed thermocouples made of same alloy but with different wire diameters. The dynamic response of the two thermocouples is expressed in Eqs. (3.15)-(3.16).

$$\frac{dT_{w1}}{dt} = \frac{1}{\tau_1}(T_{g1} - T_{w1}) \tag{3.15}$$

$$\frac{dT_{w2}}{dt} = \frac{1}{\tau_2}(T_{g2} - T_{w2}) \tag{3.16}$$

Here the subscript 1 stands for the faster thermocouple.

Many previous works have contributed to the measurement of thermocouple time constants and the reconstruction of gas temperatures by assuming that $T_{g1} = T_{g2} = T_g$. This is reasonable because the thermocouples are made of the same alloy and are submerged in the same flow at a small spatial distance.

Early work of Strahle and Muthukrishnan (1976) have tried to measure thermocouple time constants from the cross correlation of the thermocouple signals. The real and imaginary part of the complex cross-correlation coefficients have been investigated separately. The high frequency limit of the real part of the cross correlation spectrum have been found equal to the ratio of thermocouple time constants. The imaginary part of the cross correlation spectrum presents a local maximum, which has been found located on the frequency equal to the inverse of one of the time constants.

The Time domain reconstruction (TDR) method supposes that the ratio of thermocouple time constants:

$$\alpha = \frac{\tau_2}{\tau_1} = \left(\frac{d_2}{d_1}\right)^{2-m} \tag{3.17}$$

is invariant, although individual time constant may change in time. On can thus obtain straightforwardly the time constant and reconstructed gas temperature:

$$\tau_1 = \frac{T_{w2} - T_{w1}}{\alpha \frac{dT_{w2}}{dt} - \frac{dT_{w1}}{dt}} \tag{3.18}$$

$$T_g = \frac{\alpha(\frac{dT_{w2}}{dt} / \frac{dT_{w1}}{dt})T_{w1} - T_{w2}}{\alpha(\frac{dT_{w2}}{dt} - \frac{dT_{w2}}{dt}) - 1} \tag{3.19}$$

One drawback of the time domain method is that the calculation of τ is very sensitive to noise and may produce non realistic results. One may think of using signal smoothing techniques to solve the problem, but smoothing filters should be designed carefully to avoid adding time lag.

The Frequency domain reconstruction (FDR) method (Forney and Fralick 1994; Forney and Fralick 1995a) avoids to calculate time derivative by taking the Fourier transform of the time signals. Substituting Eq. (3.14) into Eq. (3.15) and (3.16) then applying the Fourier transform gives:

$$i\omega\hat{T}_{w1} = \frac{1}{kd_1^{2-m}}(\hat{T}_{vg} - \hat{T}_{vw1}) \tag{3.20}$$

$$i\omega\hat{T}_{w2} = \frac{1}{kd_2^{2-m}}(\hat{T}_{vg} - \hat{T}_{vw2}) \tag{3.21}$$

$$\text{with} \quad \hat{T}_{vg} = FFT(V^m T_g) \tag{3.22}$$

$$\hat{T}_{vw1} = FFT(V^m T_{w1})$$

$$\hat{T}_{vw2} = FFT(V^m T_{w2})$$

With the knowledge of the time constant ratio α, the reconstructed gas temperature writes:

$$\hat{T}_{vg} = \frac{\alpha \hat{T}_{w2}\hat{T}_{vw1} - \hat{T}_{w1}\hat{T}_{vw2}}{\alpha \hat{T}_{w2} - \hat{T}_{w1}} \tag{3.23}$$

$$T_g = \frac{1}{V^m} FFT^{-1}(\hat{T}_{vg}) \tag{3.24}$$

The equation shows that the knowledge of the flow speed is necessary to reconstruct gas temperature. But in a constant flow, Eq. (3.24) becomes:

$$\hat{T}_g = \frac{(\alpha - 1)\hat{T}_{w1}\hat{T}_{w2}}{\alpha \hat{T}_{w2} - \hat{T}_{w1}} \tag{3.25}$$

O'Reilly et al. (2001) proposed a non-linear state estimation method, which uses an extend Kalman filter to estimate true gas temperature. O'Reilly's method has shown better temperature reconstruction results than frequency domain method, although they have similar capacity of increasing signal bandwidth. More recently Hung et al. (2005) proposed a difference equation (DE) approach of the two-thermocouple system identification. The system is first characterised by an autoregressive model with noisy input and output and a generalised total least squares algorithm is then used to give unbiased estimation of the time constants. The advantage of this method is that it makes no assumption on time constant or time constant ratio.

In real conditions, true gas temperature may be different on the two thermocouple locations. In this case Tagawa and Ohta (1997) proposed a Least squares (LS) method, which estimates the thermocouple response time by minimizing the sum of the squares of the differences of the true gas temperature in a sliding window. However, it was found that the gradient evaluations in the LS method is prone to noise and it tends to underestimate the time constant, or even to give non-physical negative time constants. Indeed, the signal conditioner and acquisition system may also contribute to the differences between the temperature signals. An improved version of LS reconstruction method (Tagawa et al. 1998) minimize noise effects by maximizing the signal similarity, although it is trivial for mono-frequency signals.

To the author's knowledge, it seems that few methods can deal with signal noise without reducing the reconstruction bandwidth. For all the methods presented above, high frequency content in raw signals is often removed out in order to obtain a rational estimation of the time constants and reconstructed temperature signal. This is however not intended in the current work. An alternative method using the transfer function of the thermocouples has been developed in the next section to estimate thermocouple time constants.

3.3.2 Estimation of time constants with the transfer function of thermocouples

In the TAFG system, the flow speed evolves in time due to the acoustic modulation. It is probable that thermocouple time constant also varies in time. According to Eq. (3.14), the relative change of the time constants is proportional to the relative change of the flow speed by $\delta\tau/\tau = -m\delta V/V$. m is equal to 0.5, so a 20% increase in the flow speed would reduce 10% of the time constant. For the first-order lag system represented by Eq. (3.13), the gain g and phase angle θ of the system transfer function is determined by the time constant, as shown in Eq. (3.26) and (3.27). In the low frequency range the system transfer function is not sensitive to the change of time constants. In the high frequency range a 10% change of the time constant would cause no more than 10% difference of the gain and 0.2 rad for the phase lag. The time constant of common thermocouples, including the fast response ones, is usually between several milliseconds and seconds. The related cut-off frequency of the lag system, taken when the gain $g = 1/\sqrt{2}$ or -3 dB, is between 15 to 1 Hz, which are rather small compared to the modulation frequencies used in the experiments. This means that the lag system reaches already the low gain ($g \to 0$) and high phase ($\theta \to -\pi/2$) limit such that the oscillation of time constant affects merely the system's transfer function. The thermocouple time constants are therefore supposed invariant in time in the following estimation procedure. The eventual error related with this assumption adds to the error of the time constant estimation procedure presented in the following.

$$g = \frac{1}{\sqrt{1+(\omega\tau)^2}} \qquad \frac{\delta g}{g} = -\frac{(\omega\tau)^2}{1+(\omega\tau)^2}\frac{\delta\tau}{\tau} \tag{3.26}$$

$$\theta = \operatorname{atan}(\omega\tau) \qquad \delta\theta = \frac{2(\omega\tau)^2}{1+(\omega\tau)^2}\frac{\delta\tau}{\tau} \tag{3.27}$$

From the Fourier transform of Eq. (3.15) and (3.16), it is convenient to calculate the transfer function of thermocouple 2 to 1 $H_{2tc} = \hat{T}_{w2}/\hat{T}_{w1}$:

$$H_{2tc} = \frac{1+i\omega\tau_1}{1+i\omega\tau_2} = \frac{1+\omega^2\tau_1\tau_2}{1+\omega^2\tau_2^2} + i\frac{\omega(\tau_1-\tau_2)}{1+\omega^2\tau_2^2} = r + ix \tag{3.28}$$

It should be noted that the instrumental transfer functions of the thermocouple conditioners are considered as the same here. The real (r) and imaginary (x) part of H_{2tc} can be used in a reversed way to determine the time constants (see Eq.(3.29)).

$$\omega\tau_2 = \frac{r-1}{x} \qquad \omega\tau_1 = \frac{r(r-1)}{x} + x \tag{3.29}$$

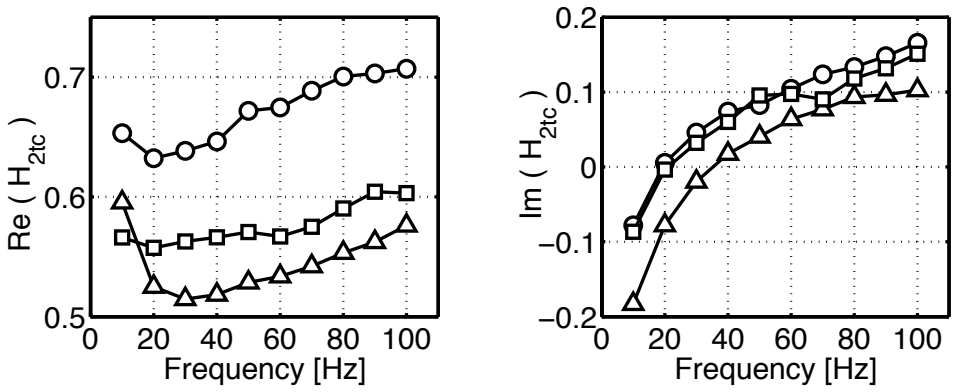

(a) (b)

Figure 3.4: *Real (left) and imaginary (right) part of the transfer functions of thermocouple 2 to 1. ◯: D12-1. △: D12-2. □: D06-1*

The real and imaginary part of the transfer function of the thermocouple 2 (slower) to 1 (faster) H_{2tc} are traced in Fig. 3.4 for all the three operating conditions. They are calculated using the Welch periodogram method examined at the forcing frequency f. The input signals to calculate the transfer functions are exactly the raw data recorded during 10 s at 8192 Hz. For consistency, all the calculations of transfer functions presented in this part of the thesis use the same protocol.

The parabolic form of the curves in Fig. 3.4(a) corresponds well to the expression of r in Eq. (3.29). Normally the imaginary part of H_{2tc} should be negative for all frequencies since $\tau_1 < \tau_2$. However, the curves in Fig. 3.4(b) all increase to positive values for frequencies beyond 10, 20 and 30 Hz respectively for configuration D12-1, D06-1 and D12-2. The differences in thermocouple conditioners are not the only cause of such abnormality otherwise these curves should have collapsed with each other. Nevertheless, the two curves in Fig. 3.4(b) of similar flow condition (D12-1 and D06-1) match with each other, and the curve for a higher flow velocity (D12-2) has gained 10 Hz in the band where the imaginary part of H_{2tc} is negative. This is reasonable because the time constants are smaller in higher velocity flow. Finally the abnormal results are again due to the difficulty in generating high amplitude temperature fluctuations in higher frequency range. Without a reference true gas temperature, there seems to be no reason to estimate the time constant using the transfer function at frequencies beyond 10 Hz.

The time constants of the two thermocouples for all three cases are summarised in Table 3.1. They are calculated from the value of the transfer function H_{2tc} at 10 Hz. The ratio α of the two time constants are slightly different in three

Table 3.1: *Estimation of time constants using signals at 10 Hz modulation*

Cases	D12-1	D12-2	D06-1
τ_1 [ms]	45	18	44
τ_2 [ms]	71	35	80
$\alpha = \tau_2/\tau_1$	1.58	1.94	1.82
e_τ	$\pm 13\%$	$\pm 11\%$	$\pm 8\%$

operating conditions. The relative errors of the time constants estimation e_τ is calculated by $\pm m V_{\text{rms}}/V_{\text{mean}}$ with $m = 0.5$, so only the empirical temporal evolution of the time constant as a function of the flow speed have been accounted for the estimation errors.

The estimations with some of the methods presented in the previous section have also been plotted in Fig. 3.5, and their input parameters can be found in Table 3.2. For these methods, raw thermocouple signals have been first normalised to the mean temperature. This removes the different DC offsets caused by thermocouple conditioners. For some methods the raw signals have been smoothed by a 4th order Savitzky-Golay filter (Savitzky and Golay 1964), which gives additionally the filtered first time derivative of the raw signals. The smoothed time derivative is used later in time domain reconstruction method (see Eq.(3.19)).

The mean time constants given by the LS method merely differ between the three operating conditions, which is physically incorrect because the flow speed is quite different. The DE method gives more reasonable estimation of the time constant, because the mean time constants are similar in the two conditions with a slower flow (D12-1 and D06-1) and higher than in a faster flow (D12-2). The deviation of the estimated time constants from the mean value are obviously smaller in the case D12-2 where the flow Mach number is 0.05. This has been observed for both LS and DE methods, showing that the estimations in D12-2 configuration are most reliable. Finally the mean time constants obtained from the thermocouple transfer functions (see Table 3.1) agree well with those obtained from the DE method with smoothed input signals. The mean time constants and the raw signals are used in the next section to reconstruct gas temperature according to Eq. (3.30).

$$T_{g1} = FFT^{-1}\left((1 + i\omega\tau_1) \cdot \hat{T}_{w1}\right) \qquad T_{g2} = FFT^{-1}\left((1 + i\omega\tau_2) \cdot \hat{T}_{w2}\right) \quad (3.30)$$

3.3.3 Reconstruction of temperature signals

Using the time constants estimated from the transfer function of the two thermocouples, gas temperature has been reconstructed for the operating condition

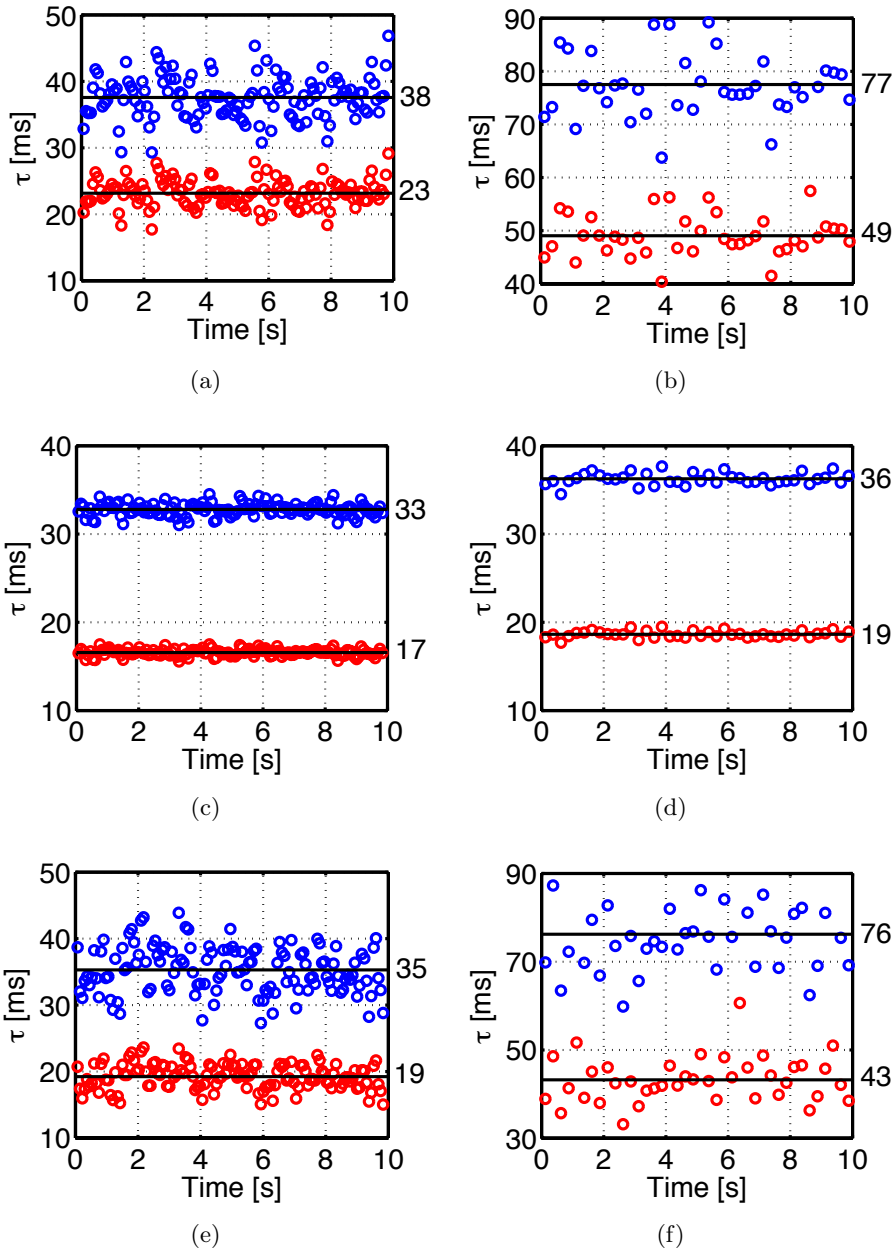

Figure 3.5: *Estimation of thermocouple time constants by LS method (left column) and DE method (right column) for the cases D12-1 (top), D12-2 (middle), D06-1 (bottom). Red symbols: τ_1. Blue symbols: τ_2. The mean value is traced in black line with annotations on the right border of the figures. All input signals have been smoothed with Savitzky-Golay filter.*

Table 3.2: *Input parameters for TTM reconstruction methods*

Method	Input parameters
TDR	α referred to Table. 3.1
FDR	constant flow velocity, α referred to Table. 3.1
LS	sliding window duration $\Delta t = 0.15$ s window overlapping 0.5 Δt
DE	sliding window duration $\Delta t = 0.15$ s, ratio of signal noise variances of thermocouple 1 to 2 $\Phi = 0.93$

D12-2 at 10 Hz modulation. This method is called the H_{2tc} method in the following texts. The previous TDR, FDR, LS and DE methods have also been used to reconstruct temperature fluctuations measured in the TAFG system. The input parameters are summarised in Table 3.2. The reconstructed gas temperature are summarised in Fig. 3.6 together with the original thermocouple signals. For all the methods, the reconstructed gas temperature T_{g1} and T_{g2} almost superpose with each other, so only T_{g1} is traced in the figures. The reconstruction using smoothed input datasets are designated by the method name plus a suffix '-SG'. Particularly, TDR method uses also the smoothed first time derivative of the raw signals.

In Fig. 3.6(a), the amplitude of reconstructed gas temperature are similar for the time and frequency domain method, but the TDR method failed to capture the time lag between the reconstructed and original signals. The FDR method show some high-order harmonics of 10 Hz. This is a deficiency of the method, already been reported in O'Reilly et al. (2001), which occurs when the denominator in Eq.(3.25) becomes null. The LS and DE methods give similar reconstructed gas temperature and both have produce high frequency fluctuations compared with the original signals. They are also in good correspondence with the gas temperature reconstructed by the H_{2tc} method . However, the primary results from H_{2tc} method were very noisy. In Fig. 3.6(c), the high frequency fluctuations has been either smoothed out with the Savitzky-Golay filter, or reduced by averaging the Fourier spectrum of several 1-second segmentations of the total 10-second signals.

To draw a conclusion of the H_{2tc} method for compensating the temperature measurement by the two-thermocouple sensor, the time constants of the thermocouples in each flow configuration can be estimated within a good confidence range at 10 Hz. These constants were then supposed the same over the whole frequency range (10 - 100 Hz) and were used to reconstruct temperature fluctuations at all the modulation frequencies. The root-mean-square of the reconstructed temperature signals are summarised in Fig. 3.7.

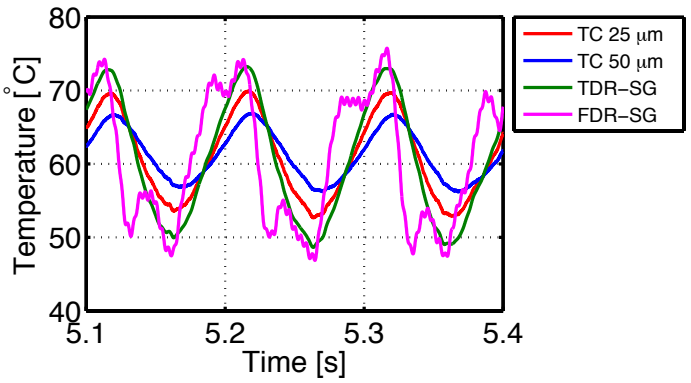

(a)

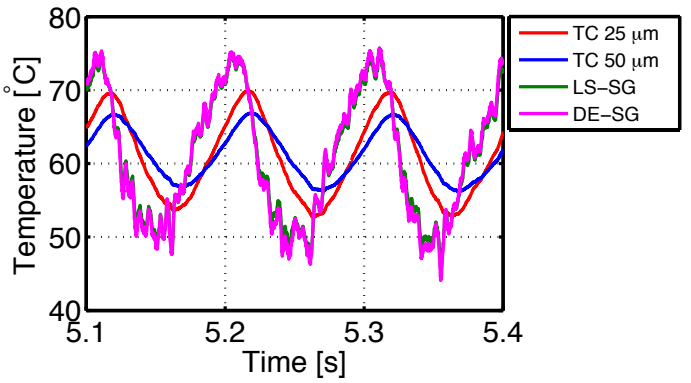

(b)

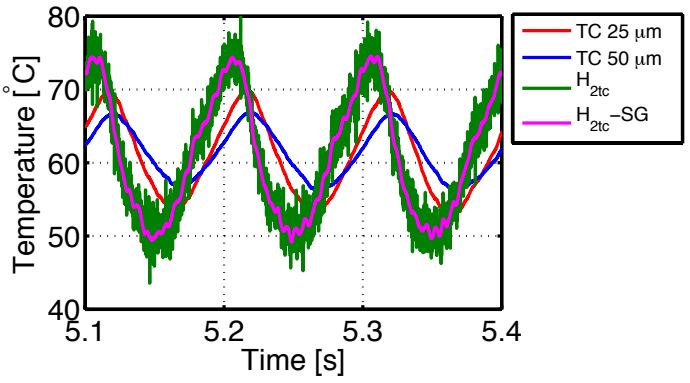

(c)

Figure 3.6: *Reconstructed gas temperature using different methods in the operating condition D12-2 at 10 Hz modulation*

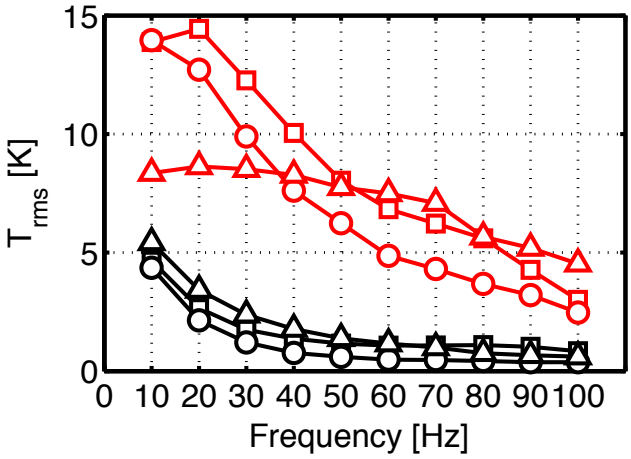

Figure 3.7: *Root-mean-square value of the temperature fluctuations as a function of modulation frequency. Black symbols: original signals. Red symbols: reconstructed signals. ◯: D12-1. △: D12-2. □: D06-1*

3.4 Determination of the upstream perturbation variables in the TAFG setup

Using the nozzle reflection coefficient $\mathcal{R}$ measured by the Three-microphone method, and the time constant estimation τ_1 for thermocouple 1 (25 μm), the complex ratio $H_{42} = \hat{T}_g/\hat{p}_2$ in Eq. (3.4) can be estimated from the raw temperature and pressure signals using Eq. (3.31). However no correction of the phase mismatch for one single microphone was made in this expression.

$$H_{42} = (1 + i\omega\tau_1)\frac{\hat{T}_{w1}}{\hat{p}_2} \tag{3.31}$$

By the combination of Eq. (3.4) and (3.31), the complex ratio of incident entropy wave to acoustic wave $H_{sa} = \sigma/P_u^+$ have been calculated for all operating conditions as a function of the forcing frequency. The modulus $|H_{sa}|$ and the phase angle $\varphi = \arg(H_{sa})$ are plotted in Fig. 3.8. For the three configurations explored, the modulus decreases above 20 Hz as the modulation frequency rises. This low-pass filter behavior that was already illustrated in Sec. 2.3 is a characteristic of the TAFG system. High frequency temperature fluctuations are difficult to generate and are smoothed out due to mixing with the main stream, dispersion and dissipation. Compared with the configuration D12-1, reducing the nozzle outlet diameter (D06-1) or raising the flow velocity (D12-2) both increase the mean pressure in the system. This would cause a drop of the pressure difference across the jet ducts and the amplitude of pressure fluctuations p' (see Appendix A) needs to be increased in order to maintain the same velocity modulation amplitude. The combination of the two facts lead to the drop of the

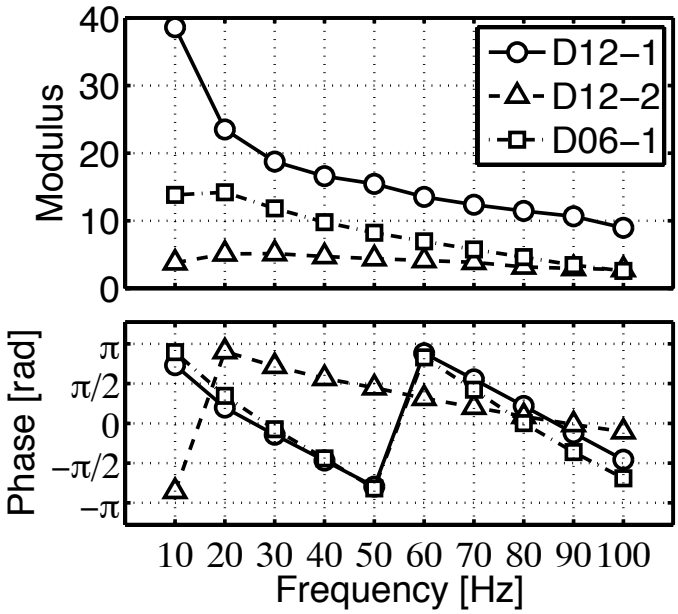

Figure 3.8: *Modulus and phase angle of the complex ratio* $H_{sa} = \sigma / P_u^+$.

momentum of the cross flow jets, thereby the amplitude of the temperature fluctuations decreases in the TAFG system. The phase angle φ varies quasi-linearly with the forcing frequency in Fig. 3.8. The phase velocity $\partial\varphi/\partial f$ is similar in the two configurations with similar flow Mach numbers and for the D12-1 condition, $\partial\varphi/\partial f = -0.1$ rad/Hz. This value is very close to the phase change calculated with the different propagation speeds of acoustic and entropy waves. The zero-frequency limit of the phase angle for the three operation conditions all tend toward $\pm\pi$, which corresponds well with the quasi-steady analysis of the TAFG setup presented in Appendix A.

Finally the acoustic waves P_u^+, P_u^- can be determined from the measured reflection coefficient $\mathcal{R}$ and the pressure signal at position x_2 according to Eqs. (3.2)-(3.3). Combined with the previously evaluated H_{sa}, it is then convenient to evaluate the entropy wave using $\sigma = H_{sa} P_u^+$. These sets of post-treatments have been conducted for each modulation frequency ranging from $f = 10$ to 100 Hz and results at $f = 20$ and $f = 100$ Hz are listed in Table 3.3 together with the inflow conditions. These upstream variables can also be determined by the same methods on position x_4, which constitute the inputs of numerical simulations of the TAFG test bench that are presented in the next chapter.

Table 3.3: *Upstream perturbation variables at the inlet of the nozzle with the flow and modulation conditions*

NO.	f [Hz]	P_u^+	$P_u^- e^{i\varphi_a}$	$\sigma e^{i\varphi_s}$	$u_{\mathrm{rms}}/u_{\mathrm{mean}}$	M_u
1	20	0.0019	$0.0014e^{+3.12i}$	$0.0441e^{+0.62i}$	0.24	0.017
2	100	0.0010	$0.0008e^{+3.06i}$	$0.0089e^{-1.44i}$	0.14	0.017
3	20	0.0074	$0.0040e^{+2.57i}$	$0.0375e^{+2.83i}$	0.22	0.050
4	100	0.0067	$0.0028e^{+2.89i}$	$0.0185e^{-0.33i}$	0.17	0.050
5	20	0.0035	$0.0021e^{+0.93i}$	$0.0496e^{+1.08i}$	0.17	0.016
6	100	0.0039	$0.0015e^{+0.37i}$	$0.0102e^{-2.17i}$	0.20	0.016

Chapter 4

Separation of direct and indirect noise contributions

The method to measure the direct and indirect reflection coefficients $\mathcal{R}_a$ and $\mathcal{R}_s$ is presented in this chapter. It consists of making the difference of the nozzle reflection coefficients $\mathcal{R}$ measured in two sets of experiment. In the first set of experiments, the main flow and the crossflow jets are at the same temperature, while in the second set of experiments they are at different temperatures. In this way entropy fluctuations can be switched off and on respectively in the first and second set of experiments. The direct and indirect reflection coefficients are then derived from the nozzle reflection coefficients measured when entropy fluctuations are switched on/off and complex ratio of incident entropy to acoustic waves H_{sa} presented in the Sec. 3.4. The strategy has been first validated by the SUNDAY solver then applied to experimental data.

4.1 Separation method for direct and indirect noise contributions

A recapitulation of the waves in the upstream region of the nozzle and the measurement positions is shown in Fig. 4.1. When the nozzle is submitted to simultaneous acoustic and entropy forcing, P_u^+ and σ respectively, there are direct and indirect contributions in the reflected wave P_u^-. The objective here is to evaluate separately the two type of contributions by means of measuring the direct and indirect nozzle reflection coefficients, $\mathcal{R}_a$ amd $\mathcal{R}_s$ respectively.

Admitting linear perturbations, the direct and indirect contributions to the noise field add straightforward to each other. So that the reflection coefficient

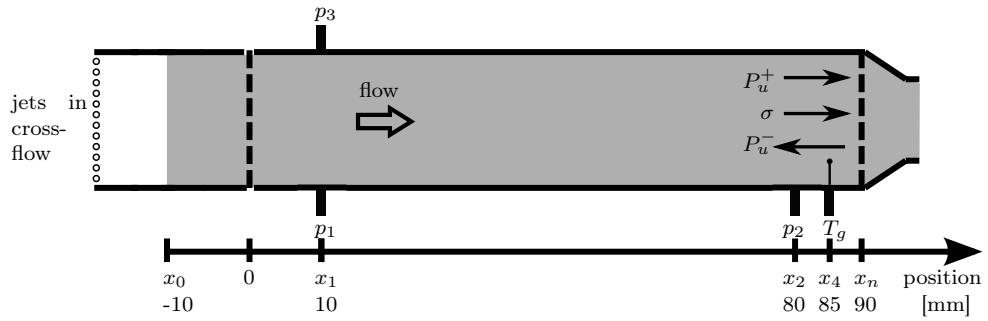

Figure 4.1: *Schematic view of waves and measurements in the upstream domain of the nozzle. The grey area corresponds to the numerical calculation domain for the code SUNDAY*

$\mathcal{R}$ at x_n measured in the Sec. 3.2 is related to the complex ratio $H_{sa} = \sigma/P_u^+$, the reflection coefficients $\mathcal{R}_a$ and $\mathcal{R}_s$ by:

$$\mathcal{R} = \frac{P_u^-}{P_u^+} = \frac{\mathcal{R}_a P_u^+ + \mathcal{R}_s \sigma}{P_u^+} = \mathcal{R}_a + \mathcal{R}_s H_{sa} \tag{4.1}$$

One possibility to determine the reflection coefficients is to compare two operating regimes where the direct and indirect reflection coefficients $\mathcal{R}_a$ and $\mathcal{R}_s$ are kept constant, but the complex ratio $H_{sa} = \sigma/P_u^+$ are different. For compact nozzles, it has been shown in Sec. 1.2 that the reflection coefficients $\mathcal{R}_a$ and $\mathcal{R}_s$ only depend on the inlet and outlet Mach numbers of the nozzle and the boundary conditions at the nozzle outlet, they are independent of the forcing waves as long as in linear regime. This property allows to deduce the indirect nozzle reflection coefficient $\mathcal{R}_s$ from Eq. (4.1) using measurements in the first regime without entropy fluctuations $\sigma = 0$ (A) and in the second regime with entropy fluctuations $\sigma \neq 0$ (B). These two regimes can be realised in the TAFG setup by maintaining the mainstream and cross jet flows at either the same temperature (A) or different temperatures (B). In regime (A), entropy fluctuations vanish and the reflection coefficient $\mathcal{R}$ is simply given by:

$$\mathcal{R}(\sigma = 0) = \mathcal{R}_a \tag{4.2}$$

The mean flow fields in regimes (A) and (B) need to be the same while air is injected in the cross jet flows at a different temperature. Modifying the air temperature in cross jet flows alters the speed of sound in the upstream flow, and this in turn modifies the inlet Mach number M_u. An analysis of the sensitivity of reflection coefficient $\mathcal{R}_a$ to a change of the inlet Mach number M_u has thus been carried out. Two baseline flows were considered with $M_u = 0.017$ and $M_u = 0.050$ and with relative variations of the Mach number within the range of $\Delta M_u/M_u = \pm 7\%$ around these values. These conditions cover the range of variations of the speed of sound resulted from the largest mean temperature difference of 50 K that was measured in the TAFG setup (see Table 2.2). The

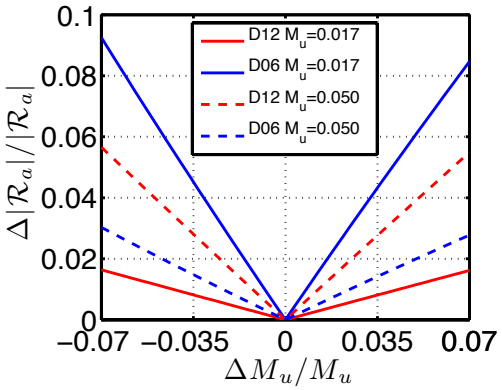

Figure 4.2: *Sensitivity of analytical reflection coefficient $\mathcal{R}_a$ as a function of relative variation of Mach number M_u for nozzles D12 and D06.*

relative change $\Delta|\mathcal{R}_a|/|\mathcal{R}_a|$ of the modulus of the reflection coefficient $\mathcal{R}_a$ is plotted in Fig. 4.2 for two nozzles D06 and D12. In these calculations, the distance L is equal to 2 mm, the end correction $\delta = 0.61a$ and the reflection coefficient at a distance $L + \delta$ from the nozzle outlet has been fixed to -1 for both nozzles.

In the four cases the sensitivity of $\mathcal{R}_a$ increases linearly with the relative change of the inlet Mach number M_u. At smaller Mach number, the direct reflection coefficient of the nozzle D06 is more sensitive to the change of the inlet Mach number than the nozzle D12, while the tendency is inverted at the larger Mach number. This is caused by the reflective boundary condition downstream of the nozzle, which induces a phase lag $2\pi fL/c(1+M_d) + 2\pi fL/c(1-Md)$ between the progressive and regressive acoustic waves downstream of the nozzle. This phase lag is very sensitive to the change of outlet Mach number M_d. The sensitivity of the direct reflection coefficient remains limited to 10% within the range of Mach numbers explored. Indeed, this effect can not be ignored, but a series of experiments attempting to keep the same inlet Mach numbers in regimes without and with entropy perturbations have failed due to the difficulty to control the temperature of the jets in crossflow. This effect is eventually treated as uncertainties. One should note that in case of a choked nozzle the sensitivity of the reflection coefficient to the inlet Mach number is below 1% for a large range of M_u up to 0.1.

Finally by subtracting Eq. (4.2) from Eq. (4.1), one deduces:

$$\mathcal{R}_s = \frac{\mathcal{R}(\sigma \neq 0) - \mathcal{R}(\sigma = 0)}{H_{sa}} \tag{4.3}$$

The the strategy formulated in the above expression is designated thereafter by the diff-R methods. It requires the measurements of the nozzle reflection coefficient $\mathcal{R}$ and the complex ratio H_{sa} of the entropy to acoustic waves propagating

to the nozzle. The two parameters can be determined from the experimental methods presented in Sec. 3.2 and Sec. 3.4.

The diff-R method has been developed based on the assumptions of small-amplitude pressure, velocity and temperature fluctuations. Although the implementation of the diff-R method presented here has been dedicated to compact nozzles, it also applies to finite-length nozzles as long as the nozzle response stays linear. This is supported by the analytical solutions derived for non-compact nozzle in Marble and Candel (1977); Moase et al. (2007); Durán and Moreau (2013); Giauque et al. (2012), which are frequency-dependant, yet determined by the inlet and outlet Mach numbers for a given nozzle under certain inflow condition and at a single forcing frequency.

In the next section, the flow with acoustic and entropy perturbations approaching the nozzle in the TAFG setup is calculated by an Eulerian code at several forcing frequencies. This gives numerical pressure and temperature signals that are used to validate the diff-R method by comparing the direct and indirect reflection coefficients to their analytical solutions.

4.2 Numerical validation of the diff-R method by the SUNDAY code

Simulations of the test bench TAFG were carried out with a dedicated code SUNDAY (SimUlation of Noise in 1D flows due to fluctuAtions in entropY) at ONERA developed by Giauque et al. (2012); Huet and Giauque (2013). It solves quasi-one-dimensional linear and nonlinear Euler equations of flows in a channel with variable section. The nonlinear simulations uses the Riemann invariants which are defined by:

$$2\Gamma^{\pm} = \frac{2}{\gamma - 1}\left(\left(1 + \frac{p'}{p}\right)^{(\gamma-1)/2\gamma} - 1\right) \pm \frac{u'}{ce^{\sigma/2}} \tag{4.4}$$

They correspond to the characteristic waves of the hyperbolic system and reduces to $2P^{\pm} = p'/p \pm u'/c$ for small amplitude perturbations. The nonlinear expressions of the characteristic waves allow to couple acoustic and entropy waves along the propagation path. SUNDAY can be used to solve the pressure and temperature field fluctuations within the numerical domain for different nozzle geometries and flow operating conditions. It allows to force the flow with acoustic and entropy waves with reflective or non-reflective boundary conditions at the extremities of the simulation domain. The boundary conditions used in this work are non-reflective at the entrance of the simulation domain (see Fig. 4.1) and fully reflective at the exit. The investigated numerical domain corresponds to the part of TAFG setup downstream the hot air injection

unit starting at x_0 (see Fig. 4.1), where it is assumed that flow disturbances are uniform and have a plane wave structure.

Given the mean flow condition and the incoming harmonic forcing waves of acoustic and entropy at x_0 as input, SUNDAY calculates the temporal evolution of pressure, velocity and temperature in the flow. These signals are recorded at the same positions as in the TAFG setup after the transient waves when the initial conditions have been evacuated. These numerical signals are then sampled at a rate of 8 192 Hz as in the experiments but only during 1 second.

The diff-R method is now used to examine the numerical signals for a configuration with the nozzle D12 at the following conditions:

- Synthetic case: $f = 20$ Hz, $P_u^+ = 0.003$, $\sigma = -0.1$, $M_u = 0.050$, $L + \delta = 5.66$ mm and $T_{\text{mean}} = 473$ K.

This simulated configuration could not be explored experimentally and corresponds to an ideal operating condition, where the amplitude of the temperature fluctuations reaches about 47 K. The diff-R method is then validated by comparing to the analytical nozzle reflection coefficients for this synthetic case, which are $\mathcal{R}_a = 0.482e^{3.13i}, \mathcal{R}_s = 0.006e^{3.13i}$.

Simulation are carried out first by only considering acoustic waves $P_u^+ \neq 0, \sigma = 0$ and then with coexisting acoustic and entropy excitations $P_u^+ \neq 0, \sigma \neq 0$. The velocity modulation in both simulations is 0.9%. The numerical signals are then post-processed with the diff-R method, the modulus and the phase angle of the resulting reflection coefficients are summarised in Fig. 4.1.

In Fig. 4.1(a), the obtained nozzle reflection coefficient with no entropy forcing $\mathcal{R}(\sigma = 0)$ matches exactly with the analytical direct nozzle reflection coefficient $\mathcal{R}_a$, which verifies Eq. (4.2). It is also noted that the nozzle reflection coefficient $\mathcal{R}(\sigma \neq 0)$ measured when acoustic and entropy forcing co-exist is different from $\mathcal{R}(\sigma = 0)$. In this synthetic case the amplitude ratio η_u (Eq. (4.5)) of indirect to direct noise contribution reaches 40%, this is already high to alter the acoustic boundary condition of the tube.

$$\eta_u = \frac{|P_{us}^-|}{|P_{uu}^-|} = |\frac{\mathcal{R}_s}{\mathcal{R}_a}||\frac{\sigma}{P_u^+}| \simeq 40\% \tag{4.5}$$

The indirect nozzle reflection coefficient $\mathcal{R}_s$ evaluated from the diff-R method also agrees well with the analytical value both in modulus and in phase as shown in Fig. 4.1(b). These results proof the efficiency of the diff-R method to measure the direct and indirect nozzle reflection coefficients.

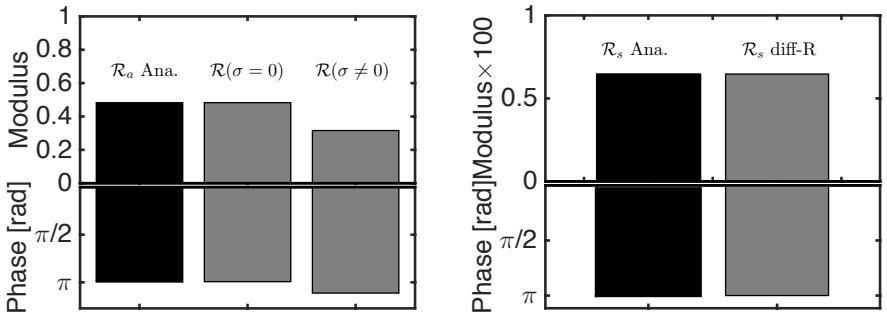

(a) $\mathcal{R}$ (b) $\mathcal{R}_s$

Figure 4.3: *Reflection coefficients obtained from SUNDAY simulations with the diff-R method. Results are compared to analytical values in black bars.*

4.2.1 Sensitivity to signal noise

The sensitivity of the diff-R method to external noise is now examined for two level of random noises that have been added to the ideal signals in the previous synthetic case calculated by SUNDAY.

The noise level is indicated by the signal-to-noise ratio (SNR). For ideal signals SNR $= \infty$. SNR $= 20$ dB corresponds to the highest noise level encountered in the experiments explored. Results for the direct and indirect nozzle reflection coefficients are summarized in Fig. 4.4. The error margins are obtained from 1000 runs with noisy signals.

When noise at SNR $= 20$ dB is added to the ideal excitation signals, the modulus $|\mathcal{R}(\sigma = 0)|$ and $|\mathcal{R}_s|$ obtained with the diff-R method still match well the values found for the ideal signals within a high precision. The precision on the phase angle of both direct and indirect reflection coefficients is however largely corrupted by the noise. The accuracy and precision of the phase angle drop drastically when the SNR is reduced to 10 dB. These tests show that signal noise has significant impact on the diff-R method. Low signal-to-noise values can occur for example in cases with high flow noises in pressure signals or in cases with low amplitude of temperature fluctuations and they be should be carefully examined in experimental conditions.

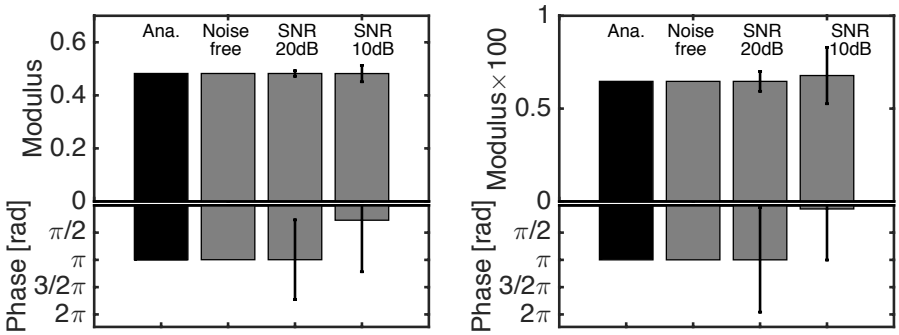

(a) $\mathcal{R}_a$ (b) $\mathcal{R}_s$

Figure 4.4: *Direct (left) and indirect (right) nozzle reflection coefficients obtained from SUNDAY simulations with the diff-R method. Results are compared to analytical values of $\mathcal{R}_a$ and $\mathcal{R}_s$ in black bars. Error bars are obtained from 1000 runs with random noise signals.*

4.2.2 Effects of finite-amplitude convective velocity fluctuations

The diff-R method has been used to measure successfully the direct and indirect nozzle reflection coefficients by a numerical case with small-amplitude perturbations. The conditions explored in the experiments correspond to small inlet Mach numbers that is limited here to $M_u = 0.050$. The maximum amplitude of the pressure fluctuations measured in the TAFG setup is lower than 10^3 Pa for a mean operating pressure of about 10^5 Pa. The temperature fluctuations produced do not exceed 5% of the mean flow temperature. The perturbation equation for entropy fluctuations:

$$\frac{s}{c_p} = \frac{T'}{T} - (\gamma - 1)\frac{p'}{\gamma p}$$

is thus valid and pressure perturbations can be considered in their acoustic limit.

The convective velocity modulation level may however reach relatively high values $u_{\text{rms}}/u_{\text{mean}} = 0.24$ as shown in Fig. 2.11. These velocity disturbances can be neglected compared to the speed of sound but are not negligible compared to the mean velocity. The diff-R method is then examined with the nonlinear simulations of the experimental case NO.1 (see Table 3.3) featuring non-negligible convective velocity modulations. The inflow conditions are recapitulated below:

- Experimental case NO.1 : $f = 20$ Hz, $P_u^+ = 0.0019$, $\sigma = -0.044e^{+0.62i}$, $M_u = 0.017$, $L + \delta = 5.66$ mm $T_{\text{mean}} = 344$ K, and $u_{\text{rms}}/u_{\text{mean}} = 0.24$

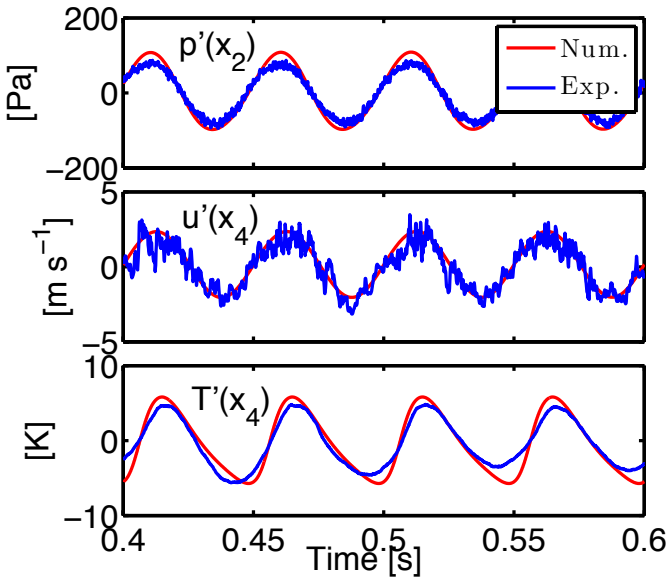

Figure 4.5: *Experimental and numerical signals from SUNDAY for the experimental case NO.1.*

Nonlinear simulation results for the pressure, velocity and temperature fluctuations with the SUNDAY solver are first plotted in Fig. 4.5 together with the experimental signals for the case NO.1. These signals have been synchronized with the experimental pressure signal measured at x_1. The experimental signals are contaminated by high frequency noise, but they are well recovered by the numerical signals. The slight difference between the numerical and experimental signals results from the non-negligible convective velocity modulation, which can be observed from the phase difference $\Delta\varphi_{12}$ between entropy fluctuations at positions x_1 and x_2 (see Fig, 4.1). Fig. 4.6 gives $\Delta\varphi_{12}$ obtained from linear and nonlinear simulations as a function of time. The phase difference calculated with the linear approximation is almost constant in time and has the same value $\Delta\varphi_{12} = -1.4$ rad as the theoretical phase difference $\Delta\varphi_{12} = \omega(x_2 - x_1)/u$ calculated with the bulk velocity $u = 6.3$ m/s of the flow at the angular forcing frequency $\omega = 2\pi f$, where $f = 20$ Hz. In the nonlinear simulations, this phase difference is time-varying and oscillates around the mean value $\Delta\varphi_{12} = -1.4$ rad. These results emphasize that at a given position, entropy fluctuations feature a phase lag that oscillates with time due to the large amplitude of convective velocity fluctuations.

One consequence of this velocity-entropy interaction is that the temperature signal deviates from an ideal harmonic wave, as can be seen in Fig. 4.5. Another consequence is that the incoming pressure and entropy waves have a phase shift that varies in time at the entrance of the nozzle at x_n, although the amplitude

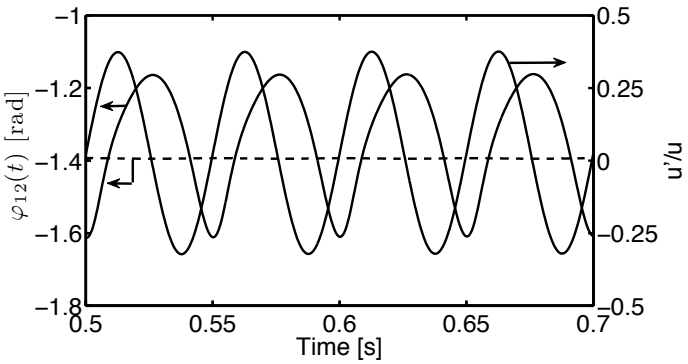

Figure 4.6: *Phase difference $\Delta\phi_{12}$ between entropy waves at x_1 and x_2 (left axis) and convective velocity modulation level u'/u at x_2 (right axis) as a function of time. dashed-line: linear simulation; black-line: nonlinear simulation.*

of this time-varying phase difference remains very small. This phenomenon however has not been considered in the frequency domain analysis conducted in Sec. 3.4 to recover the incoming acoustic and entropy waves, which suppose constant propagation velocity for both acoustic and entropy waves. For acoustic wave alone, the velocity fluctuations are negligible compared to the speed of sound, therefore the measurement of the direct reflection coefficient $\mathcal{R}_a$ in Fig. 4.7 is not affected and still in good agreement with the analytical solution. The large velocity fluctuations however alter the phase angle of the complex ratio $H_{sa} = \sigma/P_u^+$ along the flow path. In the experiments, H_{sa} is evaluated from the pressure signal at x_2 and the temperature signal at x_4, and the resulting phase angle of H_{sa} is only a mean approximation of the true one. This induces errors in the determination of the modulus and the phase of the indirect reflection coefficient $\mathcal{R}_s$, as shown in Fig. 4.7. These errors are difficult to assess *a priori*, but one way to reduce it is to place microphone and the temperature probe as close as possible to the nozzle inlet. Reducing this distance mitigates to some extent the effect of the large velocity fluctuations.

For concluding this section, a series of numerical simulations by the SUNDAY code have proved the efficiency of the proposed diff-R method to measure the direct $\mathcal{R}_a$ and indirect $\mathcal{R}_s$ nozzle reflection coefficients by comparing with the analytical results. The non-linear effect due to large convective velocity modulations has been addressed numerically. The results suggest to mitigate this problem by placing pressure and temperature measurement close to the nozzle inlet. However, the phase accuracy of reflection coefficients R_a and R_s was found strongly dependent on the signal-to-noise ratio. One should pay attentions to these effects while analysing the experimental data with the diff-R method.

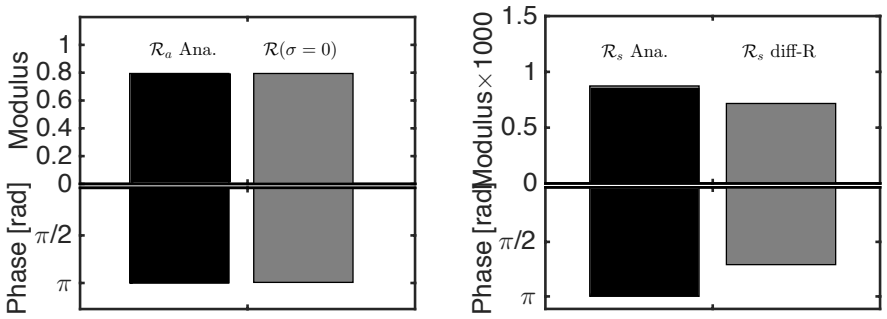

(a) $\mathcal{R}_a$ (b) $\mathcal{R}_s$

Figure 4.7: *Direct (left) and indirect (right) reflection coefficients measured by the diff-R method in the case with finite-amplitude convective velocity fluctuations.*

4.3 Experimental separation of indirect and direct nozzle reflection coefficients

4.3.1 Operating conditions and measurement quality

Experiments are now analysed for the three operating conditions with different nozzles for frequencies from 10 to 100 Hz. They correspond to the conditions explored in Fig. 2.11, where the amplitude of temperature fluctuations are optimized by maintaining at a small level ($< 25\%$) of convective velocity modulation. The inlet and outlet Mach numbers allowing to calculate the direct and indirect nozzle reflection coefficients in the three operation conditions are recapitulated in Table 4.1.

Table 4.1: *Inlet and outlet Mach numbers and the analytical direct and indirect nozzle reflection coefficient for the three operating conditions*

Configs.	M_u	M_d	$\mathcal{R}_a$	$\mathcal{R}_s$
D12-1	0.017	0.047	$0.794e^{3.13i}$	$0.001e^{3.13i}$
D12-2	0.050	0.140	$0.482e^{3.13i}$	$0.006e^{3.13i}$
D06-1	0.016	0.181	$0.353e^{0.01i}$	$0.005e^{3.13i}$

It has been shown in Sec. 4.2.1 that signal-to-noise ratio strongly alters the results when it drops below 20 dB, it is thus worth examining the SNR in the experiments that were carried out. The SNR is calculated here as the logarithm of the ratio of signal power to noise power (Eq. (4.6)) that are evaluated with

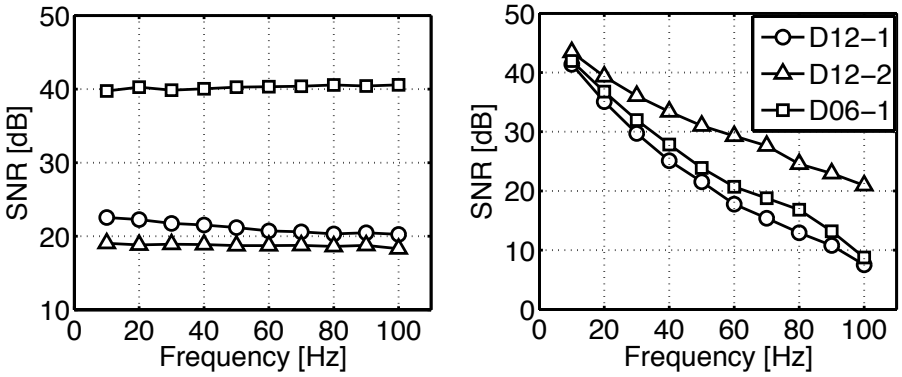

(a) Pressure measurement (b) Temperature measurement

Figure 4.8: *Signal-to-noise ratio of pressure and temperature measurements*

the Welch periodogram method.

$$\mathrm{SNR} = 10 \log_{10} \left(\frac{P_{\mathrm{signal}}}{P_{\mathrm{noise}}} \right) \tag{4.6}$$

The SNR of the raw pressure and temperature signals at each forcing frequency from 10 to 100 Hz are presented respectively in Fig 4.8(a) and (b). The SNR of the pressure measurements in each conditions are almost constant with frequency, while the quality of the temperature measured by the 25 μm thermocouple drops gradually as the frequency increases. This is related to the fact that temperature fluctuations vanishes progressively as the frequency increases in the TAFG system.

In order to study the impact of signal noise on the measurement accuracy and precision of direct and indirect nozzle reflection coefficient under experimental conditions, simulations with the SUNDAY code were carried out for all the operating conditions at two modulation frequencies $f = 20$ amd $f = 100$ Hz. The inputs of the SUNDAY code are determined experimentally with the method presented in Sec. 3.4 and are summarised in Table 3.3. The same procedure as in Sec. 4.2.1 has been employed to measure the direct and indirect reflection coefficients $\mathcal{R}_a$ and $\mathcal{R}_s$ with both ideal signals and random noise added signals. The results obtained with the diff-R method are summarised in Fig. 4.9 and 4.10 and compared to the analytical values computed from inlet and outlet Mach number (see. Table 4.1). There are slight differences between the reflection coefficients calculated analytically and measured by the diff-R method with noise free signals, they result from the differences between the analytical and numerical reflective boundary condition downstream of the nozzle. Without noise, the diff-R method yields results for the reflection coefficients $\mathcal{R}_a$ and $\mathcal{R}_s$ that closely match analytical solutions. The influence of noise on the determination

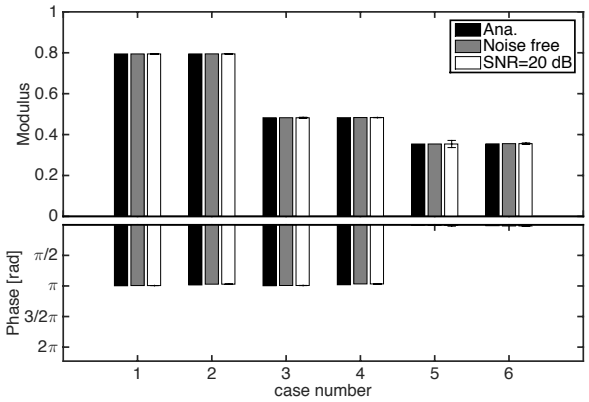

Figure 4.9: *Analytical direct reflection coefficient $\mathcal{R}_a$ and the reflection coefficients $\mathcal{R}(\sigma = 0)$ at nozzle inlet calculated using ideal and noisy signals. The case number corresponds to those in Table 3.3.Error bars are obtained from 1000 runs with random noise signals.*

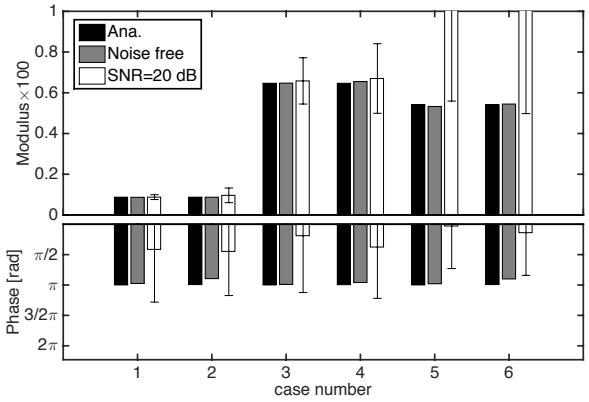

Figure 4.10: *Indirect reflection coefficient $\mathcal{R}_s$ calculated analytically and by the diff-R method using ideal and noisy signal. The case number corresponds to those in Table 3.3. Error bars are obtained from 1000 runs with random noise signals.*

of the direct reflection coefficient $\mathcal{R}_a$ is limited, but errors due to noise seem to be largely amplified for the determination of the indirect reflection coefficient $\mathcal{R}_s$. In particular, the larger of the error bar in the modulus of $\mathcal{R}_s$ increase from operation condition D12-1, D12-2 to D06-1. This tendency has also been observed when using the diff-R method with real experimental signals, as will be discussed below.

4.3.2 Measurement of the nozzle reflection coefficients with the diff-R method

The reflection coefficients at the nozzle inlet are analysed now with experimental pressure and temperature signals when the entropy mode is switched on $\mathcal{R}(\sigma \neq 0)$ and off $\mathcal{R}(\sigma = 0)$. Their modulus and phase angles are plotted in Fig. 4.11 together with the analytical values for $\mathcal{R}_a$. When the mainstream and jets flow are at the same temperature, the measured reflection coefficient $\mathcal{R}(\sigma = 0)$ corresponds well to the analytical value for $\mathcal{R}_a$ except at the very low frequency of 10 Hz. This is due to the low frequency limit of Three-microphone method. The wavelength of the pressure wave at 10 Hz is very long compared to the microphone inter-spacing, and the microphones measure almost the same signals. When air is injected at a higher temperature in the jet flows than in the main stream, the reflection coefficients $\mathcal{R}(\sigma \neq 0)$ differs less at high frequency than at low frequency from the value $\mathcal{R}(\sigma = 0)$. These differences associated with the higher values of temperature fluctuations at low frequencies indicate stronger contribution from indirect noise with respect to the direct noise level at low modulation frequencies. The indirect reflection coefficient $\mathcal{R}_s$ plotted in Fig. 4.12 largely differ from their analytical values. The modulus $|\mathcal{R}_s|$ are in the same order of magnitude as the analytical solutions for all the cases, although the relative difference can be very high.

4.4 Conclusion

The diff-R method proposed in this chapter allows to measure the direct and indirect nozzle reflection coefficients of a nozzle submitted to simultaneous acoustic and entropy forcing. It has been developed based on the assumption of small-amplitude perturbation and has been validated in a numerical case of perturbed subsonic nozzle flow calculated by the SUNDAY solver. Its efficiency has been proven by the good agreement with analytical solutions for compact nozzles.

The experimental validation of the diff-R method proved to be more complex. Some of the reasons why the diff-R method didn't manage to provide expected

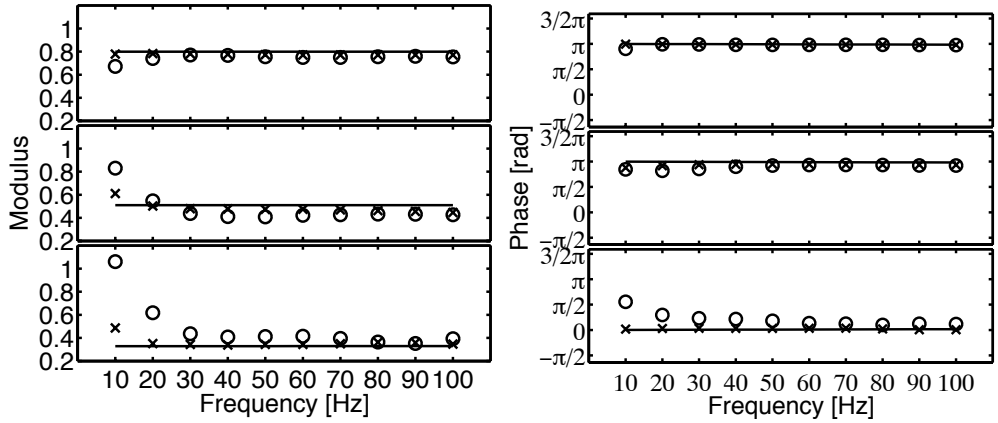

Figure 4.11: *Modulus (left) and phase angle (right) of the nozzle reflection coefficient $\mathcal{R}$ for configurations D12-1 (top), D12-2 (middle) and D06-1 (bottom). Analytical $\mathcal{R}_a$ (black-line), $\mathcal{R}(\sigma \neq 0)$ (◯) and $\mathcal{R}(\sigma = 0)$ (×).*

results with experimental signals have been addressed successively in this work. They are:

1 Temperature measurement errors due to thermocouple finite time constant (Sec. 3.3).

2 Difference between the inlet Mach numbers when entropy wave is switched on and off (Sec. 4.1).

3 The velocity-entropy interaction due to large modulation level of the convective velocity (Sec. 4.2.2).

4 Impact of signal noise (Sec. 4.2.1 and 4.3.1)

The last two reasons are actually interdependent during the experiments in the TAFG system. Indeed, it is difficult generate high amplitude temperature fluctuations with low modulation level of the convective velocity. Besides, the entropy contribution in the reflected pressure wave P_u^- is small in the cases explored. This is shown in Fig. 4.13, where the relative level of indirect to direct noise contributions in the near field upstream of the nozzle η_u have been calculated with the analytical nozzle reflection coefficients $\mathcal{R}_a$ and $\mathcal{R}_s$ and the measurement of H_{sa} (Sec. 3.4). η_u remains always lower than 25% of the pressure signal for all the three optimized operation conditions. One should remind that the noise level for a SNR = 20 dB represents 10% of the meaningful signal. This makes the results with the diff-R method very sensitive to signal noises.

Nevertheless, the experimental methods to determine upstream acoustic and

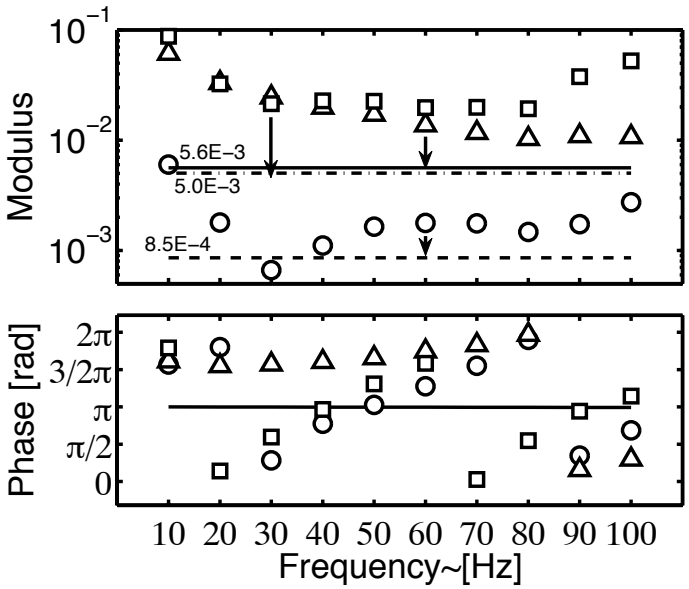

Figure 4.12: *Indirect reflection coefficient $\mathcal{R}_s$. D12-1: analytical (dashed-line), experimental (◯). D12-2: analytical (black-line), experimental (△). D06-1: analytical (dash-dotted-line), experimental (□).*

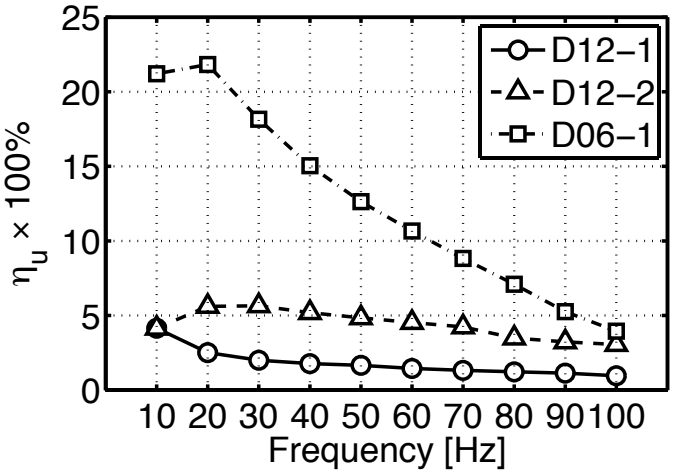

Figure 4.13: *Ratio of indirect to direct noise level upstream of the nozzle η_u for the three optimised operation conditions*

entropy waves (see Sec. 3.4) and the diff-R method have been validated. They are used in the second part of the thesis in a laboratory-scale burner under the Large Eddy Simulation (LES) framework.

Part II

Analysis of combustion noise in a laboratory-scale burner using Large Eddy Simulation

Chapter 5

LES of the CESAM-HP Burner

This chapter focus on the implementation of the Large Eddy Simulation of a laboratory-scale burner. A brief introduction to the LES method is given in the first place. Next the CESAM-HP burner is presented and followed by the definition of the computational domain and the corresponding mesh. The LES code AVBP and the numerical configurations are presented in the last section with some emphasis on the boundary conditions.

5.1 An introduction to Large Eddy Simulation

The theory of combustion noise given by Eq. (2) in Sec. was obtained from a rearrangement of Navier-Stokes equations for a reactive flow with N-species, which have been written based on the conservation of mass, species, momentum and total non-chemical energy ignoring external forces (Poinsot and Veynante 2005):

$$\frac{\partial \rho}{\partial t} + \frac{\partial \rho u_i}{\partial x_i} = 0 \tag{5.1}$$

$$\frac{\partial (\rho Y_k)}{\partial t} + \frac{\partial}{\partial x_i}\left[\rho (u_i + V_{k,i}) Y_k\right] = \dot{\omega}_k \tag{5.2}$$

$$\frac{\partial (\rho u_i)}{\partial t} + \frac{\partial (\rho u_i u_j)}{\partial x_j} = -\frac{\partial p}{\partial x_i} + \frac{\partial \tau_{ij}}{\partial x_j} \tag{5.3}$$

$$\rho \frac{DE}{Dt} = \dot{\omega}_T - \frac{\partial q_i}{\partial x_i} - \frac{\partial p u_i}{\partial x_i} + \frac{\partial (\tau_{ij} u_i)}{\partial x_j} + \dot{\mathcal{Q}} \tag{5.4}$$

These equations are written in Cartesian coordinate system with the Einstein convention, where ρ is the density, x_i and u_i are the i-th coordinate and velocity component. Eq. (5.2) is the mass conservation equation of species k for $k =$

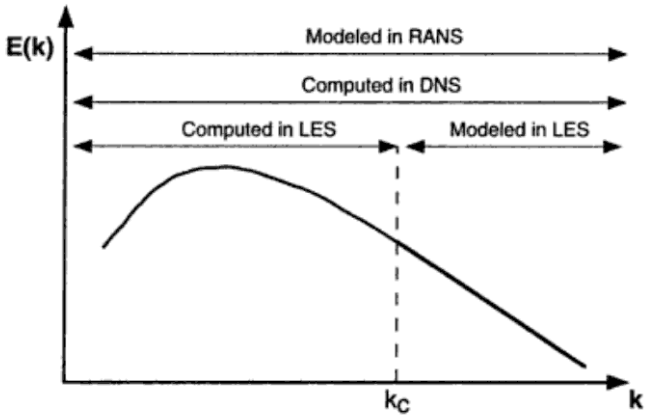

Figure 5.1: *Turbulent energy spectrum plot as a function of wave numbers. DNS, RANS and LES are summarised in terms of spectral frequency range. k_C is the cut-off wave number used in LES (log-log diagram) (Poinsot and Veynante 2005)*

.

1 to N, where Y_k is its mass fraction, $V_{k,i}$ is the i-th component of its diffusion velocity V_k and $\dot{\omega}_k$ its reaction rate. Summing up Eq. (5.2) established for all species leads to a necessary condition for total mass conservation, which is $\Sigma_{k=1}^{N} Y_k V_{k,i} = 0$. In the momentum conservation equation Eq. (5.3), p is the pressure, τ_{ij} is the viscous tensor (in Pascal) defined by:

$$\tau_{ij} = -\frac{2}{3}\mu\frac{\partial u_k}{\partial x_k}\delta_{ij} + \mu\left(\frac{\partial u_i}{\partial x_j} + \frac{\partial u_j}{\partial x_i}\right) \tag{5.5}$$

where μ is the dynamic viscosity and the kinematic viscosity $\nu = \mu/\rho$. $\delta_{i,j}$ is the Kronecker symbol: $\delta_{ij} = 1$ if $i = j$ otherwise 0. Viscous tensor and pressure are often combined into the total stress tensor σ_{ij} by $\sigma_{ij} = \tau_{ij} - p\delta_{ij}$. The total non-chemical energy E in Eq. (5.4) is the sum of sensitive energy e_s and the kinetic energy $\frac{1}{2}u_i u_i$, $\dot{\omega}_T$ is the heat release due to combustion, q_i is the energy flux including heat diffusion and diffusion of species with different enthalpies, $\dot{\mathcal{Q}}$ is an external heat source term other than combustion (due to for example an electric spark, a laser or a radiative flux).

In most applications combustion is turbulent and involves complex chemical process. While it is almost impossible to handle turbulent combustion with analytical techniques, Computational Fluid Dynamics (CFD) methods is a fast growing area (Poinsot and Veynante 2005). There are three commonly used CFD approaches, namely Direct numerical simulation (DNS), Raynolds Averaged Navier-Stokes (RANS) and Large Eddy Simulation (LES). Their characteristics are usually summarised in terms of energy spectrum in Fig. 5.1. DNS computes explicitly all spatial scales whereas in RANS only mean flow are resolved. LES is increasingly used as a trade-off between computational cost and

accuracy. The objective of LES is to resolve large structures in the flow field whereas small structures are modelled. In practice the spatial filter is simply the mesh, and the modelled scales are subgrid scales (SGS). The mass-weighted spatial filtering of a quantity Φ in the LES is defined by:

$$\overline{\rho}\widetilde{\Phi} = \int \rho\Phi(\mathbf{x}')F(\mathbf{x}-\mathbf{x}')d\mathbf{x}' \tag{5.6}$$

where F is the LES filter. After applying the LES filter, the filtered balance equations write (Poinsot and Veynante 2005):

$$\frac{\partial\overline{\rho}}{\partial t} + \frac{\partial(\overline{\rho}\widetilde{u_i})}{\partial x_i} = 0 \tag{5.7}$$

$$\frac{\partial(\overline{\rho}\widetilde{Y_k})}{\partial t} + \frac{\partial(\overline{\rho}\widetilde{u_i}\widetilde{Y_k})}{\partial x_i} = \frac{\partial}{\partial x_i}\left[\overline{V_{k,i}Y_k} - \overline{\rho}\widetilde{u_iY_k} - \widetilde{u_i}\widetilde{Y_k})\right] + \overline{\dot{\omega}_k} \tag{5.8}$$

$$\frac{\partial(\overline{\rho}\widetilde{u_i})}{\partial t} + \frac{\partial(\overline{\rho}\widetilde{u_i}\widetilde{u_j})}{\partial x_j} = -\frac{\partial\overline{p}}{\partial x_i} + \frac{\partial}{\partial x_i}\left[\overline{\tau}_{ij} - \overline{\rho}(\widetilde{u_iu_j} - \widetilde{u_i}\widetilde{u_j})\right] \tag{5.9}$$

$$\begin{aligned}\frac{\partial(\overline{\rho}\widetilde{E})}{\partial t} + \frac{\partial}{\partial x_i}(\overline{\rho}\widetilde{u_i}\widetilde{E}) = \overline{\dot{\omega}_T} - \frac{\partial\overline{q_i}}{\partial x_i} - \frac{\partial\overline{p}\widetilde{u_i}}{\partial x_i} + \frac{\partial}{\partial x_j}\left[\overline{(\tau_{ij}-\tau^t_{ij})}\widetilde{u_i}\right] \\ + \frac{\partial}{\partial x_i}\left[\overline{\rho}(\widetilde{u_iT} - \widetilde{u_i}\widetilde{T})\right]\end{aligned} \tag{5.10}$$

In these equations, the Reynolds stress $(\widetilde{u_iu_j} - \widetilde{u_i}\widetilde{u_j})$ is unresolved and requires SGS turbulence models such as Smagorinsky model, scale similarity model and Germano dynamic model (Poinsot and Veynante 2005). The other unresolved term concerning the species flux $(\widetilde{u_iY_k} - \widetilde{u_i}\widetilde{Y_k})$ can be usually estimated from modelled Reynolds stress.

By filtering the instantaneous balance equations, LES allows a dynamic representation of the large scale motions such as large vortex shedding and acoustic waves. The results are therefore close to the physical state in complex geometries. The present work uses LES to compute the reacting flow in a laboratory-scale burner running at a choked condition at the outlet of the combustion chamber. First the computational domain is presented.

5.2 Computational domain

5.2.1 The CESAM-HP burner

The CESAM-HP burner (Mazur et al. 2015) has been developed in the EM2C Laboratory for the purpose of studying direct and indirect combustion noise

in the RECORD (Research on Core Noise Reduction) project[1] in the Seventh Framework Programme FP7 under Grant Agreement No. ACP2-GA-2012-312444. It is operated with propane-air lean-premixed combustion and swirl-stabilised flame. A schematic view of the burner is illustrated in Fig. 5.2. In the upstream region there is an Impedance Control System (ICS), which consists of a perforated plate (see Fig. 5.3) backed by a cylindrical cavity with adjustable length by moving a piston. A small amount of air is injected through the piston. The ICS is intended to damp combustion instabilities. The efficiency of the system can be optimized by combining air injection through the piston and the cavity length (Tran et al. 2009a; Tran et al. 2009b; Scarpato et al. 2012). After a series of experimental explorations, the distance between the piston and the rear face of the perforated plate has been set to 500 mm in all the operation conditions. An air injection tube with an inner diameter of 4 mm is also installed in the ICS cavity. The discharge surface of the air jet coincides with the front face of the perforated plate. The original purpose of the jet is to prevent flame flashback. In the admission stage of the burner, air and propane are first premixed in the feeding lines. The mixture goes into a flow-tranquillising plenum before it is injected tangentially in order to create a swirling motion. The cylindrical injector has a diameter of 30 mm and a length of 134.5 mm. It is connected to the combustion chamber which has a square cross-section of 70×70 mm and a length of 140 mm. The combustion chamber walls allow the installation of quartz plates to give optical access. These walls are also cooled by individual water circulation systems. The combustion chamber is terminated by a convergent-divergent nozzle. The special shape of the nozzle has been designed by ONERA to favorise indirect combustion noise generation (Giauque et al. 2013). Three operating conditions have been explored and summarised in Table 5.1. Under these conditions, the nozzle is effectively choked. The global equivalence ratio of the propane-air mixture is equal to 0.85 in all the cases, so that the burner is running at a power of 45 kW.

Pressure sensors are installed on the chamber walls at four axial positions equally distanced by 35 mm (see Fig. 5.2). They record the total pressure signals in the chamber, from which the mean and fluctuating parts can be extracted. The Two-thermocouple sensor is located at position x_4 and can submerge in the burnt gas at variable positions in y direction. It is made of two R-type thermocouples of diameter 50 μm and 125 μm. The mean gas temperature given in Table 5.1 has been compensated using the two thermocouple signals measured at $x_4 = 122.5$ mm, $y = 20$ mm. Optical diagnostics such as Particle Image Velocimetry (PIV), OH^* chemiluminescence and Laser Interferometric Vibrometry (LIV) are also available to investigate the flow and flame characteristics in the combustion chamber. The experimental results are used as reference to validate the LES of the burner.

[1] Project coordinator: Friedrich Bake

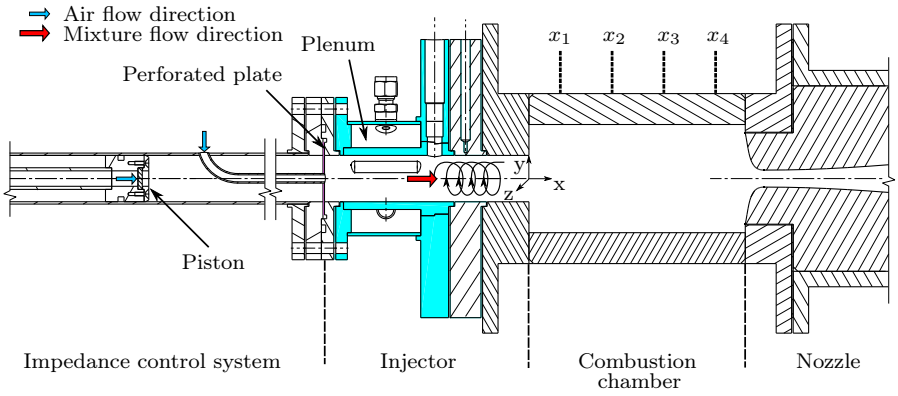

Figure 5.2: *Schematic view of the CESAM-HP burner*

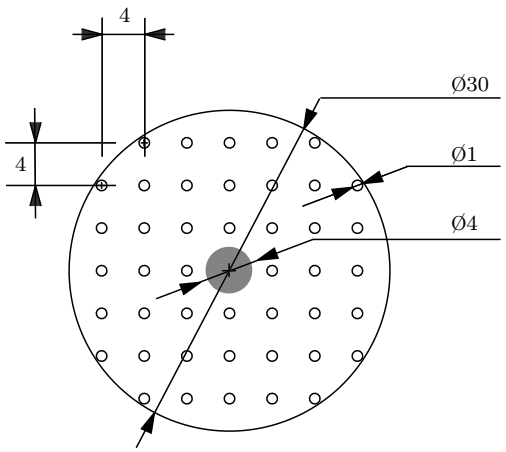

Figure 5.3: *The perforated plate used in ICS. The grey area corresponds to the discharge plane of the jet. Unit in mm.*

Table 5.1: *CESAM-HP reactive operating conditions, mean pressure and temperature measured at axial position x_4*

Name	Air [g/s]			Propane [g/s]	$\bar{p}$ [bar]	$\bar{T}$ [K]
	tangential	jet	piston			
op16-0-2-85	16	0	2	0.98	2.37	1890
op16-2-0-85	16	2	0	0.98	2.36	1900
op13-5-0-85*	13	5	0	0.98	1.80	1920

*Case measured with the eroded nozzle

5.2.2 Computational domain and the unstructured mesh

The computational domain of the reactive LES is illustrated in Fig. 5.4. A large part of the feeding lines are removed in the simulations and are replaced by inlet boundary conditions (see Sec. 5.3.4.1). Simulations with full nozzle geometry carried out by Lapeyre (2015) have produced large mean pressure differences from experimental data, showing that the flow in the nozzle was not resolved enough. Compromise between calculation cost and accuracy leads to the choice of simulating the convergent part and a short section of the divergent part of the nozzle. In the non-reactive LES, a hemispherical atmosphere of radius 1 m is connected to the nozzle outlet. This is a numerical choice to impose correctly the pressure on the nozzle outlet without dealing with the complex flows in the divergent part of the nozzle. The target pressure at the boundary of the atmosphere for the cold run is first calculated from the 1D isentropic nozzle theory based on the pressure inside the chamber measured experimentally. It is then slightly adjusted until the mean pressure in the chamber obtained from the LES converges to the experimental condition. In reactive runs the nozzle is choked, so that the flow domain upstream of the nozzle throat is not affected by the downstream conditions. Particularly the ICS has been removed in the non-reactive simulations, since it is rather the aerodynamics in the burner than the acoustic behaviour that is the main interest of the cold runs.

The above computational domain is now discretized with an unstructured mesh of 11 millions of tetrahedral cells and 2 million nodes. Some details of the unstructured mesh are illustrated in Fig. 5.5. The global grid size in the injector and the combustion chamber is equal to 1 mm, while the region downstream of the jet exhaust and the region with the flame are refined respectively to 0.4 mm and 0.6 mm.

During the RECORD project the design of the CESAM-HP burner has been modified in order to stabilise the flame. The previous design has two tangential air injection stages instead of one as in the final version of the burner (see Fig. 5.2, stage colored in cyan). It is also deprived of the air jet on the front face of the perforated plate. The compressible LES of the two-stage version of the burner has been achieved during the Ph.D of Lapeyre (2015), who has conducted both reactive and non-reactive simulations and given very pertinent insights on some phenomena observed in the experiments, namely the flame stabilisation, flashback and combustion instabilities. The simulation of the current version of the burner follows the same numerical setup that are summarised in the next section. Only some modifications of the unstructured mesh and boundary conditions were made in order to adapt to the new geometry and the operating conditions, as will be discussed in Sec. 5.3.4.1.

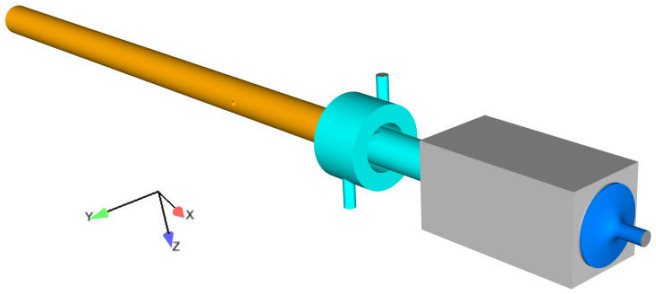

(a) Global view

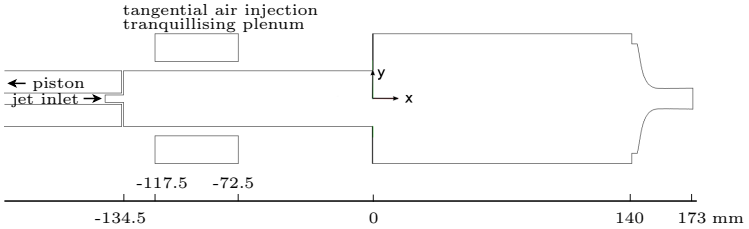

(b) Outline and key dimensions

Figure 5.4: *Computational domain for the reactive LES*

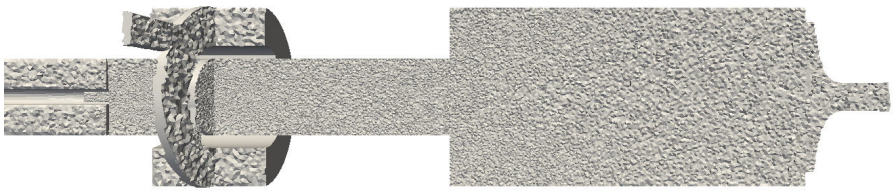

Figure 5.5: *View of the unstructured mesh of the computational domain*

5.3 The LES code: AVBP

The compressible Large eddy simulations of the CESAM-HP burner were conducted with the high-fidelity LES code AVBP (Schönfeld and Rudgyard 1999; Moureau et al. 2005; Cerfacs 2008) developed by CERFACS and IFP-EN. AVBP solves the three-dimensional compressible Navier-Stokes equations for turbulent reacting flows, using both the DNS and LES approaches on unstructured and hybrid meshes.

5.3.1 Subgrid scale model (SGS)

The filtered compressible Navier-Stokes equations exhibit subgrid scale (SGS) tensors and vectors describing the interaction between the non-resolved and resolved motions. The influence of the SGS on the resolved motion is taken into account in AVBP by a SGS model based on a turbulent kinetic viscosity ν_t (Cerfacs 2008). Such an approach assumes the effect of the SGS field on the resolved field to be purely dissipative. Various subgrid scale models are available in AVBP, and they only differ in the estimation of ν_t. The Smagorinsky model (Smagorinsky 1963) has the particularity of supplying the right amount of dissipation of kinetic energy in homogeneous isotropic turbulent flows, but local features are lost and only global quantities are maintained. The WALE (Wall Adapting Linear Eddy) model proposed by (Nicoud and Poinsot 1998) gives the correct scaling of turbulent viscosity when approaching walls and determining transition from laminar to turbulent flow. The Sigma model (Nicoud et al. 2011) presents the interesting properties to vanish in various laminar flow configurations for which no SGS activity is expected. It also shares with the WALE model the property to vanish with the proper asymptotic behaviour near solid boundaries. This model is highly recommended for performing 3D flows computations in complex configurations and academic cases as well. The Sigma model is retained in this work.

5.3.2 Combustion model

The chemical scheme for lean premixed propane-air has been reduced to a global one-step reaction including 5 species ($C_3H_8, O_2, N_2, CO_2, H_2O$) in the LES. At the equivalence ratio $\Phi = 0.85$ the laminar flame speed S_L and flame thickness were determined from a 1D DNS, which gave $S_L = 28.46$ cm/s and $\delta_L = 186$ μm. At this point, the flame is non-resolved on the mesh. The Thickened Flame (TF) Model is then implemented in AVBP. The basic idea of TF model is to consider flame thicker than the actual one while the flame speed is conserved. The artificially thickened flame front may then be resolved

in LES on the mesh without applying a SGS model. The reaction rate is expressed using an Arrhenius law as in DNS. However, the thickening of the flame reduces the flame surface and consequently the reaction rate. Interaction between the turbulence and chemistry may be modified and accordingly the interaction between flame and turbulence may be altered. An efficiency function has been derived in numerous works using DNS (for example Angelberger et al. (1998); Colin and Rudgyard (2000)) to correct this effect, which consists to apply a wrinkling factor on the diffusivity and the reaction rate, and then propagates the flame at a higher subgrid scale turbulent flame speed. In AVBP, there is also a dynamic version of the TF model which is recommended for partially premixed flame. The thickening operation is only applied in the reacting regions to preserve diffusion in non-reacting regions (Legier et al. 2000). The Dynamic Thickened Flame model is used in this work combined with the Charlette-Meneveau efficiency function (Charlette et al. 2002). The thickened flame is resolved by 3 mesh points, yielding a thickening factor of 10 since the unstructured mesh is refined to 0.6 mm in the flame zone.

5.3.3 Numerical method

The discretization of the governing equations in AVBP relies on the Cell Vertex (CV) Finite-Volume (FV) method (Cerfacs 2008). The CV method consists in applying conservation relations to the grid cells, while solution is stored at the grid nodes. For time marching method, AVBP only uses a multi-stage low-storage Runge-Kutta (RK) scheme. The diffusive terms are discretized using the Galerkin Finite Element 2Δ method (Colin et al. 2003), which offers strong dissipations at the highest frequencies and therefore well suited for LES. To discretize the convective fluxes, different numerical schemes are available in AVBP. The second-order in space, third-order in time Lax-Wendroff (LW) numerical scheme (Ni 1982) has been used first in this work to start computations. Then it is replaced by the third-order in time and space Taylor-Galerkin Finite Element scheme TTGC (Colin and Rudgyard 2000) in order to propagate vortices and acoustic waves accurately.

5.3.4 Boundary conditions

5.3.4.1 General inlet, outlet and wall boundary conditions

For inlet and outlet boundary conditions (BC), Navier-Stokes Characteristic Boundary Condition (NSCBC) (Poinsot and Lele 1992; Poinsot and Veynante 2005) have been implemented in AVBP. The key concept of NSCBC is the following: flow variables are decomposed into ingoing and outgoing characteristic

waves, waves that are leaving the domain are well-computed by the numerical scheme and must be left unchanged, while waves entering the domain cannot be computed by the numerical scheme and must therefore be replaced by user-defined values. The imposed values must reflect the physics of the BC (Cerfacs 2008). In this work, the mass flow rate at the inlets are imposed whereas the pressure is imposed on the outlet. The computations converge to the imposed values with an adjustable relaxation coefficient. The relaxation coefficient is chosen based on the principle of imposing non-reflecting conditions for acoustic waves, therefore has been set to small values both at the inlets and the outlet of the computational domain.

Two kind of wall-type boundary conditions are implemented in AVBP. No-slip wall condition has been used on most of solid boundaries, on which the velocity is simply imposed to zero. The grid size is in general small enough ($y^+ < 50$) so that no-slip boundary conditions can be applied safely. However, exception has been made on the jet injection tube wall, where a logarithmic law has been applied in order to give a more realistic turbulent velocity profile at the jet discharge. The corresponding mesh size in the jet tube, which is 0.4 mm, have been determined by a 2D test presented in Appendix A.

Special boundary treatments, such as the perforated plate and heat loss wall conditions have also been employed in the LES in order to mimic the experimental conditions. These BCs are carefully controlled during the computations and are verified *a posteriori* in the following.

5.3.4.2 Homogeneous coupled boundary condition for the perforated plate

The Impedance Control System has been found very efficient in stabilising combustion process during the experimental explorations of the CESAM-HP burner. The contributing mechanism behind this is well recognised as the attenuation of acoustic energy by vorticity production at the rims of perforated holes (Howe 1979; Howe 1997). The acoustic damping can be further enhanced by the presence of a closed resonance cavity behind the perforated plate (Hughes and Dowling 1990; Bellucci et al. 2004; Tran et al. 2009b). Therefore it is important to well capture the acoustic behavior of the ICS in the LES computations.

The flow through the holes on the perforated plate is however too expensive to compute. Instead, a coupled boundary condition is applied in AVBP to produce numerically the acoustic behaviour of the perforated plate in the ICS. The dedicated numerical method, developed by Mendez and Eldredge (2009), couples the flow quantities on both side of the perforated plate by a homogeneous

condition derived from the perturbation form of Bernoulli's equation written as:

$$\Delta P = \rho l' \frac{\partial U_j}{\partial t} + \frac{(\rho U_j)^2}{2\rho C_D^2}; \quad l' = \frac{\pi a}{2} + h \tag{5.11}$$

where a is the hole radius, h is the thickness of the perforated plate, U_j is the bulk velocity of the jet formed through the holes and C_D is the discharge coefficient of the hole. This approach has been used in Luong et al. (2005) to unify the non-linear model for the acoustic absorption of a perforated plate without a mean flow given in Cummings and Eversman (1983); Cummings (1986) and the linear model for the same problem but with bias flow given in Howe (1979). The numerical approach also takes account of the effect of the finite thickness of the plate using the term l' as proposed by Jing and Sun (2000). The performance of the coupled boundary condition has been evaluated *a posteriori* by comparing the reflection coefficient R_{ICS} and the absorption coefficient $A_{\text{ICS}} = 1 - |R_{\text{ICS}}|^2$ (Hughes and Dowling 1990) of the ICS with existing models.

To compute the reflection coefficient numerically, pressure and axial velocity signals are recorded during 100 ms at 65 536 Hz on one probe located on the front face of the perforated plate. Progressive and regressive characteristic waves are then given by plane wave decomposition:

$$P^{\pm} = \frac{1}{2}\left(\frac{p'}{\gamma p} \pm \frac{u'}{c}\right) \tag{5.12}$$

The ratio P^-/P^+ gives directly the reflection coefficient on the front face of the ICS system in LES.

For the perforated plate with a bias flow, corresponding to the case op16-0-2-85, analytical solution of the reflection coefficient can be derived based on the Howe's model (Howe 1979). Consider a perforated plate of thickness h, with aperture radius a and interspace d, backed by a cavity of length L, and traversed by bias flow at bulk velocity U, the modified Rayleigh conductivity including plate thickness given by Jing and Sun (2000) writes:

$$K_R = 2a\left(\frac{1}{\gamma - i\delta} + \frac{2}{\pi}\cdot\frac{h}{a}\right)^{-1} \tag{5.13}$$

$$\text{with} \quad \gamma - i\delta = 1 + \frac{1}{St}\cdot\frac{\frac{\pi}{2}I_1(St)e^{-St} - iK_1(St)\sinh(St)}{\frac{\pi}{2}I_1(St)e^{-St} + iK_1(St)\cosh(St)}$$

In this expression $St = 2af/U_j$ is the Strouhal number based on the bulk velocity U_j of the jet formed through the aperture, and I_1 and K_1 are modified Bessel functions of first and second kind. The porosity of the perforated plate $\sigma_{poro} = \pi a^2/d^2$ is small $\sigma_{poro} \ll 1$ so that the flow interaction between holes can

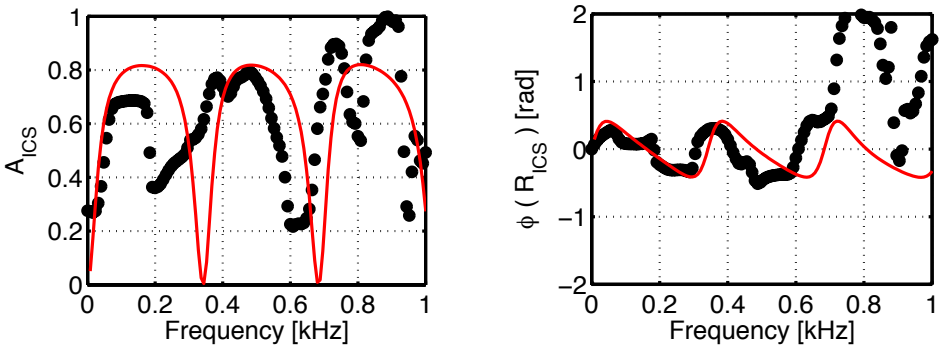

(a) Absorption coefficient (b) Phase angle of reflection coefficient

Figure 5.6: *Acoustic properties of the perforated plate with a back cavity from LES (symbols) and analytical modified Howe's model (line). Case op16-0-2-85*

be neglected (Melling 1973). Based on this assumption, the complex reflection coefficient at the front face of the perforated plate-back cavity system given by Hughes and Dowling (1990) writes:

$$R_{\mathrm{ICS}} = \frac{(ikd^2/K_R) + 1 - (i/tan(kL))}{(ikd^2/K_R) - 1 - (i/tan(kL))} \tag{5.14}$$

where $k = \omega/c$ is the wave number.

The coefficients obtained from analytical and numerical approaches are given in Fig. 5.6 for the operation condition op16-0-2-85. The acoustic damping by the ICS calculated in LES is in general coherent with the modified Howe's model below 600 Hz, showing that as high as 80% of acoustic energy are dissipated by the vortex shedding in the vicinity of the perforated plate. A frequency shift between the analytical and numerical reflection coefficients is also observed. This is suspected related to the onset of nonlinear acoustic dissipation when the perforated plate is submitted to high sound pressure level of the incident wave. One should note that Howe's model has been established for linear acoustic dissipations by vortex shedding. Under the explored experimental condition, the sound pressure level (SPL) in the CESAM-HP burner reached more than 140 dB in the frequency range below 400 Hz. This kind of condition has been extensively examined by Ingard and Ising (1967) for a single aperture with and without bias flow, who have shown that acoustic dissipation by the aperture is dependent on the SPL and total sound absorption can occur at high SPL values of the incident acoustic wave.

This test have shown that the coupled boundary condition behaves well as expected by the frequency-domain model it aims to build in time-domain LES computations. However the obtained results should be used with caution due

to the lack of experiments. Finally for the two operation conditions without the bias flow, op16-2-0-85 and op13-5-0-85, the effect of nonlinear interaction between the vortex shedding and the acoustic waves is suspected to be more important than the case with a bias flow (Tran 2009).

5.3.4.3 Heat loss on the combustion chamber walls

For reactive LES, heat losses on the chamber walls equipped with the water-cooling system have been taken into account by using an uniform heat resistance on these walls. The quartz wall in the combustion chamber is treated as adiabatic. Comparison with the experimental conditions are summarised in Table 5.2. The total heat extracted from the wall by water-cooling during the experiments reaches more than 20% of the combustor power for all operation conditions. This would largely reduce the mean pressure in the chamber. The comparison between LES computations with adiabatic wall and heat loss wall have shown a 0.2 bar drop in the mean pressure.

Table 5.2: *Experimental and numerical heat losses on the chamber walls for the operation condition op16-0-2-85*

Case	bottom wall	top wall	instrument carrier wall
Exp. op16-0-2-85	4.24 kW	2.83 kW	2.42 kW
LES. Mean	3.66 kW	2.85 kW	2.15 kW
LES. RMS	0.47 kW	0.30 kW	0.25 kW

Chapter 6

Numerical characterisation of the CESAM-HP burner

This chapter presents the LES of the CESAM-HP burner by comparing with experimental results from three aspects: aerodynamic, thermoacoustic and temperature field near the nozzle. The main objective of this cross check is to obtain high-fidelity numerical signals of pressure and temperature fluctuations inside the burner that can be used to measure nozzle transfer functions with the diff-R method. First the velocity field from both reactive and non-reactive LES are compared with the Particle Image Velocimetry (PIV) results. Second the acoustic behaviour of the the burner is investigated from the power spectra of numerical and experimental pressure signals. Finally temperature fields on transverse planes near the inlet of the nozzle have been extracted from the LES, the mean and the line-of-sight integration of which have also shown good agreement with experimental investigations.

6.1 Overview of LES simulations

LES simulations of the three reactive cases in Table. 5.1 are presented in this section by first looking at temporal evolutions of flow quantities. Fig. 6.1 gives the pressure, axial velocity and temperature signals recorded by a probe located at the end of the chamber at $(x, y, z) = (140, 0, 0)$ mm. The mean pressure and temperature in all cases were closed to experimental measurements given in Table. 5.1. The mean axial velocity reached high values at the entrance of the nozzle. For the three cases, pressure oscillations at a relatively high amplitude occurred at a proper frequency. The combustion instability will be analysed later in Sec. 6.3.

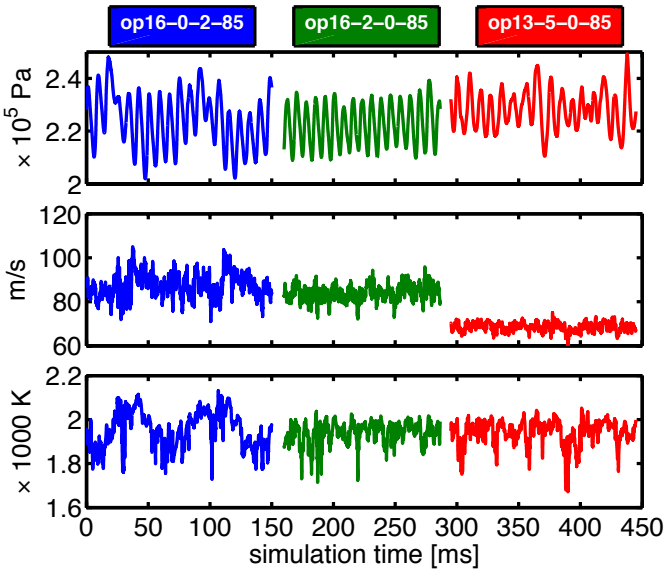

Figure 6.1: *Overview of reactive LES simulations. Pressure (top), axial velocity (middle) and temperature (bottom) signals are recorded by a probe at* $(x, y, z) = (140, 0, 0)$ *mm from reactive LES simulations.*

Next LES solutions are averaged during 100 ms after converged, corresponding to about two flow-through time in the burner calculated based on the bulk velocity in cold conditions. Fig. 6.2 illustrates the time-averaged temperature fields in the central plan $z = 0$ for all operating points. The flame was stabilised inside the injector in the two cases with 16 g/s tangential air injection. It will be shown in Sec. 6.2.3 that the flame location in the injector is determined by the swirl number. For all reactive cases, a typical M-shaped flame was formed. The temperature gradient in the injector was smaller than in the region stabilised on the backward facing step. This is an averaging effect of the flame front that is moving unsteadily towards up and downstream of the injector, as will be discussed in Sec. 6.4.1.

Finally it is noted that signals from the case op16-0-2-85 in Fig. 6.1 were all modulated by a very low frequency content. The low frequency (around 15 Hz) signal became the dominant oscillatory mode after 200 ms, and the entire flame entered periodically in the injector. The LES simulations when the whole flame is located in the injector require a proper treatment of flame-wall interaction and also further refinement of the mesh grid, which are however not performed in the extent of the thesis. The simulations of the op16-0-2-85 case after 200 ms are not presented hereafter.

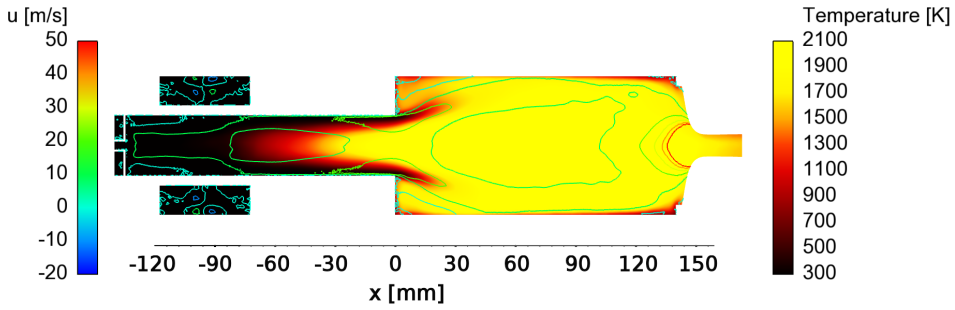

(a) op16-0-2-85

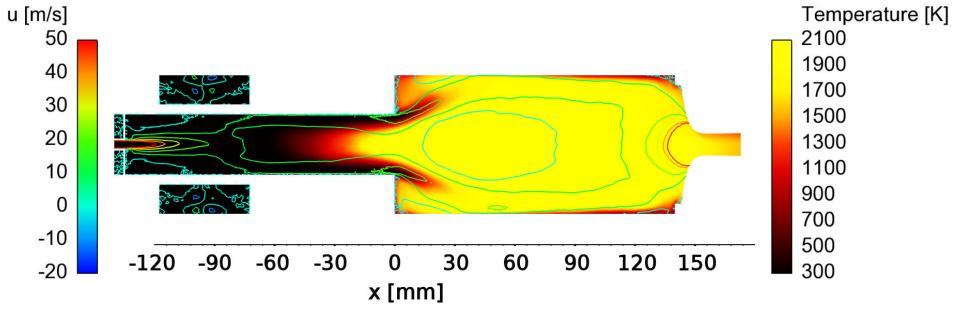

(b) op16-2-0-85

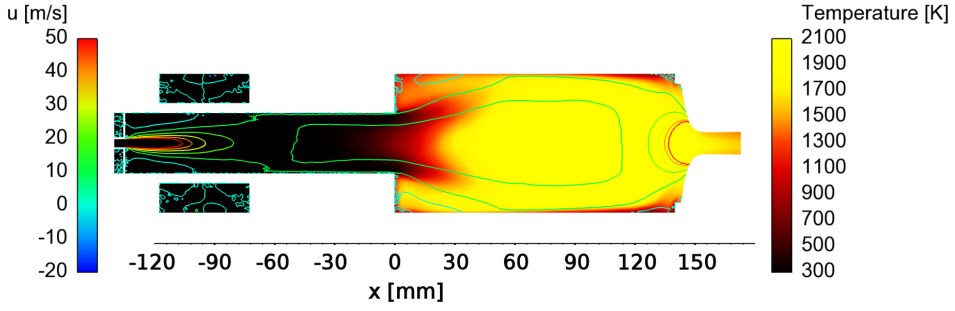

(c) op13-5-0-85

Figure 6.2: *Time-averaged LES temperature field superposed with axial velocity for three operation conditions.*

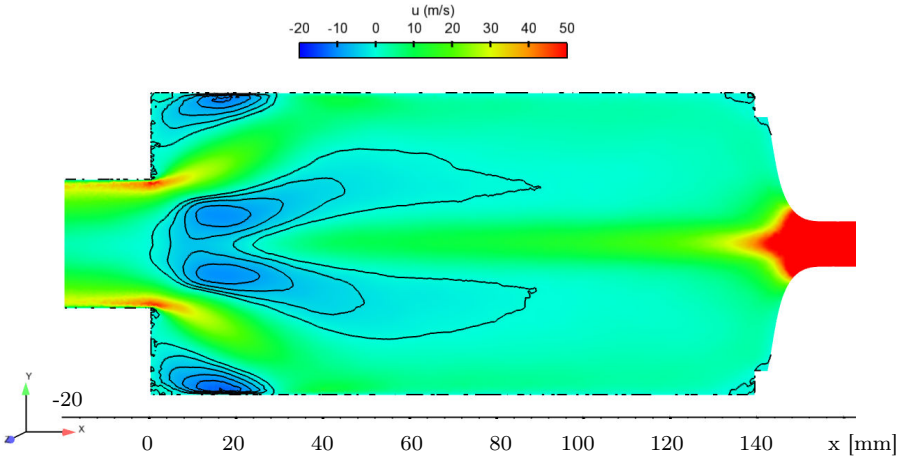

Figure 6.3: *Axial velocity field from time-averaged non reactive simulation of the case op16-0-2-85 in the plane $Z = 0$. Black lines indicates negative axial velocity $u < 0$.*

6.2 Flow characterisation

In this section, time-averaged and root-mean-square (RMS) velocity profiles in the central plane ($z = 0$) given by LES simulations are compared with Particle Image Velocimetry (PIV) measurements at different axial positions. 700 particle images were taken every 0.1 s to give the mean and RMS velocity fields in cold conditions, while 13 000 images from the high-speed PIV (100 000 Hz) technique developed in the EM2C laboratory were used in reactive conditions.

6.2.1 Non reacting flow velocity fields

The CESAM-HP burner features lean-premixed swirl-stabilised combustion. The effect of swirl on the flow motion in the burner has been examined first by a non reactive simulation of the case op16-0-2-85 in Table. 5.1 with 16 g/s tangential air injection and 2 g/s axial air injected through the perforated plated. The axial velocity field of the time-averaged simulation in Fig. 6.3 shows clearly the internal recirculation zone (IRZ) in the downstream region of the dump plane ($x = 0$). Outer recirculation zones (ORZ) are also formed due to the sudden enlargement right downstream of the dump plane.

Velocity profiles in the central plane $z = 0$ along the y-direction at various axial positions are extracted from the simulations, the time-averaged and RMS value of the velocity components in x and y directions, u and v respectively, are compared with the PIV measurements in Fig. 6.4. The mean velocity components were in good agreement with the experimental results. LES simulations also calculated correctly the size of the IRZ. The fluctuating velocities in these

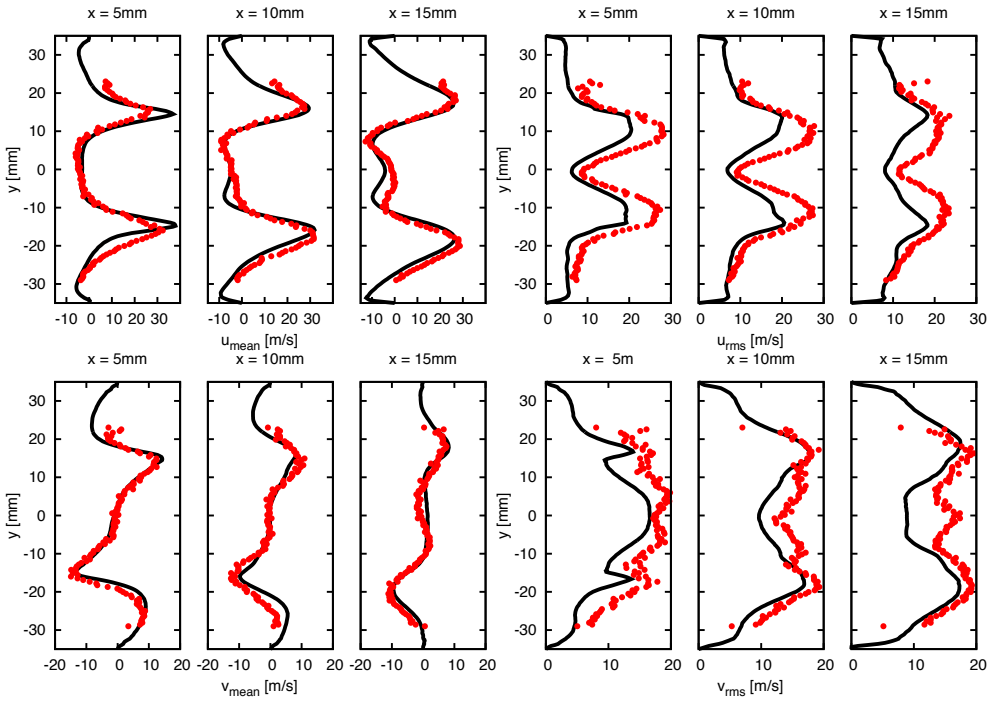

Figure 6.4: *Mean and RMS velocity profiles for the non reactive case op16-0-2-85. LES (line) and PIV (symbols).*

regions were however underestimated in LES. Flow in the recirculation region are often associated with high shear rates and strong turbulence intensity due to vortex breakdown (Huang and Yang 2009), which are difficult to handle by LES as well as experiments.

6.2.2 Reacting flow velocity fields

The velocity fields from reactive LES simulations are now compared with PIV measurements. Mean and fluctuating velocity components in x and y direction are extracted at various positions for the case op13-5-0-85 in Fig. 6.5. LES simulations yielded smaller internal recirculation zone and lower mean velocities compared to PIV measurements, while the fluctuation velocity components are close to experiments. In particular, the mean velocity component v almost vanished in the simulation, indicating a smaller centrifugal force than in experiments.

Fig. 6.6 gives the velocity components from LES and PIV for the case op16-2-0-85. Large difference in the RMS of axial velocity, especially in the internal recirculation zone, was observed between LES and PIV. It was the same for

the op16-0-2-85 case. Indeed, the simulations of the two cases with 16 g/s tangential air injection also present a periodical displacement of reaction zone in the injector that give rise to large axial velocity fluctuations near burner axis as will be discussed in Sec. 6.4.1.

Finally the discrepancy between LES and PIV measurements may also result from the erosion of the nozzle after series of firing. However no simulation with the enlarged nozzle are carried out yet due to the uncertainty in the geometrical description of the eroded nozzle.

6.2.3 Swirl number in reactive LES simulations

The mean temperature fields in Fig. 6.2 showed well that the flame was stabilised in the injection for the two cases with 16 g/s tangential injection. This is relevant to the strong swirl motion in the first two cases. To illustrate this, the swirl number of the flow in the injector has been calculated for the three reactive operating conditions using the time-averaged LES field. The swirl number is by definition the ratio of tangential moment to the axial moment. This work uses the swirl number given by Sheen et al. (1996) shown in Eq. (6.1).

$$S_w = \frac{\int_0^R U_{ax} U_{az} r^2 dr}{R \int_0^R U_{ax}^2 r dr} \tag{6.1}$$

where U_{ax} is the axial velocity, U_{az} is the azimuthal velocity and R is the outer radius of swirl annulus. Since the injector in the CESAM-HP burner features a constant cylindrical section, $R = 15$ mm, i.e. the inner radius of the injector. A schematic view for swirl number calculation is given in Fig. 6.7.

The swirl number as a function of the axial coordinate x for the three reactive cases are summarised in Fig. 6.8. At the upstream of the injector, the jet controls the swirl number as it augments the axial flow momentum. Comparing the two cases with 16 g/s tangential injection, they have equal swirl number at $x = -80$ mm. However, due to larger extent of the flame in the injector, the swirl number in the first case (Fig. 6.2(a)) drops earlier than the second case (Fig. 6.2(b)). At $x > -60$ mm, the swirl number in the two cases with 16 g/s tangential injection both exhibit a quasi-linear decrease along the axial direction, while it is almost constant in the case with 13 g/s tangential injection. The different swirl number decrease rates indicate the impact of the flame on the surrounding swirling flow. As the flame produces density and pressure gradient in the flow, it changes the flow vorticity and therefore the swirl number.

It is noted that the swirl number in the two most flashed back cases both reaches values higher than 1. Swirl-stabilised burners use the internal recirculation zone generated by vortex breakdown to stabilize the flame (Syred and Beér 1974;

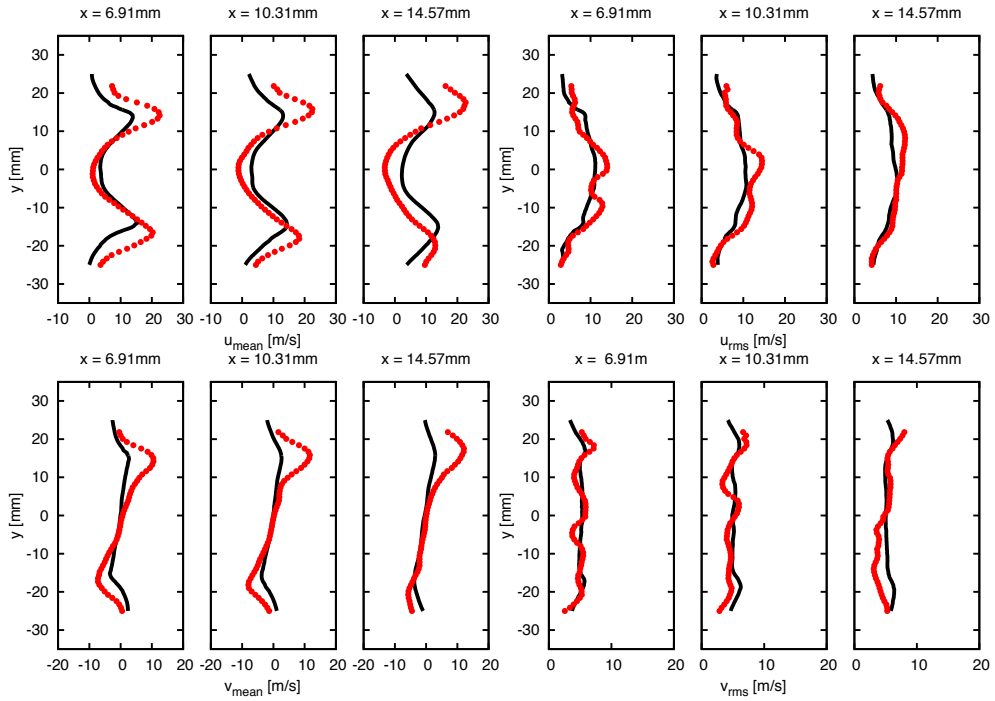

Figure 6.5: *Mean and RMS velocity profiles for the reactive case op13-5-0-85. LES (line) and PIV (symbols).*

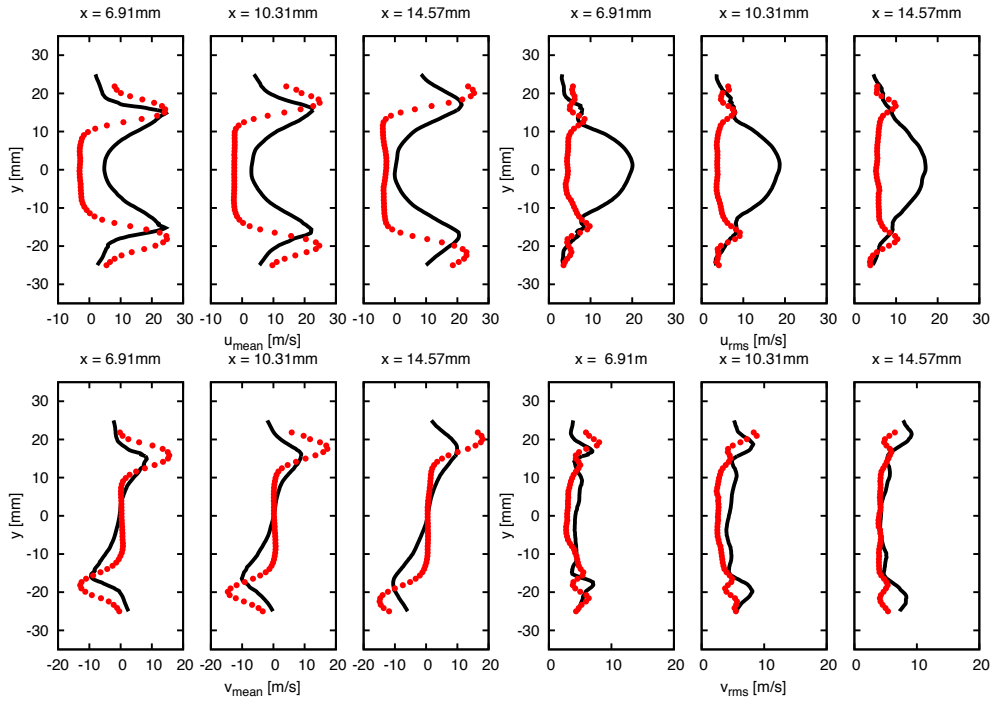

Figure 6.6: *Mean and RMS velocity profiles for the reactive case op16-2-0-85. LES (line) and PIV (symbols).*

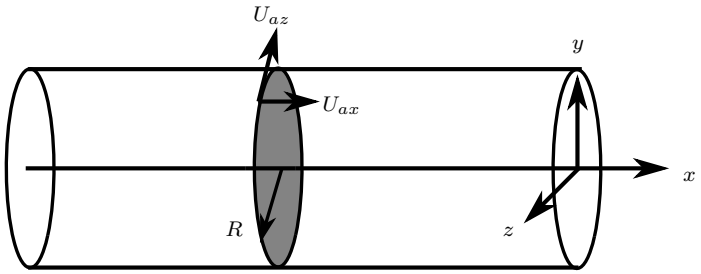

Figure 6.7: *Schematic view of the calculation of swirl number in the injector*

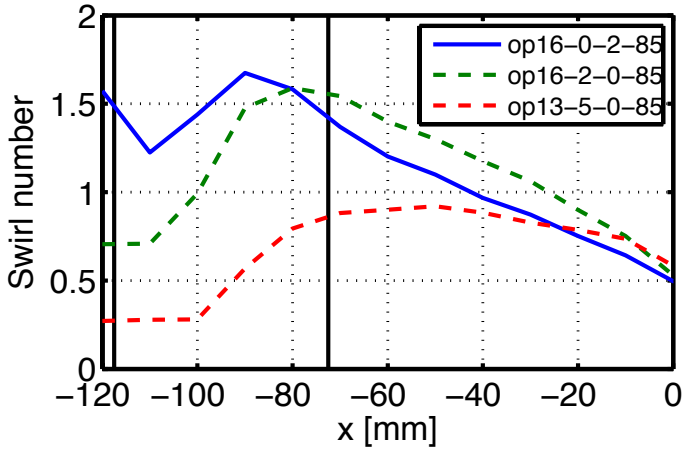

Figure 6.8: *Swirl number along the center axis of the injector. The tangential injection extends from $x = -117.5$ mm to $x = -72.5$ mm.*

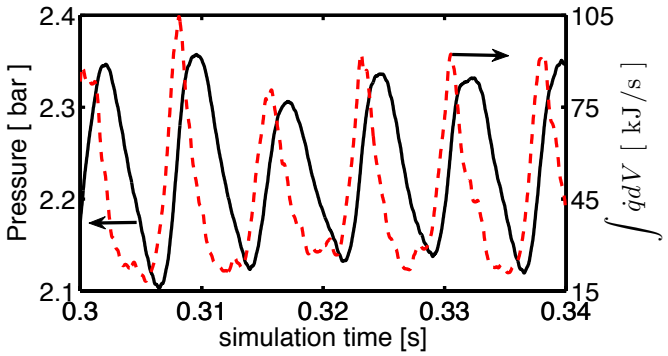

Figure 6.9: *Evolution of pressure and volume-integrated heat release rate from the LES of case op16-2-0-85*

Lucca-Negro and O'Doherty 2001). When the swirl number exceeds certain limit, a small and lengthy cylindrical recirculation zones can be generated in a tubular swirling flow without a centerbody as flame holder, and occasionally causes the flame to move upstream and result in flashback (Kröner et al. 2003; Fritz et al. 2004). Sec. 6.4.1 will show that such coherent structures occurred periodically in the injector due to acoustic perturbations.

6.3 Thermoacoustic characterisation

The thermoacoustic behavior in the CESAM-HP burner is studied in this section by first examining the pressure and heat release rate fluctuations.

Fig 6.9 gives the temporal evolution of pressure and heat-release rate from the LES of op16-2-0-85. The pressure signal is recorded by a probe located at $(x, y, z) = (0, 0, 0)$ and the unsteady heat release rate is integrated over the volume of the computational domain. In the presented case, pressure and heat release rate are oscillating at the same frequency around a mean pressure (2.2 bar) and mean heat release rate (44.9 kJ/s), which correspond well respectively to the measured mean pressure of this case (2.3 bar in Table. 5.1) and the heat of combustion (45 kW) of 0.98 g/s propane. Similar results for the mean pressure and volume-integrated heat release rate are obtained from the simulations of all the three reactive cases.

As self-sustained combustion instabilities are also observed in experiments, efforts have been made on identifying the instability modes. To do so, the sound pressure level (SPL) measured by the pressure sensor mounted on the chamber wall at position $x_4 = 122.5$ mm is calculated from experiments and simulations for all the three cases. The experimental signals are recorded during 10 second

at 16 384 Hz, and the numerical signals are sampled at 65 536 Hz during 125 ms, 100 ms and 250 ms for cases op16-0-2-85, op16-2-0-85 and op13-5-0-85 respectively. Welch method is used for spectral analysis and the frequency resolution is kept at 8 Hz for both numerical and experimental analysis.

The SPL for the three cases are summarised in Fig. 6.10. The peak frequencies and the corresponding sound pressure level from LES simulations agree well with the pressure sensor measurements. The differences between LES and experiment are most evident for very low frequencies below 50 Hz. It maybe due to the fact that pressure fields from LES contain both acoustic and hydrodynamic contributions, while in the experiments pressure sensors are mounted on the chamber wall and protected from flow turbulence. Hydrodynamic pressure is usually located at low frequencies, however, longer simulation time is necessary for LES to be representative in this range.

The two cases with 16 g/s tangential injection have very similar spectral signatures, with several distinct peaks at frequencies below 1 000 Hz and the highest SPL located between 120-128 Hz. There is also a certain feature around 3 000 Hz in simulations of the two cases. In fact as indicated in Fig. 6.11 by the coherence factor, the pressure sensors in the combustion chamber are highly correlated around 3 000 Hz, which corresponds to the longitudinal half-wave mode in the combustion chamber (2 948 Hz). The op13-5-0-85 case presents less distinct harmonics below 1 000 Hz compared to the first two cases, with a similar main peak at 120 Hz, but two symmetrical side peaks at 64 Hz and 176 Hz.

The two side peaks in the op13-5-0-85 case is relevant to the oscillatory rotation of the jet about an axis other than its own centerline, or jet precession. The 2D LES test case presented in Annexe B have already shown the flapping motion of the jet in the injector. A snapshot of this phenomenon is given in Fig. 6.12. Many works for example Hill et al. (1995); Nathan et al. (1998); Mi and Nathan (2004) have revealed the occurrence of self-exited jet precession when it emerges to a large quiescent cylindrical chamber. The jet-precession in these studies were described by the precession Strouhal number St_p, a dimensionless frequency defined by $St_p = f_p D/U_j$ with f_p, D, U_j corresponding to the precession frequency, jet orifice diameter and jet velocity respectively. An empirical description based on extensive experimental investigations of jet precession was given in Lee et al. (2007), which concluded that the jet precession is most sensitive to the expansion ratio, defined as the ratio of the chamber diameter D_c to the jet orifice diameter D_j, and the precession Strouhal number follows the empirical law $St_p = 7.6 \times 10^{-3}(D_c/D_j - 1)^{-1}$ for expansion ratio D_c/D_j of between 4.3 and 9.1. A rough estimation of the precession frequency in the op13-5-0-85 case based on the empirical Strouhal number leads to $f_p = 67$ Hz. This frequency is already close to the one predicted by LES simulations and in

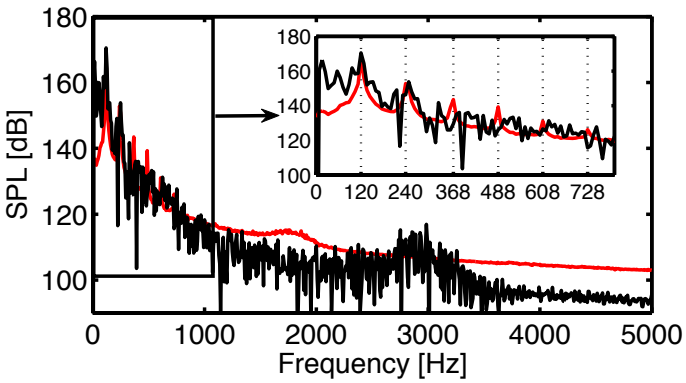

(a) SPL op16-0-2-85

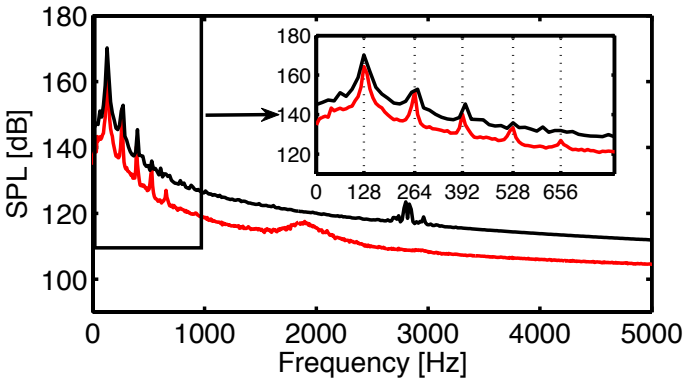

(b) SPL op16-2-0-85

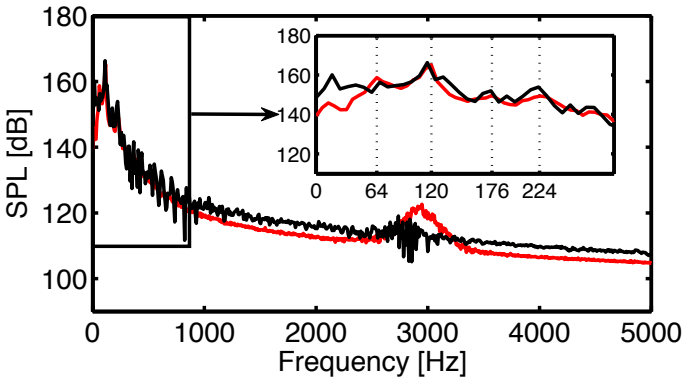

(c) SPL op13-5-0-85

Figure 6.10: *Sound pressure level measured at $x_4 = 122.5$ mm for the three operation conditions. LES (black) and Experiments (red).*

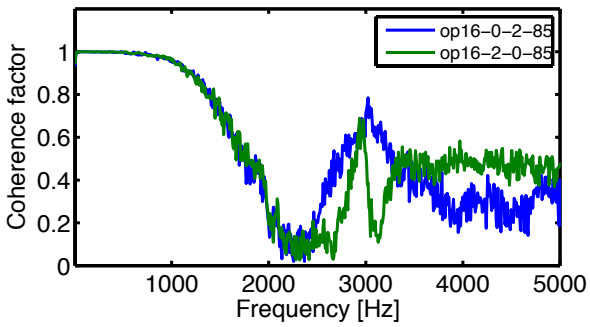

Figure 6.11: *Experimental signal coherence factor of two wall pressure sensors in the combustion chamber located at position x_2 and x_4*

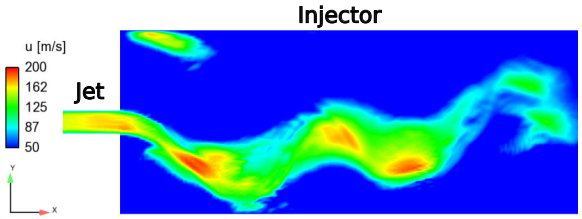

Figure 6.12: *A snapshot of axial velocity from the 2D LES test of the jet in the case op13-5-0-85 showing the flapping movement of the jet.*

the present work jet precession is also likely to convolve with the swirling flow.

The fundamental modes of combustion instability observed in all cases are very much lower than the longitudinal modes of the injector and combustion chamber. From a linear acoustic analysis of the burner presented in Appendix C, it is found that the first analytical eigenmode of the CESAM-HP burner is close to 92 Hz and is determined only when the acoustic impedances in the feeding lines are considered. In that analysis, the acoustic boundary condition of the feeding lines has been measured with the flame as the acoustic source. However, it was found in recent experiments that changing the length of the feeding lines does not change the instability mode. It is thus suspected that the missing element in the analysis: the tangential injection unit may be the cause of such contradiction. The tangential injection controls the swirling flow and the flame stabilisation. It is shown in the next section that the interactions between the flame and the swirling flow is substantial for the characterisation of the occurring combustion instability.

6.4 Numerical analysis of the self-sustained combustion instability

This section analyses the self-sustained combustion instability with raw and post-processed LES simulation of the case op16-2-0-85 (see Table 5.1). A qualitative description of the instability mechanism is given first from a sequence of LES snapshots, showing the occurrence of internal recirculation zone in the injector and the intermittent flash back due to acoustic perturbations. This illustrates the coupling between acoustic and velocity fluctuations in the burner, which is examined next by post-processing LES fields with Dynamic Mode Decomposition (DMD).

6.4.1 Intermittent flash back in the injector

Fig. 6.14 gives eight snapshots of burner central plane ($z = 0$) of LES simulations for the case op16-2-0-86. The snapshots have been taken with a 1 ms time interval and in total show about one cycle of the self-sustained instability. The number of snapshots are aslso annotated on the time evolutions of pressure and volume-integrated heat release rate. The position of the reaction zone evolves periodically in the injector. The flame tip moves toward upstream of the injector as the pressure increases and *vice versa*. A maximum depth is reached in snapshot 5. At this point the bulk flow in the injector is almost reversed and the flame surface is most stretched, yielding the largest heat release rate. Part

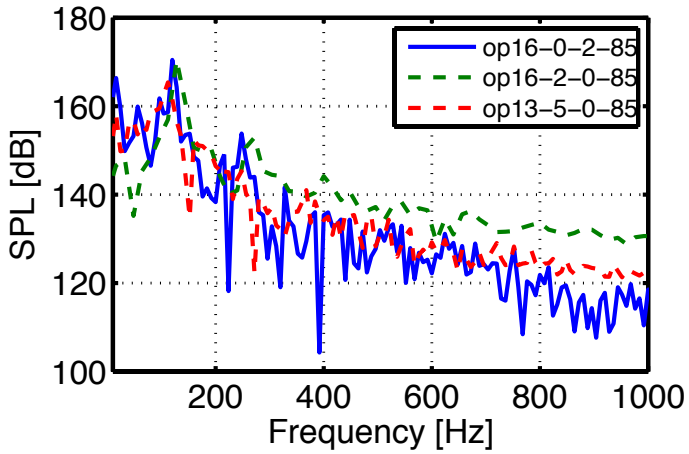

Figure 6.13: *Sound pressure level from the LES simulations.*

of the mixture pass through the perforated plate and the momentum of tangential injection should also be low at this moment. Apparently, the air jet at the head-end of the injector stops the flame from moving farther towards upstream. This could be the combined effect from the increase of axial momentum and dilution of the mixture by the jet.

A comprehensive study of fully and intermittent flash back in the two-stage version the same burner was given by Lapeyre et al. (2015) based on LES simulations. Accordingly, the intermittent flash back, such as illustrated in Fig. 6.14 was suspected to be induced by acoustic waves. By the LES simulations of the burner submitted to pressure oscillations at the chamber end, Lapeyre et al. (2015) have shown that fully flash back was triggered when the amplitude of pressure fluctuations reaches 20 kPa while at 10 kPa only intermittent flash back occurred. 10 kPa is approximately 170 dB in SPL, which is very close to those given by the LES simulations of the one-stage version of the burner in Fig. 6.13.

Acoustic perturbations produce acoustic velocity fluctuations. In the present case the amplitude of the acoustic velocity at the probe on the dump plane is 36 m/s while the bulk flow velocity 71 m/s. The high relative strength of the acoustic velocity gives rise to the occurrence of internal recirculation zone in the injector, which then moves the reaction zone to the upstream of the injector. This increases the flame surface and consequently the total heat release rate. Interestingly the heat release rate fluctuations is delayed by a quarter of oscillation period ($\pi/2$) compared to the pressure signal (Fig. 6.9), which corresponds to the phase shift between acoustic velocity and pressure. These interactions are then self-amplified due to the feedback from the nozzle and finally lead to a limit cycle such as observed in the simulations.

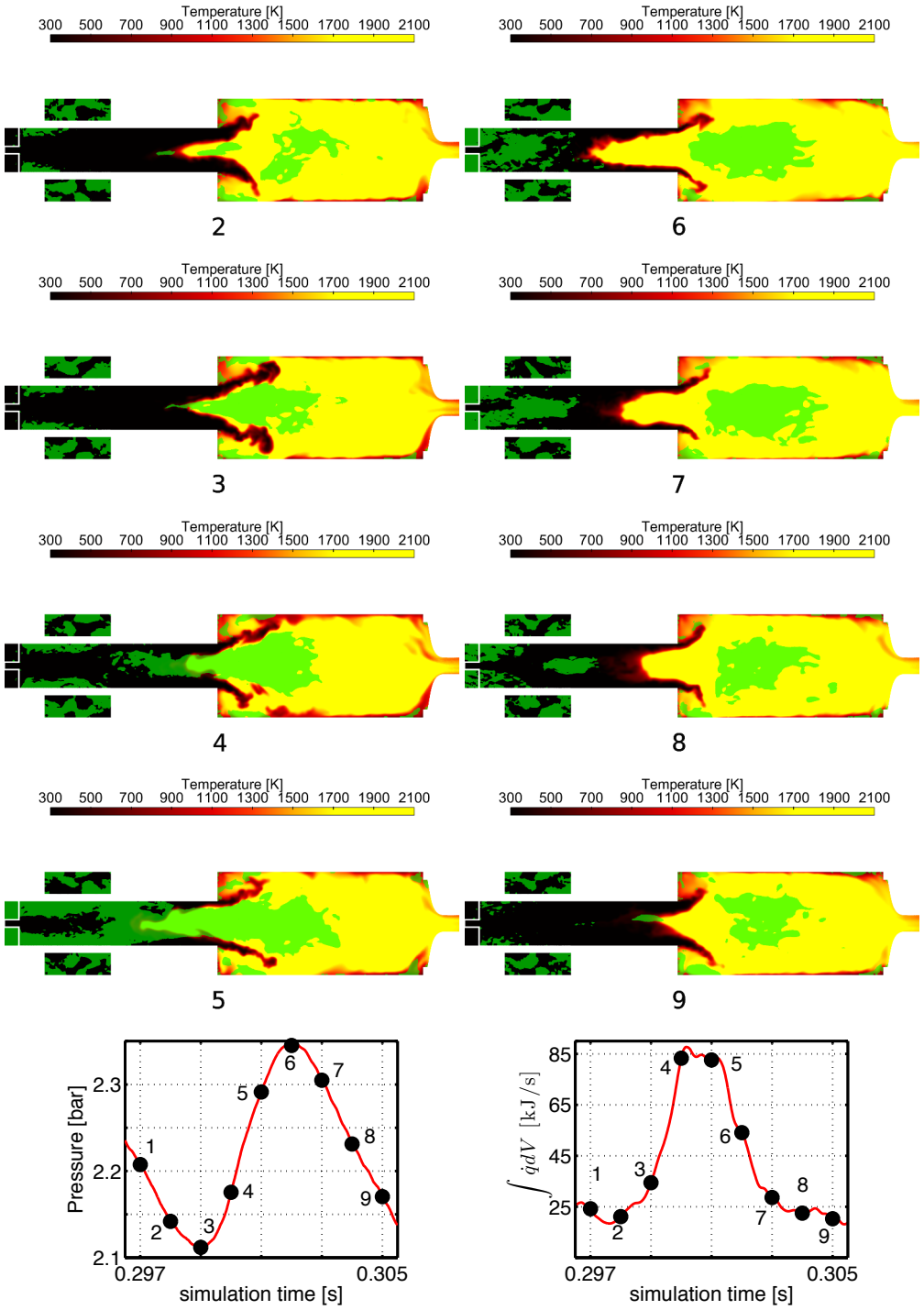

Figure 6.14: *LES snapshots of temperature field for case op16-2-0-85. The green zone corresponds to the flow with non positve axial velocity $u \leq 0$. Snaptshot numbers are shown in the pressure signal from probe located at $(x, y, z) = (0, 0, 0)$, and also in volume integrated heat release rate. The time interval between 2 snapshots is 1 ms.*

6.4.2 DMD analysis of LES fields

From the description of the limit cycle presented in Sec. 6.4.1, it is shown that acoustic and velocity fluctuations are coupled in the burner. This coupling is now analysed with Dynamic Mode Decomposition (DMD) of LES fields. The following will first be dedicated to the theoretical background of DMD.

6.4.2.1 Dynamic mode decomposition

Dynamic mode decomposition is a popular tool to analyse experimental measurements or numerical simulations of a flow in complex geometries. It decomposes the flow into temporally and spatially coherent structures and allows stability analysis of relevant flow process. The starting point is a sequence of N time-resolved experimental or numerical snapshots of the evolving flow, given by V_1^N

$$V_1^N = \{v_1, v_2, v_3, ..., v_N\} \tag{6.2}$$

where v_i stand for the ith snapshot of the flow. Supposing that the snapshots are taken at a constant time interval Δt, one has:

$$AV_1^{N-1} = A\{v_1, v_2, v_3, ..., v_{N-1}\} = \{v_2, v_3, v_4, ..., v_N\} = V_2^N \tag{6.3}$$

In the above expression, A is a linear operator which approximates the true state operator that could be nonlinear. Flow modes, their frequencies and growth rates can then be examined from the eigenvalues and eigenvectors of the operator A. Several methods to calculate A have been developed in the literature and they mainly differentiate in the way to decompose the snapshot sequence V_1^{N-1}. For example the QR decomposition based on a companion matrix in Schmid (2011); Schmid et al. (2011), or singular value decomposition (SVD) in Schmid (2010); Jovanović et al. (2014). This work uses the SVD method to expand V_1^{N-1}, accordingly:

$$V_1^{N-1} = U\Sigma W^* \tag{6.4}$$

Here W^* stands for the complex-conjugate-transpose of matrix W. Substituting the SVD into Eq. (6.3) and after some rearrangement, one has:

$$U^*AU = U^*V_2^N W\Sigma^{-1} = F \tag{6.5}$$

The advantage of this construction is that the matrix in the right hand side, F, shares the same eigenvalues as A and is only $(N-1) \times (N-1)$ in dimension. This procedure is also robust even if V_1^{N-1} is rank-deficient (Schmid 2010). The dynamic modal structures Φ_i and their temporal evolution C_i of the system

operator A are then extracted based on the eigenvalues λ_i and eigenvectors X_i of the low-dimensional operator F:

$$\{\Phi_1, \Phi_2, \Phi_3, ..., \Phi_{N-1}\} = U\{X_1, X_2, X_3, ..., X_{N-1}\} \tag{6.6}$$

$$\{C_1, C_2, C_3, ..., C_{N-1}\} = \{X_1, X_2, X_3, ..., X_{N-1}\}^{-1} \Sigma W^* \tag{6.7}$$

In what follows, DMD analysis has been used to extract relevant structures from LES fields in the central plane $z = 0$. The snapshots sampled at 1 000 Hz have been used in the post-processing, corresponding to 8 snapshots per cycle of the self-sustained instability (128 Hz). The analysis are therefore limited to 500 Hz. This sampling rate is sufficient to extract pertinent flow processes according to Schmid (2010).

6.4.2.2 DMD results

A sequence of 100 instantaneous LES fields on the central plane $z = 0$ containing pressure, temperature and velocity informations are now post-processed using DMD. The length of the sequence corresponds to 12 instability cycles. Although not detailed in the following, several DMD tests have been conducted by changing the number of snapshots and time-shifting the sequence of snapshots, all yielding distinctive modes with frequencies shifted only by a few tenth of Hz.

Fig. 6.15 gives the amplitude spectrum of axial velocity, pressure and temperature in the median plan for the op16-2-0-85 case. All three flow quantities share the oscillatory mode at 129 Hz, which is only 1 Hz higher than the frequency found by the Fourier analysis of the temporal pressure signals (see Fig. 6.10(b)). This not only confirms the coupling of the acoustic and velocity fluctuations illustrated in Fig. 6.14, but also indicates that the largest temperature fluctuations are generated by the thermoacoustic instabilities. Fig. 6.16 illustrates the fluctuating temperature field during one cycle of the DMD mode at 129 Hz. The reaction zone in the chamber moves periodically in axial direction. This produces large temperature fluctuations that are convected by the flow towards the chamber end.

6.4.3 Conclusion

For concluding this section, the analysis of the LES of the case op16-2-0-85 showed that the self-sustained combustion instability results from the coupling of acoustic and velocity perturbations in the burner. The high-amplitude acoustic fluctuations cause periodical displacement of the reaction zone in the injector

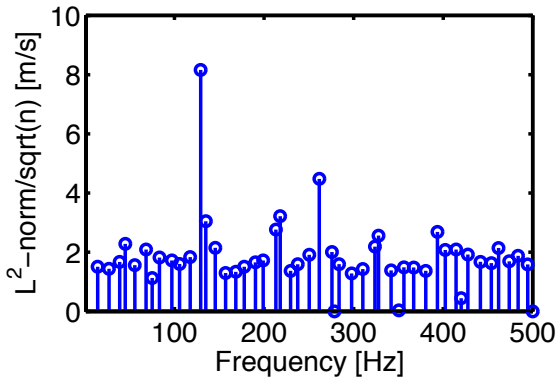

(a) Axial velocity

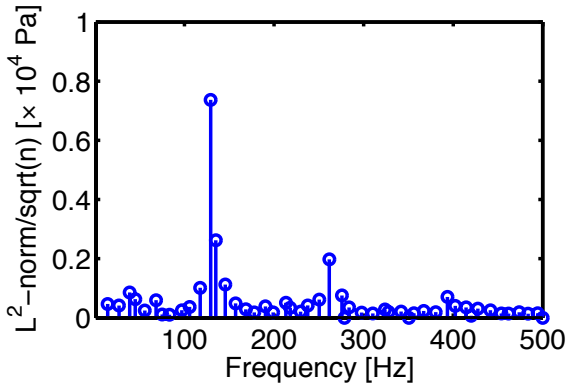

(b) Pressure

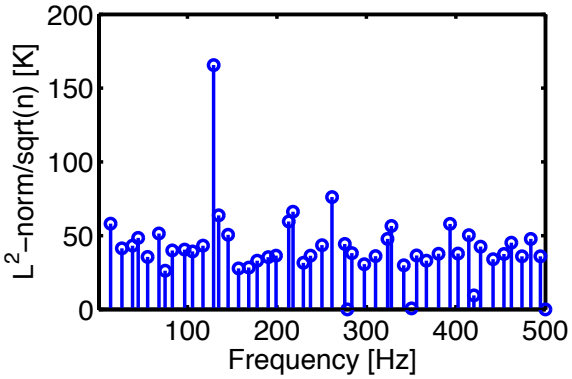

(c) Temperature

Figure 6.15: *Axial velocity, pressure and temperature amplitude spectrum from DMD analysis of instantaneous field in longitudinal plane $z = 0$. Amplitude calculated using the L^2-norm of the modes in median plane devided by square-root of the nodal points. Case op16-2-0-85*

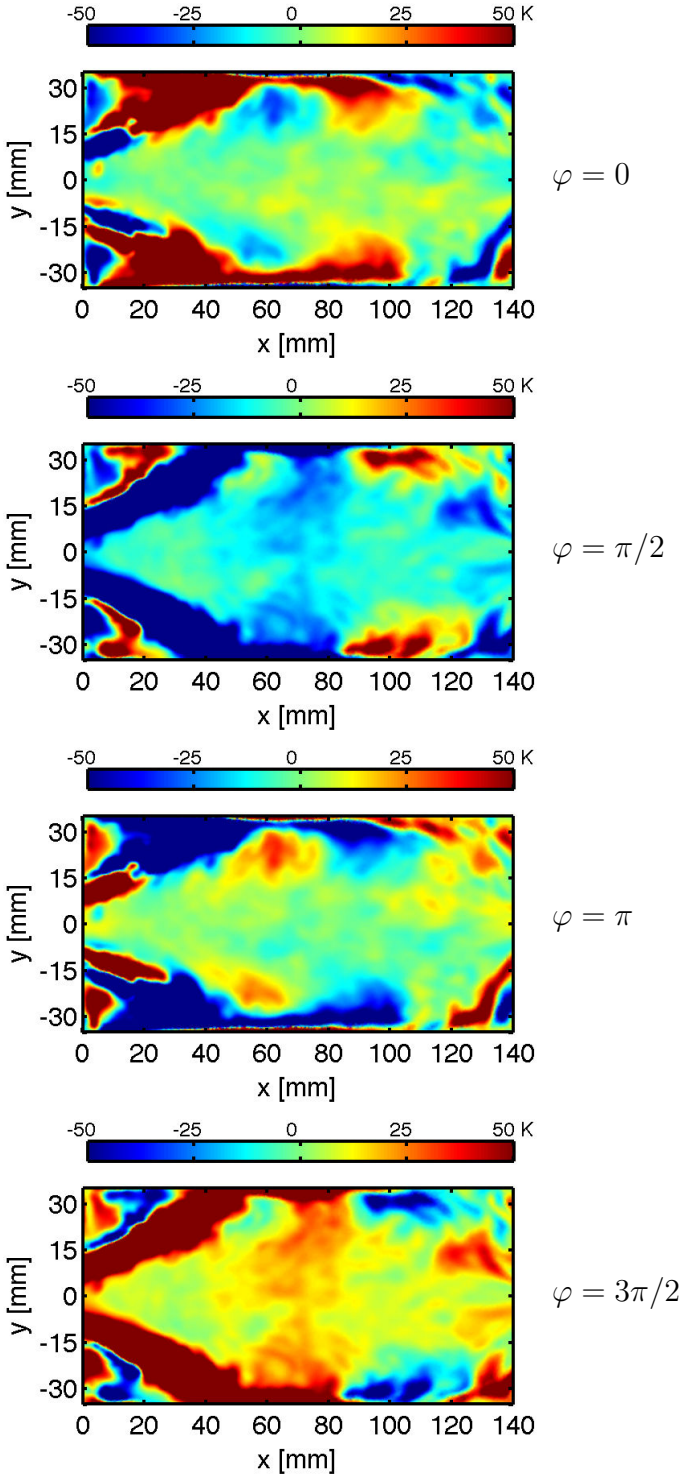

Figure 6.16: *Fluctuating temperature field in longitudinal plane $z = 0$ from the DMD mode at 129 Hz for case op16-2-0-85*

and accordingly the evolution of heat release rate. From the DMD analysis, it is further shown that the displacement of the reaction zone is responsible for large structure of temperature inhomogeneities in the flow approaching the nozzle.

6.5 Analysis of the temperature fields at the end of combustion chamber

In order to assess the indirect combustion noise contribution, it is necessary to quantify the entropy fluctuations upstream of the nozzle. Since temperature fluctuations are good indicator for entropy inhomogeneities, the temperature fields at the end of the combustion chamber have been examined both from statistical and spectral aspects in this section. The analysis in this section will also focus on the case op16-2-0-85.

6.5.1 Time-resolved LES fields in the cross sections at the chamber-end

To obtain the temperature field at the chamber-end with a high time resolution, interpolation of the instantaneous 3D LES field from the original unstructured mesh to a structured grid has been carried out every 150 iterations during 100 ms of simulation time. This *real-time* interpolation allows to have a large amount of LES data with a short incremental time for minimum memory requirement.

Fig. 6.17 gives the interpolation grid. It consist of eight transversal planes equally spaced by 7 mm, each of them are discretized by 35×35 2×2 mm^2 squares. The original smallest length scale of the unstructured mesh in this region is 1 mm, structures on the transverse plane with a length scale between 1 and 2 mm are therefore filtered by the interpolation. In axial direction, the spatial sampling is properly tailed for length scales larger than 3.5 mm according to the Nyquist–Shannon sampling theorem. Information on smaller structures may be lost due to interpolation, but they are not particularly of interest for studying combustion noise since they correspond to large wave numbers. The interpolation time step varies slightly due to the explicit marching time in the AVBP code. The final time series are re-sampled to give a sampling rate of 50 000 Hz.

Fig. 6.18 gives the time-averaged and root-mean-square 2D temperature fields on three transversal planes. The images are so organised that we are looking towards the upstream of the chamber. The top, right and bottom boundaries

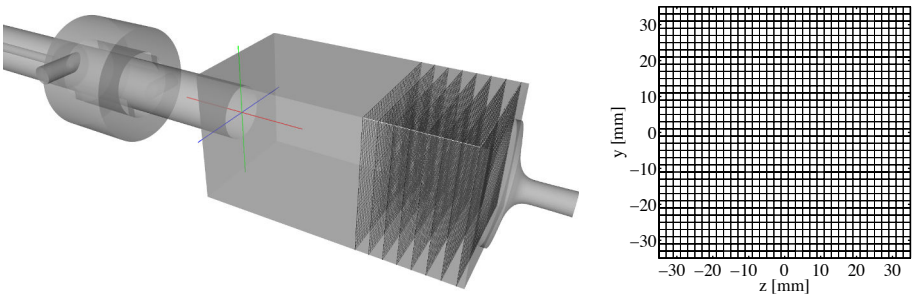

(a) (b)

Figure 6.17: *Interpolation grid. Eight* 70×70 mm^2 *transversal planes starting from* $x = 87.5$ *to* $x = 136.5$ *mm with an equal distance of 7 mm and discretized by square grids of* 2×2 mm^2.

correspond to the chamber walls with heat losses, and the left wall is treated as adiabatic. This results in lower mean and higher root-mean-square temperature near the cooled walls. As the flow advances to the nozzle, the rotational momentum increases, entraining gas from the wall towards the chamber center. As the circumferential velocity is accelerated by the nozzle, entropy inhomogeneities can also be converted into sound. The possible sound production related to this phenomenon is however not treated in the thesis, instead the instantaneous LES fields at the end of the combustion chamber are averaged in cross sections to give 1D temporal signals in the following.

6.5.2 Extraction of 1D time series

Fig. 6.19 gives the temporal evolution of surface-averaged pressure and temperature signals on the plane at $x = 122.5$ mm for the reactive case op16-2-0-85. These signal are normalised by their temporal mean values respectively. The pressure and temperature fluctuations are all within 10% of their mean values.

Entropy fluctuations are now evaluated using cross-sectional averaged LES data. It has been shown that combustion instability is the dominant process in the burner. Acoustic is by nature an isentropic process, it is thus necessary to verify first if entropy fluctuations are generated in the flow approaching the nozzle. To do so, the temperature fluctuations generated by isentropic processes T'_{is} have been subtracted from the total temperature fluctuations T'. This was achieved by combining the equations $c^2 = (\partial p/\partial \rho)_s$ and $p = r\rho T$, which gives $T'_{\text{is}}/T = (\gamma - 1)p'/\gamma p$. The difference $T'_s = T'_t - T'_{\text{is}}$ is then proportional to entropy fluctuations by $s'/c_p = T'_s/T$ according to the perturbation form of the entropy function $s = c_v \ln(p/\rho^\gamma)$.

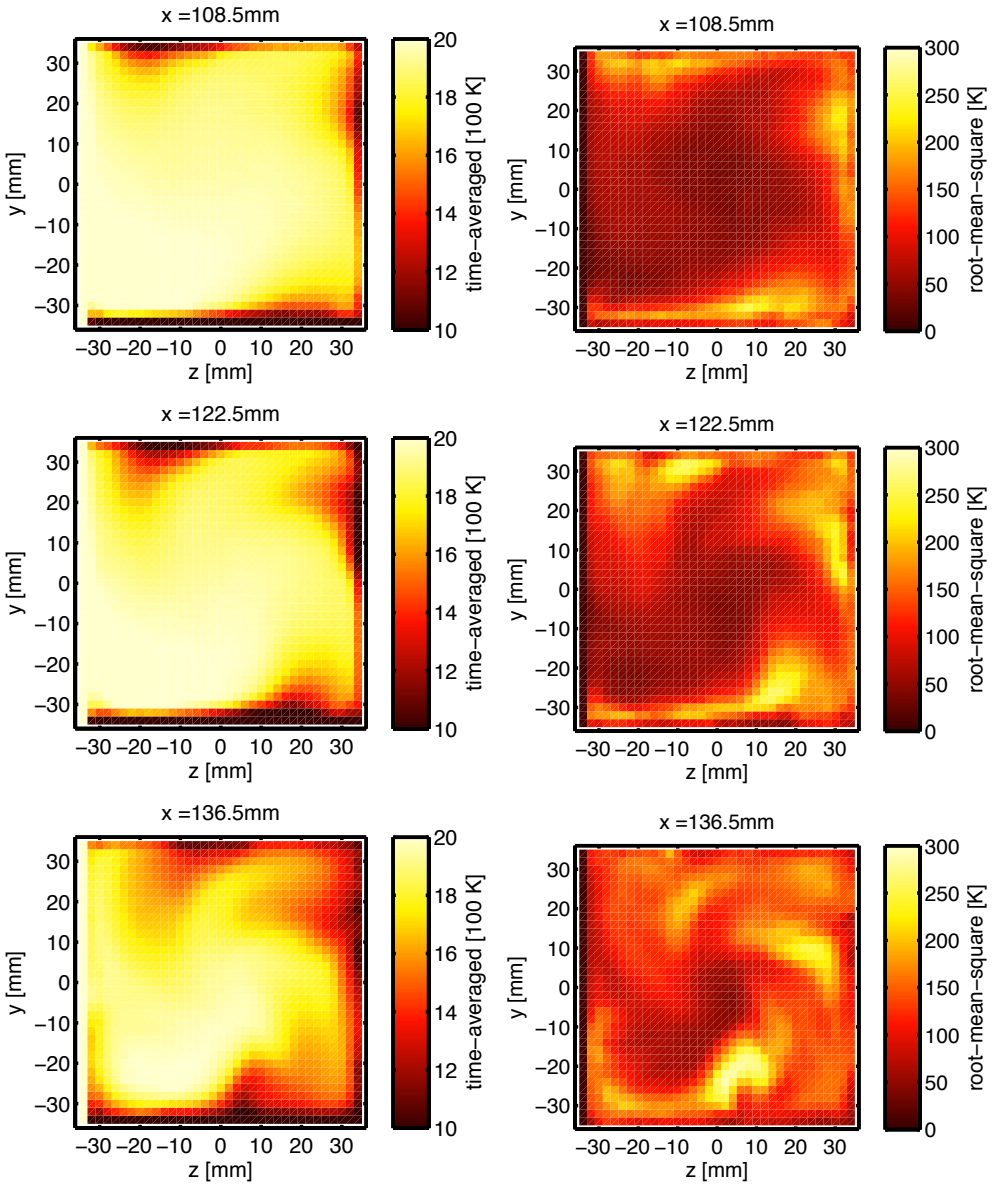

Figure 6.18: *Mean (left) and root-mean-square (right) temperature field of the transverse planes on $x = 87.5$ mm (top), $x = 122.5$ mm (middle) and $x = 136.5$ mm (bottom). From interpolated LES simulations of the op16-2-0-85 case.*

Fig. 6.20 compares the amplitude spectra of T' and T'_{is}. The total temperature fluctuations seem to be the superposition of the isentropic temperature fluctuations with a broad band part, or the so-called non-isentropic temperature fluctuations, which are in the next step compared with Laser interferometric Vibrometer (LIV) measurements in Fig. 6.21. LIV technique (see for example in Leitgeb et al. (2013)) measures the instantaneous density fluctuations integrated along the laser beam. The raw LIV signal contains contributions from vibrations and changes of the refractive index in the flow due to turbulence, acoustic and temperature. The strategy proposed by Kings et al. (2015); Kings et al. (2016) consists to extract from the raw LIV signals the excess density fluctuations that are related to entropy disturbances and that are used to evaluate the instantaneous line-of-sight averaged temperature fluctuations shown in Fig. 6.21. LIV measurements are conducted during 10 s. This is long enough to remove non consistent temperature fluctuations and the amplitude spectra as a result has high amplitude at a few distinctive frequencies. The amplitude spectra from LES, on the contrary, present more contents in low frequency range due to the short sample duration. Nevertheless, the amplitude of temperature fluctuations at the self-sustained oscillation frequency is well predicted by LES. These results confirm the presence of entropy fluctuations both in experiments and simulations and make it reasonable to determine acoustic and entropy waves from the cross-correlation of pressure and temperature fluctuations as will be presented in the next chapter.

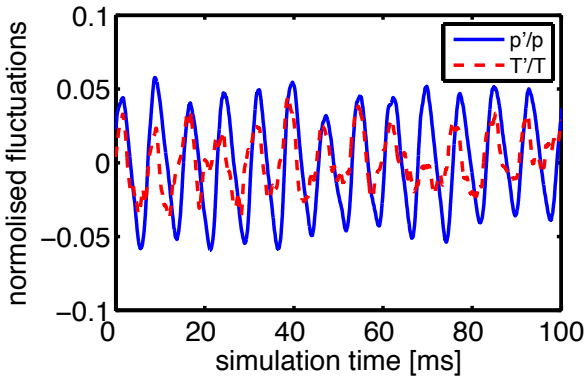

Figure 6.19: *Normalised surface-averaged pressure and temperature fluctuations at* $x = 122.5$ *mm from LES simulations*

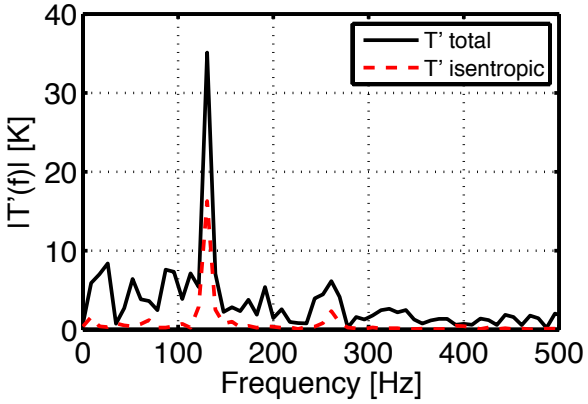

Figure 6.20: *Amplitude spectrum of total and acoustic temperature fluctuations at* $x = 122.5$ *mm.*

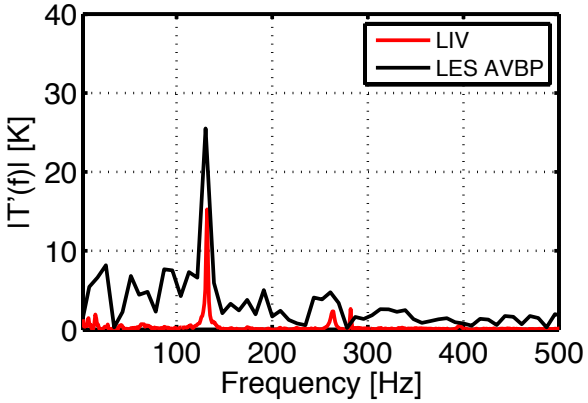

Figure 6.21: *Amplitude spectrum of surface-averaged temperature fluctuations at* $x = 122.5$ *mm. LES (black line) and LIV (red line).*

Chapter 7

Combustion noise analysis

The objective of this chapter is to analyse combustion noise in the CESAM-HP burner using LES simulations and the diff-R method. Combustion noise sources, characterised by acoustic and entropy waves propagating towards the nozzle, are computed first directly from LES simulations. The direct noise and the entropy-generated noise that propagate towards the upstream of the combustion chamber are then computed using the compact nozzle transfer functions. The combustion noise sources, direct and indirect noise contributions in the acoustic feedback of the nozzle are also determined with the diff-R method using simulation signals. The comparison of the two approaches has been dedicated to the op16-2-0-85 case and showed satisfying agreement.

7.1 From 2D LES fields to 1D time series

The diff-R method requires to compute the cross-correlation between one dimensional pressure and temperature signals measured in the same cross-section. The eight cross sections in Fig. 6.17 have been chosen to compute the correlation. A schematic view of these sections is given in Fig. 7.1. For each section, a projection of the 2D LES data to 1D time series is needed and the way to convert data may change the acoustic source term computation. The methodology to extract one-dimensional time series is here investigated.

The surface-averaged temperature $T'_{av}(x,t)$ and the temperature fluctuations $T'(x,y,z,t)$ measured at any point of the surface A are linked through relation in Eq. (7.1). The cross-correlation of a time-varying quantity $\Phi(t)$ with the surface-averaged temperature is given by Eq. (7.2). The later shows that using the section-averaged or the central point temperature is equivalent if C_{00} equals

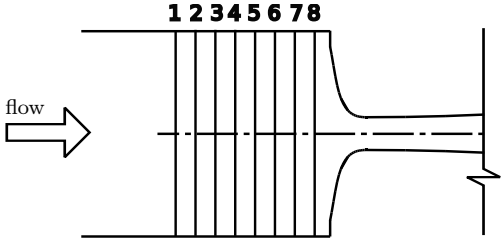

Figure 7.1: *Schematic view of the 1D configuration for combustion noise analysis. 1st plane at $x = 87.5$ mm, 8th plane at $x = 136.5$ mm*

unity. C_{00} evaluates the inhomogeneity of the temperature field in the cross-section depending on the time scale. Perfectly homogeneous temperature fields in the cross-section for all the time steps will give C_{00} the unity value.

$$T'_{av}(x,t) = \frac{1}{A}\int T'(x,y,z,t)dydz \tag{7.1}$$

$$\begin{aligned}\hat{T}_{av}(x)\hat{\Phi}^* =& \frac{1}{A}\int \hat{T}(x,y,z)\hat{\Phi}^* dydz = \frac{1}{A}\int \frac{\hat{T}(x,y,z)}{\hat{T}(x,0,0)}\hat{T}(x,0,0)\hat{\Phi}^* dydz \\ =& \hat{T}(x,0,0)\hat{\Phi}^* \underbrace{\left(\frac{1}{A}\int \frac{\hat{T}(x,y,z)}{\hat{T}(x,0,0)}dydz\right)}_{C_{00}}\end{aligned} \tag{7.2}$$

Taking surface-averaged pressure data for Φ in Eq. 7.2, its cross-correlation with surface-averaged temperature fluctuations, temperature fluctuations measured at $(y,z) = (0,0)$ and its corrected version by the C_{00} factor are plotted in Fig. 7.2. The cross-correlations computed with the three methods are very similar up to 300 Hz. From 400 Hz, the use of the local temperature tends to overestimate the correlation whereas the corrected local temperature allows to recover the correlation. The correction takes mainly effects for high frequencies which is reasonable since small frequencies represent large scale coherent temperature structures.

The combustion noise analysis presented in the following is proceeded with surface-averaged LES data, which are sampled at 50 000 Hz during 100 ms. We will show at the end of the chapter that the combustion noise analysis with the diff-R method using C_{00} corrected single point signals gives results similar to the analysis with surface-averaged data.

All the analysis results are presented in frequency domain. Due to the short signal length, Fourier transform combined with a Gaussian window has been applied to the entire signal, yielding a frequency resolution of 10 Hz.

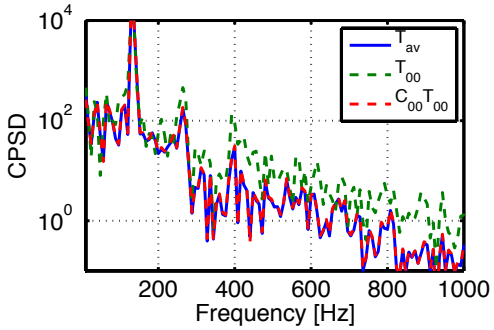

Figure 7.2: *Cross-correlation of surface-averaged pressure fluctuations with surface-averaged temperature fluctuations, temperature fluctuations measured at* $(y, z) = (0, 0)$ *and its corrected version by the* C_{00} *factor. For the case op16-2-0-85 and on the tranversal plane at* $x = 136.5$ *mm.* C_{00} *factor is integrated over all nodal points in the plane.*

7.2 Combustion noise analysis using LES simulations

This section first calculates the combustion noise sources, designated by acoustic and entropy waves approaching the nozzle, using pressure, velocity and temperature data at the 8th axial position $x = 136.5$ mm in Fig. 7.1. The progressive and regressive acoustic waves are obtained from characteristic wave decomposition given by Eq. (7.3) and (7.4), and the entropy wave is calculated according to Eq. (7.5).

$$P_u^+ = \frac{1}{2}\left(\frac{p'}{\gamma p} + \frac{u'}{c}\right) \tag{7.3}$$

$$P_u^- = \frac{1}{2}\left(\frac{p'}{\gamma p} - \frac{u'}{c}\right) \tag{7.4}$$

$$\sigma = \frac{s'}{c_p} = \frac{T'}{T} - (\gamma - 1)\frac{p'}{\gamma p} \tag{7.5}$$

Fig. 7.3(a) gives the amplitude spectrum of normalised incident and reflected acoustic waves, P_u^+ and P_u^- respectively, and the entropy wave σ. The amplitude of entropy wave tends to decrease as the frequency increases. This limits the following analysis of combustion noise to 1 000 Hz, above which the amplitude of temperature fluctuations drops below 1 K. The acoustic waves P_u^+ and P_u^- are identical for the reason that will be discussed below.

It has been shown in Sec. 1.1 that apart from the reflection of incident acoustic wave, sound is also generated by the accelerated entropy wave in the nozzle. Therefore there are both direct P_{ua}^- and indirect P_{us}^- contributions in the acoustic feedback of the nozzle P_u^-. It is now convenient to calculate the direct and

entropy noise contributions in the combustion chamber using the analytical compact nozzle transfer functions:

$$\mathcal{R}_a^{\text{choked}} = \frac{P_{ua}^-}{P_u^+} = \frac{1 - \frac{1}{2}(\gamma - 1)M_u}{1 + \frac{1}{2}(\gamma - 1)M_u} = 0.9970 \tag{7.6}$$

$$\mathcal{R}_s^{\text{choked}} = \frac{P_{us}^-}{\sigma} = -\frac{\frac{1}{2}M_u}{1 + \frac{1}{2}(\gamma - 1)M_u} = -0.0058 \tag{7.7}$$

with the nozzle inlet Mach number $M_u = 0.0115$ and $\gamma = 1.26$ from surface-averaged LES data of the presented case. It is noted that up to 600 Hz the entropy wavelength is smaller than the length of convergent part of the nozzle (15 mm). This is the reason why the analytical entropy generated noise from compact nozzle transfer functions is limited to 600 Hz. Since the nozzle compactness is well satisfied for acoustic wave, indirect noise contributions can be computed by subtracting the direct contributions from the total acoustic feedback, or $P_u^- - \mathcal{R}_a P_u^+$ mathematically. This approach actually follows the same principle from which the diff-R method has been developed, as will be discussed in the next section.

Fig. 7.4(a) gives the direct and indirect noise contributions in the combustion chamber measured in sound pressure level. The direct reflection coefficient in Eq. (7.6) equals almost to unity, meaning that the nozzle is fully reflective. This is the reason why acoustic waves P_u^- and P_{ua}^- collapse with each other. Interestingly, the obtained indirect noise contribution is at least 11 dB higher than the analytical compact solution for entropy noise at the frequency of combustion instability (129 Hz). Although no measure for the vorticity has been carried out yet, the excess indirect noise contributions other than the entropy contribution is suspect to be generated by vortex shedding from the swirling flow. This is one particularity of the burner where a large recirculation zone (see Fig. 6.14) is formed in the middle of the combustion chamber. At this point, it may be insufficient to consider only entropy wave as the source of indirect noise generation in the CESAM-HP burner, further quantification of vorticity generated sound seems necessary to close the problem of indirect noise contributions. Nevertheless, the direct contribution P_{ua}^- dominate the indirect contribution P_{us}^- upstream of the nozzle in the current LES simulation case. This results in the identity of the progressive and regressive acoustic waves shown in Fig. 7.3(a).

7.3 Combustion noise analysis with the diff-R method

The diff-R method developed in Sec. 4.1 is now used to analyse combustion noise from LES simulations of the CESAM-HP burner. The measurement positions

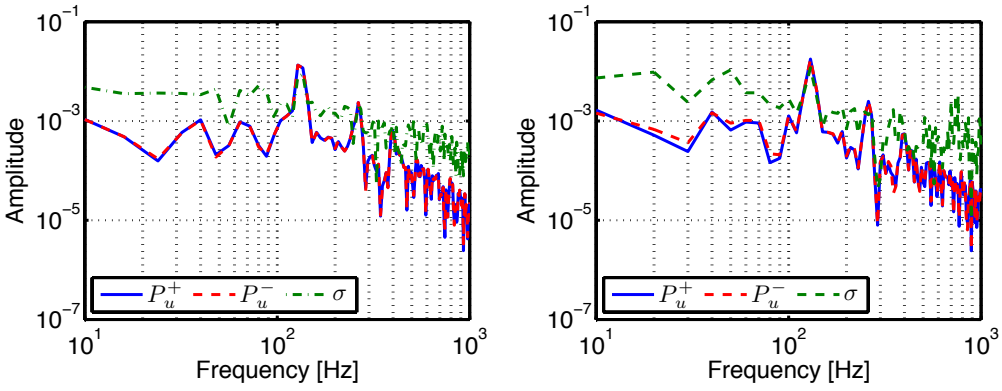

(a) LES (b) diff-R method

Figure 7.3: *Amplitude spectrum of normalised acoustic and entropy waves upstream of the nozzle at $x = 136.5$ mm determined (a) directly from LES simulations using characteristic wave decomposition and (b) with the diff-R method.*

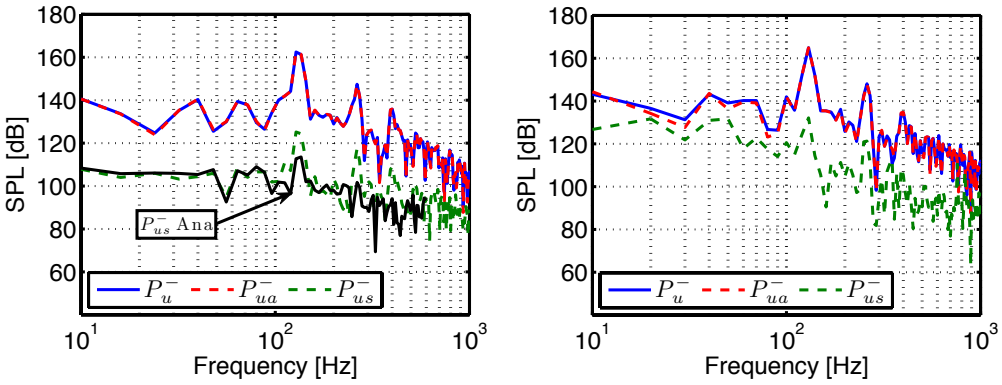

(a) LES (b) diff-R method

Figure 7.4: *Sound pressure level of direct and indirect noise contribution in the acoustic feedback of the nozzle calculated (a) directly from LES simualtions using characteristic wave decomposition and analytical compact nozzle transfer functions and (b) with the diff-R method.*

are determined first following the principles proposed in Sec. 3.2 and 4.2.2: the temperature measurement position is chosen close to the nozzle inlet at $x = 136.5$ mm and coincides with the downstream pressure measurement position. The upstream pressure measurement position is set at the largest available distance from its downstream counterpart, so at $x = 87.5$ mm. This choice aims to increase low-frequency measurement accuracy of the nozzle reflection coefficient.

The diff-R method needs to measure the nozzle reflection coefficient $\mathcal{R} = P_u^-/P_u^+$ and the complex ratio, or the complex ratio of incident entropy to acoustic waves $H_{sa} = \sigma/P_u^+$. In what follows , the two parameters are measured in the first place from numerical pressure and temperature signals by methods presented in Sec. 3.2 and 3.4. They are used in the next step to compute the acoustic and entropy waves upstream of the nozzle. The indirect noise contributions are finally evaluated from the formerly determined parameters using the diff-R method.

7.3.1 Computations of $\mathcal{R}$ and H_{sa}

Now the nozzle reflection coefficient $\mathcal{R}$ at $x = 136.5$ mm is measured with the Two-microphone Method based on the transfer function of the two pressure measurements (see Sec. 3.2). The occurrence of the combustion instability indeed provides consistent acoustic sources. This generates coherent pressure oscillations and the Two-microphone method can be properly implemented over a large frequency range up to 1 000 Hz. The complex ratio $H_{sa} = \sigma/P_u^+$ is measured based on the complex ratio of pressure and temperature fluctuations measured both at $x = 136.5$ mm (see Sec. 3.4).

The obtained $\mathcal{R}$ and H_{sa} are compared to the same parameters obtained from characteristic wave decomposition of LES data in Fig. 7.5. In general the coefficients obtained by characteristic wave decompositions were well found using only two pressure and one temperature measurements. This is reasonable since they share the same theoretical background based on the assumption of planar and linear waves propagations. The differences between the two approaches results from two facts. First, the spectral analysis for frequencies lower than 100 Hz was very sensitive to the size of the window function used in the Fourier analysis, which is an indication for not enough cycles of small frequency signals. This affects the estimation of the parameters from both approaches. Second the complex acoustic and entropy wave propagation between the two measurement positions. As discussed in Sec. 2.2, the two pressure sensor technique is not designed to handle problems such as wave dissipations and dispersions that are likely to occur in a complex flow.

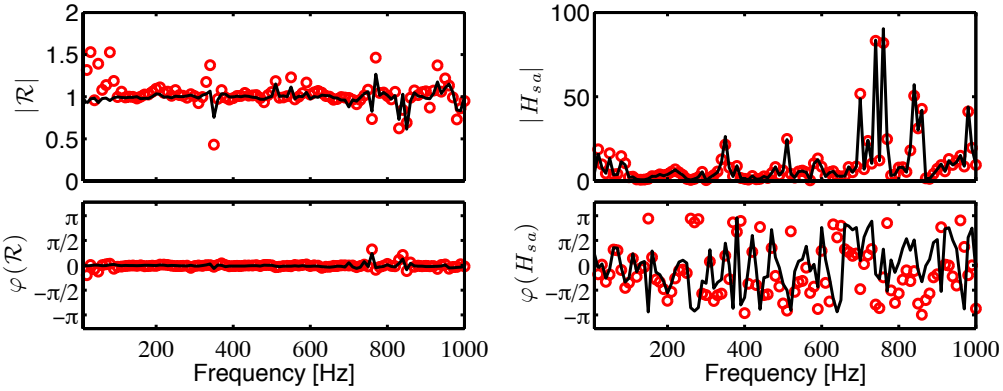

(a) $\mathcal{R}$ (b) H_{sa}

Figure 7.5: *Nozzle reflection coefficient and the complex ratio of incident entropy to acoustic waves. Lower frequency limit is 10 Hz. Line: Characteristic wave decomposition. Symbols: diff-R method.*

7.3.2 Determination of upstream acoustic and entropy waves

In this section, the incident acoustic and entropy waves P_u^+ and σ are determined from the previously measured reflection coefficient and the complex ratio $H_{sa} = \sigma/P_u^+$. The progressive and regressive acoustic waves P_u^+ and P_u^- are obtained from plane wave decomposition using the nozzle reflection coefficient $\mathcal{R}$ measured at $x = 136.5$ mm. The entropy wave σ is then compute from P_u^+ and $H_{sa} = \sigma/P_u^+$. The amplitude spectrum of incident acoustic and entropy wave, as well as the reflected acoustic wave P_u^- are given in Fig. 7.3(b). Due to the differences in the $\mathcal{R}$ and H_{sa} measured in the previous step, their amplitudes were slightly higher than those given directly by LES simulations over the whole frequency range from 10 to 1 000 Hz.

Fig. 7.6 shows the amplitude of entropy wave obtained following the same procedure presented above but with temperature fluctuations measured on a single point $(y, z) = (0, 0)$ in the cross section at $x = 136.5$ mm. It has been mentioned in Sec. 7.1 that it is necessary to correct single point measurement in the case when temperature fluctuations are not homogeneous in the cross section ($C_{00} \neq 1$). After the correction by the factor C_{00}, single point measurement found similar results as the section-averaged data.

7.3.3 Determination of indirect noise contribution

The diff-R method now proceeds to evaluate separately the direct (P_{ua}^-) and indirect (P_{us}^-) noise contributions in the reflected wave upstream of the noz-

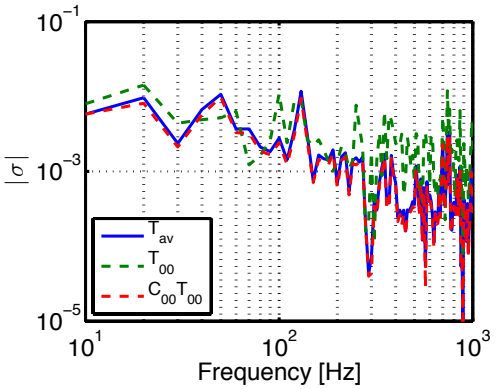

Figure 7.6: *Amplitude spectrum of entropy wave from diff-R method using cross section averaged temperature fluctuations, temperature fluctuations measured at* $(y, z) = (0, 0)$ *and its corrected version by the* C_{00} *factor. For the case op16-2-0-85 and on the tranversal plane at* $x = 136.5$ *mm.* C_{00} *factor is integrated over all nodal points in the plane.*

zle P_u^-. The direct contribution P_{ua}^- is calculated from the previously determined direct noise source P_u^+ and the compact nozzle transfer function given in Eq. (7.6). The indirect contribution is obtained by making the subtraction $P_{us}^- = P_u^- - P_{ua}^-$. These normalised waves are finally converted into sound pressure level and presented in Fig. 7.4(b). The diff-R method measured the direct and indirect noise contributions that were in good agreement with the LES results (Fig. 7.4(a)), although there was as high as 20 dB in difference for frequencies below 100 Hz. These differences were indeed due to inaccuracy of the measurement of $\mathcal{R}$ using two pressure sensors at low frequencies (see Fig. 7.5(a)).

Finally, the indirect nozzle reflection coefficient is computed from the diff-R method using $\mathcal{R}_s = (\mathcal{R} - \mathcal{R}_a)/H_{sa}$. The frequencies below 100 Hz has been cut off due to the large differences between the reflection coefficient measured from two pressure sensors and from characteristic wave decomposition. Additionally, the indirect reflection coefficient has also been computed directly from LES simulations by $\mathcal{R}_s = (P_u^- - P_{ua}^-)/\sigma$. Fig. 7.7 summarises the modulus of the nozzle indirect reflection coefficients evaluated from two approaches and the analytical indirect reflection coefficient for compact nozzle as well. Although $|\mathcal{R}_s|$ showed large dispersion around the compact solution over the whole frequency range, the value obtained directly from LES simulations matches better with the compact solution. This gives two informations: for entropy wave the nozzle can be still considered compact up to 1 000 Hz, although the obtained indirect reflection coefficient may also include contribution from vorticity fluctuations; the larger deviation from the compact solution of the measurement with diff-R method is mainly due to the inaccuracy in the measurement of nozzle reflection

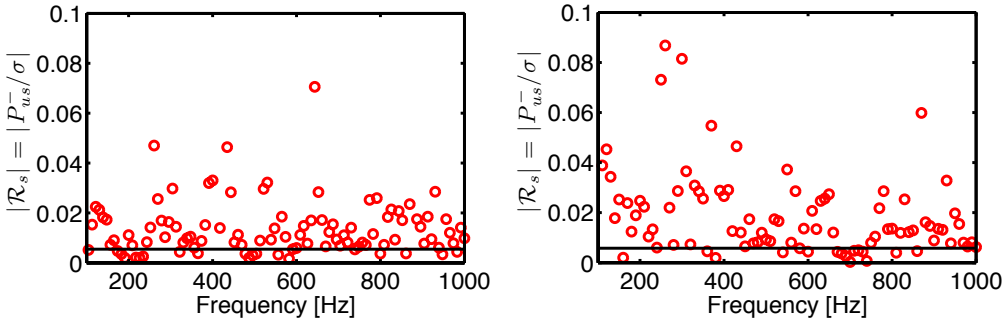

(a) LES (b) diff-R method

Figure 7.7: *Indirect nozzle reflection coefficients calculated (a) directly from LES simulations using characteristic wave decomposition and (b) with the diff-R method. Lower frequency limit is 100 Hz.*

coefficient $\mathcal{R}$ in a complex flow where wave dispersions and dissipations can not be ignored.

7.4 Conclusion

In this chapter the determination of combustion noise sources, the separation of direct and indirect noise contributions in the acoustic feedback of the nozzle have been carried out in two ways: one applies the characteristic wave decomposition directly on LES simulations and one uses the diff-R method with pressure and temperature measurements at different positions. The combustion noise sources, designated by the incident acoustic and entropy waves near the inlet of the nozzle have been determined and were found similar from the two approaches. The direct and indirect noise contributions upstream of the nozzle were also in good agreement except for frequency lower than 100 Hz, where the signal length is limited and the measurement accuracy of the nozzle reflection coefficient drops as well. These examinations also inferred possible indirect noise contribution from vorticity fluctuations, and its quantification seems necessary for the combustion noise analysis of the CESAM-HP burner.

Conclusion

The determination of the direct and indirect combustion noise contributions from pressure and temperature fluctuations measurements in combustion chambers closed by nozzles is treated in this thesis. Focused on the upstream region of the nozzle, this work had proposed an experimental methodology to evaluate entropy generated pressure fluctuations in acoustic feedback of the nozzle.

The main difficulty that the current work aims to overcome is that the noise sources, designated by acoustic and entropy waves propagating towards the nozzle, are generated both by the unsteady combustion process and are usually coherent over a large frequency range where the magnitudes of noise sources are relatively high.

To tackle this problem, some hypothesis have been made first. The propagation of the acoustic and entropy waves were assumed one-dimensional. The dissipation and dispersion of these waves were also ignored. The amplitude of the pressure, velocity and temperature fluctuations were supposed to be small compared to their mean values. These hypothesis have allowed to linearise the governing Euler equations and to sum up algebraically direct and indirect noise contributions. Further more, the noise generation mechanisms can be depicted by nozzle transfer functions. In the assumed linear regime the nozzle transfer functions are determined by the inlet and outlet Mach numbers.

Based on the previous assumptions, the diff-R method has been developed to measure the direct and indirect nozzle reflection coefficients. It consists to subtract the direct reflection coefficient from the total reflection coefficient of the nozzle. With the knowledge of the downstream propagation acoustic and entropy waves, the subtraction is then used to calculate the indirect nozzle reflection coefficient.

The diff-R method requires the measurement of nozzle reflection coefficients and the downstream propagating acoustic and entropy waves. The experimental methods for this purpose have been developed by combining the Three-microphone method and the transfer functions between pressure and tempera-

ture fluctuations measured at same or close positions in the vicinity of the nozzle inlet. For temperature fluctuations measurements with Tw0-thermocouple sensor, the thesis have also proposed a method to estimate the time constants of thermocouples has also been proposed based on the transfer function between the two thermocouples.

The diff-R method has been then validated from both numerical and experimental approaches by comparing to analytical nozzle transfer functions. The numerical validation relied on a numerical case calculated by the SUNDAY code, a solver of the Euler equations governing the flow through nozzle with acoustic and entropy inhomogeneities. The experimental validation was conducted with the Temperature and Acoustic Fluctuations Generator. This is an original setup that generates velocity, pressure and temperature fluctuations by controllable harmonic loudspeaker modulation in the mainstream traversed by cross-flow jets at a higher temperature. The root-mean-square of the temperature fluctuations in the TAFG can reach as high as 15 K.

While the numerical validation proved the efficiency of the diff-R method, the experimental validation turned out to be more complex. Apart from the limits of applied experimental methods, for example the inaccuracy of the Three-microphone method in low frequency range adn the magnitude and phase differences between real gas temperature and the compensated temperature using the Two-thermocouple sensor, the level of entropy generated noise in the TAFG setup remained relatively low compared to the direct noise. The low signal-to-noise ratio in the measurements made the diff-R method very sensitive to signal noises. Besides, the relative high amplitude of the velocity modulation level during the TAFG experiments was also responsible for the errors in the evaluation of nozzle transfer functions with the diff-R method.

Keeping in mind the hypothesis and the possible sources of errors, the diff-R method has been applied in a complex reacting flow from Large Eddy Simulations. A laboratory scale combustor operating with a choked nozzle at the combustor outlet has been simulated using the 3D compressible LES code AVBP. LES results agreed well with experiments and thus provided high-fidelity numerical signals of inhomogeneous flow quantities approaching the nozzle. 1D temporal evolutions of pressure, velocity and temperature fluctuations at different position have been extracted from 3D LES fields. The assumption of small-amplitude fluctuations was justified. The onset of self-sustained combustion instability indeed generated mono-frequency pressure and temperature oscillations. Finally, diff-R method has computed successfully the direct and indirect noise sources in the combustion chamber as well as the indirect nozzle transfer functions for frequencies between 10 to 1 000 Hz. Results have shown that the the direct noise contribution dominated the acoustic feedback of the nozzle in the laboratory scale combustor under the explored conditions.

The performance of the diff-R method has been proved both from the TAFG setup without the complexity of combustion, and from the LES of the reactive flow in a laboratory scale combustor. Concerning the indirect reflection coefficient of the nozzle, discrepancies with the analytical solutions were still present in both cases, although the results were quite satisfying by keeping in mind that the relative contribution of entropy generated noise compared to the direct noise were weak in both cases. The diff-R method is thus promising for measuring direct and indirect noise contributions in the combustion chamber. Using simultaneous pressure and temperature measurements upstream and downstream of the nozzle, it is also possible to determine direct and indirect noise contributions in the near field downstream of the nozzle in future works.

Appendix A

Quasi-steady analysis of the TAFG setup

It has been found in the parametric study of the TAFG setup that the amplitude of temperature fluctuations in the TAFG setup is very sensitive mass flow rate of cross flow jets and the main stream. Instead of a complete study on the behaviour of jets in cross-flow, a quasi-steady analysis of the setup has been carried out in this section in order to optimize the system's performance in generating high amplitude temperature fluctuations.

A schematic view of hot air injection zone is presented in Fig. A.1, in which the main stream is represented by a constant mass flow rate $\dot{m}_1$, a constant temperature T_1 and an oscillating pressure $p_1(t) = p_1 + p_1'(t)$ due to loudspeaker forcing. In the low frequency limit ($\omega \to 0$), $p_1(t)$ is supposed to be uniform in the system but evolves with time. Cross flow jets at temperature T_2 are injected from the hot air plenum, and the pressure p_2 inside is supposed unaffected by the pressure changes in the main stream. This is reasonable for small injectors with small holes where the mean pressure drop $\Delta p = p_2 - p_1$ is large compare to $p_1'(t)$. Thus the total pressure drop from the plenum to the main stream $\Delta p - p_1'(t)$ controls the momentum flux of the hot air injected through the jets, and the fluctuating mass flow rate of the jets can be calculated by:

$$\dot{m}_2(t) = C_D A_2 \sqrt{2\rho_2 (p_2 - p_1'(t))} \tag{A.1}$$

where C_D and A_2 are the discharge coefficient and the total cross section surface area of the jet ducts, and ρ_2 is the density of the jet flow. Writing $\dot{m}_2 = C_D A_2 \sqrt{2\rho_2 \Delta p}$, Eq. A.1 can be approximated in first order by Eq. A.2 when $|p_1'(t)|/\Delta p \ll 1$.

$$\dot{m}_2(t) = \dot{m}_2 \left(1 - \frac{1}{2}\frac{p_1'(t)}{\Delta p}\right) \tag{A.2}$$

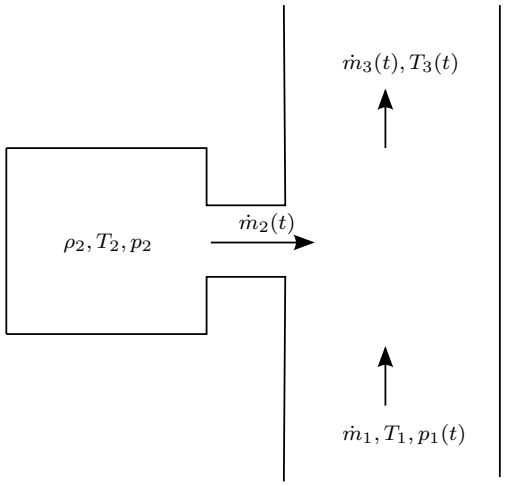

Figure A.1: *Schematic view of the cross flow jets injecting to the main stream*

Downstream of the cross-flow jets, the mass flow rate $\dot{m}_3(t)$ and the gas temperature $T_3(t)$ of the hot-cold air mixture are obtained by the mass and energy balance described in Eq. A.3 and A.4:

$$\dot{m}_3(t) = \dot{m}_1 + \dot{m}_2(t) \tag{A.3}$$

$$C_P \dot{m}_3(t) T_3 = C_P \dot{m}_1 T_1 + C_P \dot{m}_2(t) T_2 \tag{A.4}$$

where constant pressure heat capacities C_P is supposed the same in the different flow regions under the explored conditions. Combining the balance equations gives the gas temperature $T_3(t)$:

$$T_3(t) = \frac{\dot{m}_1 T_1 + \dot{m}_2(t) T_2}{\dot{m}_1 + \dot{m}_2(t)} \tag{A.5}$$

It is then possible to linearise the temperature fluctuations (Eq. A.5) by writing $T_3'(t) = T_3(t) - T_3$ where $T_3 = (\dot{m}_1 T_1 + \dot{m}_2 T_2)/(\dot{m}_1 + \dot{m}_2)$. For small pressure perturbations $p_1'(t)$ through a perturbation analysis. It gives:

$$\frac{T_3'(t)}{T_3} = -\frac{1}{2} \frac{p'(t)}{\Delta p} \left(\frac{\dot{m}_2 T_2}{\dot{m}_1 T_1 + \dot{m}_2 T_2} - \frac{\dot{m}_2}{\dot{m}_1 + \dot{m}_2} \right) \tag{A.6}$$

The factor α:

$$\alpha = \frac{\dot{m}_2 T_2}{\dot{m}_1 T_1 + \dot{m}_2 T_2} - \frac{\dot{m}_2}{\dot{m}_1 + \dot{m}_2} \tag{A.7}$$

in the right-hand-side of Eq. A.6 is a function of the mass flow rates if flow temperatures are considered constant for all configurations. In the cases for generating temperature fluctuations, $T_2 > T_1$ so that $\alpha > 0$. Eq. A.6 shows clearly that the amplitude of temperature fluctuations is very sensitive to the

mass flow rates of the two air injections, which determine directly the factor α and indirectly the pressure drop Δp of the cross-flow jets.

The amplitude of temperature fluctuations can then be optimized by maximizing α:

$$\alpha_{max} = \frac{1 - \sqrt{T_1/T_2}}{1 + \sqrt{T_1/T_2}} \quad \text{for} \quad \dot{m}_2/\dot{m}_1 = \sqrt{T_1/T_2} \tag{A.8}$$

In the experiments $T_1 \approx 290$ K and $T_2 \approx 390$ K, so the optimized injection condition is:

$$\dot{m}_2/\dot{m}_1 = 0.86 \quad \text{and} \quad \alpha_{max} = 0.07 \tag{A.9}$$

Combining Eq. A.6 with the perturbation equation for entropy fluctuations:

$$\frac{s'}{c_p} = \frac{T'}{T} - (\gamma - 1)\frac{p'}{\gamma p} \tag{A.10}$$

allows to write the transfer function H_{sp} at the zero-frequency limit, which writes:

$$H_{sp} = \frac{\hat{s}/c_p}{\hat{p}/\gamma p} = 1 - \gamma - \frac{\alpha}{2} \cdot \frac{\gamma p}{\Delta p} \tag{A.11}$$

With the specific heat ratio for air $\gamma = 1.4$, H_{sp} is negative real number, meaning that entropy wave is in opposition of phase with pressure wave in the TAFG system in the zero-frequency limit.

Appendix B

Mesh size adaptation for the jet by a 2D LES test

The objective here is to adapt the mesh size to the wall-law boundary condition on jet injection tube and to find a compromise with the computational cost. The previous work of Lapeyre (2015) has proved that the LES results are not sensitive to the grid size. However, in the modified version of the geometry with a subsonic jet, one should make sure that the present mesh is good enough to resolve the flow in the jet injection tube.

An evaluation of Reynolds number Re_D based on the bulk velocity U_b and the tube diameter $D = 4$ mm (see B.1) shows that the flow in the jet injection tube is highly turbulent.

$$Re_D = \frac{\rho U_b D}{\mu} = \frac{4\dot{m}}{\pi \mu D} = 8.8 \times 10^4 \tag{B.1}$$

It is too costly to resolve the turbulent boundary layer with the explicit LES code AVBP, which is the reason why the logarithmic law of wall has been implemented on the tube wall. Furthermore, one should make sure that the mesh size near the wall should be coarse enough to allow applying the wall function, but fine enough to resolve the flow. For a target y^+ equal to 100, the first mesh node near to the wall should be located at a normal distance y from the wall by definition:

$$y^+ = \frac{y \rho U_\tau}{\mu} \tag{B.2}$$

The friction velocity U_τ is by definition

$$U_\tau = \sqrt{\frac{\tau_w}{\rho}} \tag{B.3}$$

where the wall shear stress τ_w can be calculated from the wall friction factor C_f and the bulk velocity U_b of the pipe flow by:

$$\tau_w = \frac{1}{2} C_f \rho U_b^2 \tag{B.4}$$

For smooth pipes and $3,000 < Re_D < 100,000$, the skin friction factor C_f may be approximated by the Blasius correlation $C_f = 0.079 Re_D^{-0.25} = 4.6 \times 10^{-3}$, so that

$$\tau_w = 0.3 \times 10^3 \ kg/(m \cdot s^2), \quad U_\tau = 15.8 \ m/s, \quad y = 9.8 \times 10^{-5} \ m$$

Therefore if $y^+ = 100$ is expected, the mesh resolution near the jet injection tube should be about 0.1 mm. However, such mesh size would reduce the simulation time step to a quarter of the original one with a smallest mesh size of 0.4 mm. By the same estimation, if near wall mesh resolution is set to 0.4 mm, $y^+ = 400$ is expected, which is quite the limit of the log-law region of the wall function. Nevertheless, the main interest is to capture the aerodynamics of the jet, the choice of the mesh resolution 0.1 mm instead of 0.4 mm can be made if one sees large differences in the flow field from the simulations with both mesh resolutions. A 2D test has been done for this purpose.

The 2D domain (see Fig. B.1a)is composed of a 4×10 mm rectangle and a 32×135 mm rectangle, representing respectively the injection tube of the jet and the swirling tube of CESAM-HP. The dimensions have been slightly modified in order to scale the mesh size by integer factor. Two unstructured mesh grids are used for the test, having respectively a constant spatial resolution of 0.4 mm (see B.1b) and 0.1 mm in both X and Y directions. The numerical protocol used in these tests are the same as the LES of the entire domain except that the LES subgrid model is replaced by the dynamic Smagorinsky model.

The axial velocity profile along the y-direction from the mean solutions are traced in Fig. B.2 as a function of the reduced distance x/d with $d = 4$ mm being the the diameter of the jet orifice. On the dumping plane of the jet $x/d = 0$, the axial velocity is almost uniform. The axial velocity profile for the two meshes are similar both in shape and values. They also show well the expansion of the jet towards downstream and the recirculation zone due to confinement.

The evolution of the axial velocity along the revolution axis of the jet is illustrated in Fig. B.3. The axial velocity has been normalized by the value on $x/d = 0$. It is found that the center axial velocity decreases drastically with the jet expansion and reduces to half of the velocity on the discharge orifice around $x/d = 5$. The flow calculated from the two meshed in general match well with each other. So the 0.4 mm mesh resolution is retained for the sake of less computational cost.

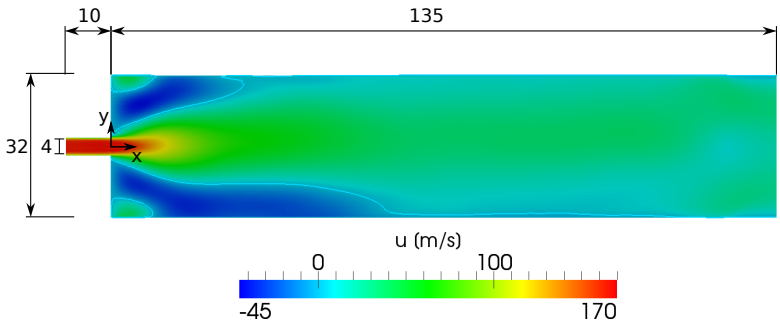

(a) 2D test computational domain superposed with the mean solution for axial velocity from the 0.4 mm mesh. Zero axial velocity is marked with the cyan line. Unit in mm.

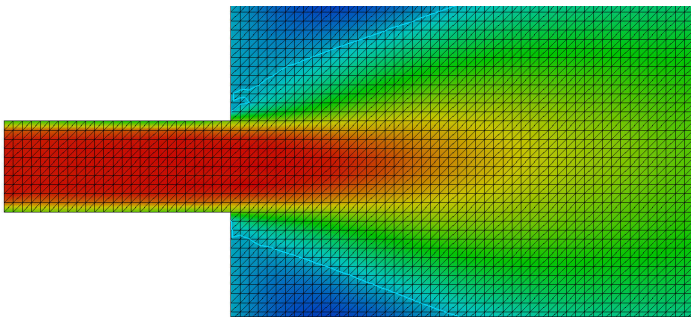

(b) Test mesh

Figure B.1: *Enlarged view of the 0.4 mm mesh for the 2D test of the jet*

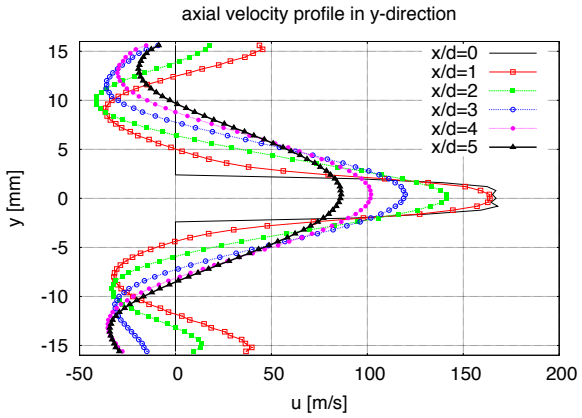

(a) 0.4 mm mesh

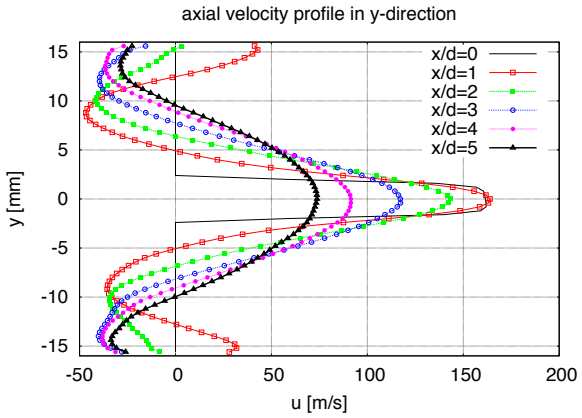

(b) 0.1 mm mesh

Figure B.2: *Axial velocity profile along y-direction*

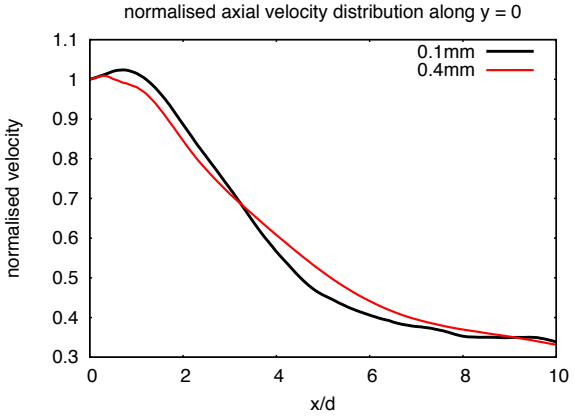

Figure B.3: *Axial velocity along jet center line*

Appendix C

Linear acoustic analysis the CESAM-HP burner

The acoustic eigenmodes of the CESAM-HP combustor are calculated analytically from simplified models and mean operational conditions of the combustor by assuming linear acoustics and no unsteady heat input in the burner $\dot{Q}' = 0$. The analysis is first conducted using a two-cavity model of the burner.

C.1 Two-cavity model

The burner is modelled by two cavities, with a cylindrical duct and square duct representing respectively the injector tube and the combustion chamber, as shown in Fig. C.1a. This model is also defined using boundary conditions associated with the ICS or the choked nozzle that are characterised either experimentally or theoretically.

The injector cavity has an inner diameter of 30 mm and a length of $L_p = 134.5$ mm. The chamber cavity has a square section of $70{\times}70$ mm^2 and a length of $L_c = 140$ mm. In both cavities flow quantities such as pressure p, velocity u and density ρ are decomposed into mean values and fluctuation values. The mean quantities are supposed to be constant since the flow Mach number in both of the cavities remains small, so only the fluctuating part are considered in the following analysis. In the low frequency range ($< 3\,000$ Hz), it is convenient to consider only the longitudinal planar waves so that the acoustic

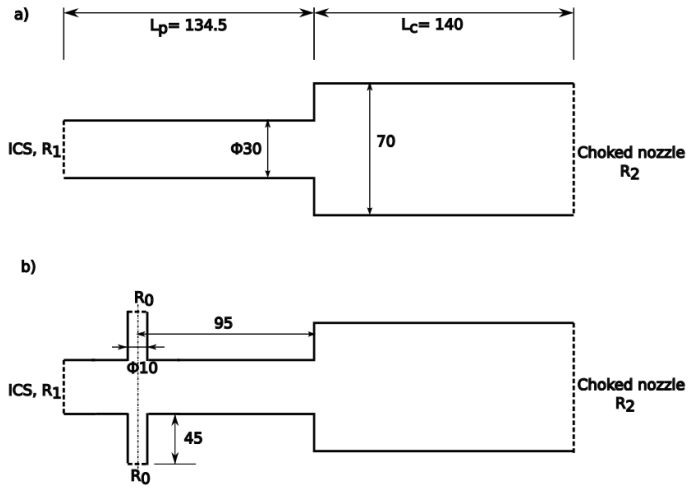

Figure C.1: *Model of th burner as a. two and b.five cavities. Unit in mm*

perturbations can be expressed by Fourier decomposition as:

$$\hat{p}_i = P_i^+ e^{+i\omega x/c_i} + P_i^- e^{-i\omega x/c_i}$$
$$\hat{u}_i = \frac{1}{\rho_i c_i}\left(P_i^+ e^{+i\omega x/c_i} - P_i^- e^{-i\omega x/c_i}\right)$$

where the subscript i stands for the cavity number, ρ_i and c_i are the mean gas density and sound velocity in the numbered cavity. The convention of $e^{-i\omega t}$ is used here.

On the front plane of the Impedance Control System (ICS), the reflection coefficient $R_1 = P_1^+/P_1^-$ is evaluated theoretically as a function of the Rayleigh conductivity K_R, as discussed in Sec. 5.3.4.2.

$$K_R = 2a\left(\frac{1}{\gamma - i\delta} + \frac{2}{\pi}\cdot\frac{h}{a}\right)^{-1}$$
$$\text{with} \quad \gamma - i\delta = 1 + \frac{1}{St}\cdot\frac{\frac{\pi}{2}I_1(St)e^{-St} - iK_1(St)\sinh(St)}{\frac{\pi}{2}I_1(St)e^{-St} + iK_1(St)\cosh(St)}$$
$$R_1 = \frac{ik_1d^2/K_R - i/tan(k_1L) + 1}{ik_1d^2/K_R - i/tan(k_1L) + 1} \tag{C.1}$$

In these expressions, a is the radius of perforated holes, d the spacing between the perforates and h the plate thicknes. St stands for the Strouhal number based on the bulk velocity of the jet formed through the aperture, and I_1 and K_1 are modified Bessel functions of first and second kind. $k = \omega/c_1$ is the wave number,and L the length of the resonance cavity of the ICS.

The wavelengths of the longitudinal acoustic waves are large enough compared with the length of junction of the two cavities, so the general Euler equations of

the flow lead to two jump conditions for the pressure and acoustic flux, shown in Eqs. (C.2)) and (C.3)). The conservation of acoustic flux in Eq. (C.3) has been established by assuming no unsteady heat input (Poinsot and Veynante 2005).

$$\hat{p}_1(x = L_p) = \hat{p}_2(x = 0) \tag{C.2}$$
$$S_1\hat{u}_1(x = L_p) = S_2\hat{u}_2(x = 0) \tag{C.3}$$

where $S_{1,2}$ designate the cross section area of the two cavities. As the length of converging part of the nozzle is also negligible compared to the wavelengths, the reflection coefficient R_2 on the entrance plane of the nozzle can be determined by the inlet flow Mach number M_2 when the nozzle is choked (Marble and Candel 1977):

$$R_2 = \frac{1 - \frac{1}{2}(\gamma - 1)M_2}{1 + \frac{1}{2}(\gamma - 1)M_2} \tag{C.4}$$

The characteristic waves $P_1^+, P_1^-, P_2^+, P_2^-$ must satisfy the Eqs. (C.1)-(C.4) and as the linear system given by these boundary and jump conditions features no source term, the determinant of this system must vanish to ensure non-trivial solutions. One obtain thus a dispersion relation (Eq. (C.5)) which gives the eigenmodes of the two-cavity model.

$$\begin{aligned}(1 + \Xi)\cdot[e^{-i(k_1L_p+k_2L_c)} - R_1R_2e^{i(k_1L_p+k_2L_c)}] \\ + (1 - \Xi) \cdot [R_1e^{i(k_1L_p-k_2L_c)} - R_2e^{-i(k_1L_p-k_2L_c)}] = 0\end{aligned} \tag{C.5}$$

where $\Xi = \frac{S_1/\rho_1c_1}{S_2/\rho_2c_2}$ indicates the acoustic coupling of the two cavities. Neglecting the mean pressure drop in the cavities one obtains $\Xi = \frac{S_1}{S_1}\sqrt{\frac{T_1}{T_2}}$ with T_1 and T_2 being the mean temperature in corresponding cavities.

C.2 Five-cavity model

As additional eigenmodes maybe introduced by the feeding lines (see for example in Richecoeur et al. (2013)), the linear acoustic analysis model is extended to five cavities, as shown in Fig. C.1b. The injector is split into two parts on the feeding line discharge plan. The two feeding line cavity with a diameter of 10 mm are identical and are located at 39.5 mm from the perforated plate.

The reflection coefficient R_0 at a radial distance of 60 mm from the injection tube axis is provided by a Pressurized Impedance Measurement System (PIMS), a device developed at EM2C laboratory that measures the acoustic impedance

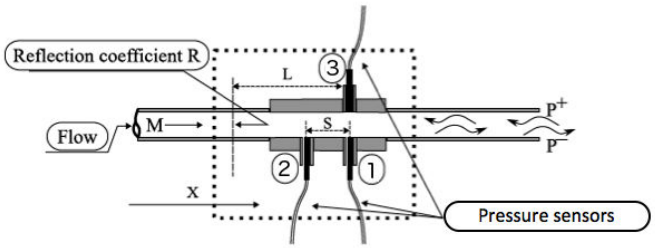

Figure C.2: *Schematic drawing of the Pressurized Impedance Measurement System (PIMS) adapted from Lamraoui et al. (2011).*

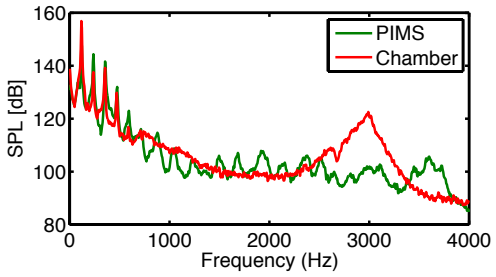

Figure C.3: *Sound pressure level measured by pressure sensors in PIMS and combustion chamber adapted from Mazur et al. (2015)*

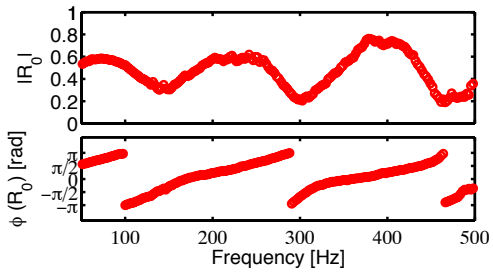

Figure C.4: *Reflection coefficient in the feeding line meausured at a radial distance of 60 mm from the injector axis.*

by the method of three microphones (Chung and Blaser 1980). A schematic drawing of the system is shown in Fig. C.2. Following a procedure originally proposed and validated in Lamraoui et al. (2011), the flame itself is used as an acoustic source and acoustic properties of the feeding lines are determined on-the-fly during hot fire tests. With this technique the measured reflection coefficient values are only reliable between 50 and 500 Hz. Beyond this range the coherence between the pressure sensors in the feeding line drops, limiting the use of the PIMS. Therefore the analysis of the 5-cavity model is also limited to this frequency range.

C.3 Results and discussion

The operating point chosen for validating the two- and five-cavity models is presented in Table C.1 with approximating mean conditions in the following: T_1 =600 K, T_2 = 1700 K and M_2 =0.02 at the entrance of the nozzle.

The sound pressure level measured by three pressure sensors located in the

Table C.1: *Chose operating point*

Property	Value
Name	op13-2-85
Tangential air flow rate m_a	13 g/s
Tangential fuel flow rate m_f	0.81 g/s
Axial air flow rate m_{ax}	2 g/s
Global equivalence ratio Φ	0.85
Power	37.5 kW
Mean chamber pressure	1.83 bar

Table C.2: *Summary of acoustic modes obtained experimentally and analytically with the two-cavity and five-cavity models*

n.	Exp	2-cavity		5-cavity	
	f_{peak}	f^n [Hz]	ω_i^n [rad/s]	f^n [Hz]	ω_i^n [rad/s]
1	116	-	-	92	-123
2	238	-	-	294	-129
3	354	-	-	384	-401.9
4	470	-	-	475	-225.5
5	582	-	-	-	-
6	2991	2954	-5.8	-	-

Table C.3: *Interpretation of acoustic modes*

n.	f [Hz]	Interpretation
1	116	Feeding line
2	238	Feeding line
3	354	Feeding line
4	470	Feeding line
5	582	Not identified, but likely from feeding line
6	2991	Half-wave mode in the combustion chamber

PIMS, the injector and the chamber respectively show several distinct peaks (see Fig. C.3). They are summarised in Table C.2 together with the eigenmodes calculated with the two- and five-cavity models. The imaginary part of the eigenmodes refers to the growth rate of each mode and it has a negative value as the model does not comprise any acoustic source.

Due to the wall-like boundaries at the inlet and outlet of the combustion chamber, the fundamental mode in the combustion chamber is supposed to be of half-wave type, so the first longitudinal mode in the chamebr is equal to 2951 Hz, which is close to that predicted by the two-cavity model and only about a 40 Hz lower than the experimental peak frequency n.86(Tab. C.2). Such difference is acceptable since the analytical value of this chamber mode is determined by the chamber cavity mean temperature T_2. Therefore f^6 is related to the combustion chamber.

The two-cavity model has allowed to identify the modes related to the combustion chamber, but the low frequencies (< 600 Hz) in Tab. C.2 remain unknown. While these peak frequencies disappear from the pressure sensors spectrum in non reacting cases, they are still present in the PIMS sensors. The five-cavity approach is then used in order to take the feeding lines into account. For this, the measured reflection coefficient in the feeding lines R_0 (see Fig. C.4) is first fitted by a tenth-order polynomial function in order to compute the dispersion relation. The found modes between 50 and 500 Hz seem to fit well the low frequency contents in the measurement signals. During the implementation it has also been found that these modes are largely influenced by the value of the reflection coefficient in the feeding line cavity R_0. And the It may be interesting to characterise the feeding lines experimentally with a more powerful and broadband acoustic source to see how they affect the injector and chamber modes in the five-cavity model.

Finally, Tab. C.3 summarizes the conclusions of the present investigation. Modes with frequencies higher than 500 Hz can be associated with the injector and the combustion chamber using a simple two-cavity model and an analytical representation of the perforated plate backed by a cavity with bias flow. For modes with lower frequencies it is necessary to take into account the feeding lines in a five-cavity model. Impedances measured in-situ on-the-fly using the flame as an acoustic source is necessary. In that case, only the modes associated with frequencies lower than 500 Hz can be retrieved due to a loss of coherence of the flame noise for higher frequencies.

References

Åbom, M. (1988). Error analysis of two-microphone measurements in ducts with flow. *The Journal of the Acoustical Society of America 83*(6), 2429. *(p. 47)*

Angelberger, C., D. Veynante, F. Egolfopoulos, and T. Poinsot (1998). Large eddy simulations of combustion instabilities in premixed flames. *Proceedinfs of the Summer Program 1998*, 61–82. *(p. 87)*

Bailly, C., C. Bogey, and S. Candel (2010). Modelling of sound generation by turbulent reacting flows. *International Journal of Aeroacoustics 9*(4), 461–490. *(p. 4, 5)*

Bake, F., C. Richter, B. Mühlbauer, N. Kings, I. Röhle, F. Thiele, and B. Noll (2009, oct). The Entropy Wave Generator (EWG): A reference case on entropy noise. *Journal of Sound and Vibration 326*(3-5), 574–598. *(p. 10)*

Bell, W., B. Daniel, and B. Zinn (1973). Experimental and theoretical determination of the admittances of a family of nozzles subjected to axial instabilities. *Journal of Sound and Vibration 30*(2), 179–190. *(p. 6)*

Bellucci, V., P. Flohr, C. O. Paschereit, and F. Magni (2004). On the Use of Helmholtz Resonators for Damping Acoustic Pulsations in Industrial Gas Turbines. *Journal of Engineering for Gas Turbines and Power 126*(2), 271. *(p. 88)*

Blacodon, D. (2009, mar). Combustion-Noise Characterization of a Turbofan Engine with a Spectral Estimation Method. *Journal of Propulsion and Power 25*(2), 374–379. *(p. 2)*

Bodony, D. J. (2009, sep). Scattering of an entropy disturbance into sound by a symmetric thin body. *Physics of Fluids 21*(9), 1–10. *(p. 39)*

Bogey, C., X. Gloerfelt, and C. Bailly (2003, may). Illustration of the Inclusion of Sound-Flow Interactions in Lighthill's Equation. *AIAA Journal 41*(8), 1604–1606. *(p. 4)*

Bushell, K. W. (1971). A survey of low velocity and coaxial jet noise with application to prediction. *Journal of Sound and Vibration 17*(2), 271–282. *(p. 2)*

Candel, Durox, Ducruix, Birbaud, Noiray, and Schuller (2009). Flame dynamics and combustion noise: progress and challenges. *International Journal of Aeroacoustics 8*(1), 1–56. *(p. 3, 4, 5, 6)*

Cerfacs (2008). *The AVBP HandBook*. *(p. 86, 87, 88)*

Charlette, F., C. Meneveau, and D. Veynante (2002, oct). A power-law flame wrinkling model for LES of premixed turbulent combustion Part I: non-dynamic formulation and initial tests. *Combustion and Flame 131*(1-2), 159–180. *(p. 87)*

Chu, B.-T. and L. S. G. Kovásznay (1958, mar). Non-linear interactions in a viscous heat-conducting compressible gas. *Journal of Fluid Mechanics 3*(05), 494. *(p. 6, 17)*

Chung, J. Y. and D. a. Blaser (1980, dec). Transfer function method of measuring in-duct acoustic properties. I. Theory. *Journal of the Acoustical Society of America 68*(3), 907–913. *(p. 45, 46, 142)*

Colin, O., A. Benkenida, and C. Angelberger (2003, jan). 3d Modeling of Mixing, Ignition and Combustion Phenomena in Highly Stratified Gasoline Engines. *Oil & Gas Science and Technology 58*(1), 47–62. *(p. 87)*

Colin, O. and M. Rudgyard (2000, aug). Development of High-Order Taylor–Galerkin Schemes for LES. *Journal of Computational Physics 162*(2), 338–371. *(p. 87)*

Crighton, D. G., A. P. Dowling, J. E. F. Williams, M. Heckl, and F. G. Leppington (1992). Thermoacoustic Sources and Instabilities. In *Modern Methods in Analytical Acoustics Lecture Notes*, pp. 378–405. London: Springer London. *(p. 3, 4, 5)*

Crocco, L. and S.-I. Cheng (1951). *Theory of combustion instability in liquid propellant rocket motors*, Volume 21. Cambridge Univ Press. *(p. 6)*

Culick, F. E. C. (2006). *Unsteady Motions in Combustion Chambers for Propulsion Systems*, Volume 323. *(p. 17)*

Cummings, A. (1986, apr). Transient and multiple frequency sound transmission through perforated plates at high amplitude. *The Journal of the Acoustical Society of America 79*(4), 942. *(p. 89)*

Cummings, A. and W. Eversman (1983, dec). High amplitude acoustic transmission through duct terminations: Theory. *Journal of Sound and Vibration 91*(4), 503–518. *(p. 89)*

Cumpsty, N. (1979, oct). Jet engine combustion noise: Pressure, entropy and vorticity perturbations produced by unsteady combustion or heat addition. *Journal of Sound and Vibration 66*(4), 527–544. *(p. 3, 6)*

Dobrzynski, W. (2010, may). Almost 40 Years of Airframe Noise Research: What Did We Achieve? *Journal of Aircraft 47*(2), 353–367. *(p. xiii, 1)*

Dowling, A. P. (1995, mar). The calculation of thermoacoustic oscillations. *Journal of Sound and Vibration 180*(4), 557–581. *(p. 8)*

Dowling, A. P. and Y. Mahmoudi (2015). Combustion noise. *Proceedings of the Combustion Institute 35*(1), 65–100. *(p. 3, 6)*

Dowling, P. and R. Stow (2003). Acoustic Analysis of Gas Turbine Combustors. *Journal of Propulsion and Power 19*(5), 751–764. *(p. 10)*

Ducruix, S., T. Schuller, D. Durox, and S. Candel (2003). Combustion Dynamics and Instabilities: Elementary Coupling and Driving Mechanisms.

Journal of Propulsion and Power 19(5), 722–734. *(p. 3)*

Durán, I. and S. Moreau (2013, apr). Solution of the quasi-one-dimensional linearized Euler equations using flow invariants and the Magnus expansion. *Journal of Fluid Mechanics 723*, 190–231. *(p. 8, 18, 19, 64)*

Durán, I., S. Moreau, and T. Poinsot (2013, jan). Analytical and Numerical Study of Combustion Noise Through a Subsonic Nozzle. *AIAA Journal 51*(1), 42–52. *(p. 10)*

Eckstein, J., E. Freitag, C. Hirsch, and T. Sattelmayer (2004). Experimental Study on the Role of Entropy Waves in Low-Frequency Oscillations for a Diffusion Burner. In *Volume 1: Turbo Expo 2004*, pp. 743–751. ASME. *(p. 9)*

Eckstein, J., E. Freitag, C. Hirsch, and T. Sattelmayer (2006). Experimental Study on the Role of Entropy Waves in Low-Frequency Oscillations in a RQL Combustor. *Journal of Engineering for Gas Turbines and Power 128*(April 2006), 264. *(p. 9)*

Enghardt, L. (2015). FLOCON: Adaptive and Passive Flow Control for Fan Broadband Noise Reduction. Selected Final Results. In *X-NOiSE/CEAS Wokrshop*. *(p. 2)*

Forney, L. J. and G. C. Fralick (1994). Two wire thermocouple: Frequency response in constant flow. *Review of Scientific Instruments 65*(10), 3252. *(p. 50)*

Forney, L. J. and G. C. Fralick (1995a). Multiwire thermocouples in reversing flow. *Review of Scientific Instruments 66*(10), 5050. *(p. 50)*

Forney, L. J. and G. C. Fralick (1995b). Three-wire thermocouple: Frequency response in constant flow. *Review of Scientific Instruments 66*(5), 3331. *(p. 49)*

Fritz, J., M. Kröner, and T. Sattelmayer (2004). Flashback in a Swirl Burner With Cylindrical Premixing Zone. *Journal of Engineering for Gas Turbines and Power 126*(2), 276. *(p. 101)*

Giauque, A., M. Huet, and F. Clero (2012). Analytical Analysis of Indirect Combustion Noise in Subcritical Nozzles. *Journal of Engineering for Gas Turbines and Power 134*(11), 111202. *(p. 7, 10, 18, 19, 64)*

Giauque, A., M. Huet, F. Clero, S. Ducruix, and F. Richecoeur (2013, aug). Thermoacoustic Shape Optimization of a Subsonic Nozzle. *Journal of Engineering for Gas Turbines and Power 135*(10), 102601. *(p. 7, 82)*

Goh, C. S. and A. S. Morgans (2011, jun). Phase prediction of the response of choked nozzles to entropy and acoustic disturbances. *Journal of Sound and Vibration 330*(21), 5184–5198. *(p. 8)*

Goh, C. S. and A. S. Morgans (2013, feb). The Influence of Entropy Waves on the Thermoacoustic Stability of a Model Combustor. *Combustion Science and Technology 185*(2), 249–268. *(p. 9)*

Groeneweg, J. F., T. G. Sofrin, E. J. Rice, and P. R. Gliebe (1991). Turbomachinery Noise. *Aeroacoustics of Flight Vehicles: Theory and Practice, Vol. 1: Noise Sources 1*, 151–209. *(p. 1)*

Hatch, M. S., W. A. Sowa, G. S. Samulersen, and J. D. Holdeman (1995, may). Geometry and flow influences on jet mixing in a cylindrical duct. *Journal of Propulsion and Power 11*(3), 393–402. *(p. 36)*

Hield, P. A. and M. J. Brear (2008). Comparison of Open and Choked Premixed Combustor Exits During Thermoacoustic Limit Cycle. *AIAA Journal 46*(2), 517–526. *(p. 11)*

Hill, S. J., G. J. Nathan, and R. E. Luxton (1995). Precession in axisymmetric confined jets. *Twelfth Australasian Fluid Mechanics Conference*, 135 – 138. *(p. 102)*

Holdeman, J. D. (1993, jan). Mixing of multiple jets with a confined subsonic crossflow. *Progress in Energy and Combustion Science 19*(1), 31–70. *(p. 36)*

Holdeman, J. D., D. S. Liscinsky, G. S. Samuelsen, V. L. Oechsle, and C. E. Smith (1996, jun). Mixing of Multiple Jets With a Confined Subsonic Crossflow in a Cylindrical Duct. In *Volume 3: Coal, Biomass and Alternative Fuels; Combustion and Fuels; Oil and Gas Applications; Cycle Innovations*, Volume 3, pp. V003T06A049. ASME. *(p. 36)*

Howe, M. (1979). On the theory of unsteady high Reynolds number flow through a circular aperture. *Proceedings of the Royal Society of London. Series A 366*(1725), 205–223. *(p. 88, 89)*

Howe, M. (1997). Influence of Wall Thickness on Rayleigh Conductivity and Flow-Induced Aperture Tones. *Journal of Fluids and Structures 11*(4), 351–366. *(p. 88)*

Howe, M. S. (1998). *Acoustics of Fluid–Structure Interactions*. Cambridge: Cambridge University Press. *(p. 3, 5)*

Howe, M. S. (2003). *Theory of Vortex Sound*. *(p. 7)*

Howe, M. S. (2010). Indirect combustion noise. *Journal of Fluid Mechanics 659*, 267–288. *(p. 5, 7)*

Huang, Y. and V. Yang (2009, aug). Dynamics and stability of lean-premixed swirl-stabilized combustion. *Progress in Energy and Combustion Science 35*(4), 293–364. *(p. 3, 97)*

Huet, M. and A. Giauque (2013, sep). A nonlinear model for indirect combustion noise through a compact nozzle. *Journal of Fluid Mechanics 733*, 268–301. *(p. 8, 64)*

Hughes, I. J. and A. P. Dowling (1990, sep). The absorption of sound by perforated linings. *Journal of Fluid Mechanics 218*(-1), 299. *(p. 88, 89, 90)*

Hulshoff, S. J., A. Hirschberg, and G. C. J. Hofmans (2001, jul). Sound production of vortex–nozzle interactions. *Journal of Fluid Mechanics 439*, 335–352. *(p. 7)*

Hung, P. C., G. Irwin, R. Kee, and S. McLoone (2005). Difference equation approach to two-thermocouple sensor characterization in constant velocity flow environments. *Review of Scientific Instruments 76*(2), 1–10. *(p. 51)*

Ingard, U. and H. Ising (1967). Acoustic Nonlinearity of an Orifice. *The Journal of the Acoustical Society of America 42*(1), 6. *(p. 90)*

Jing, X. and X. Sun (2000, sep). Effect of Plate Thickness on Impedance of Perforated Plates with Bias Flow. *AIAA Journal 38*(9), 1573–1578. *(p. 89)*

Jovanović, M. R., P. J. Schmid, and J. W. Nichols (2014, feb). Sparsity-promoting dynamic mode decomposition. *Physics of Fluids 26*(2), 024103. *(p. 108)*

Kar, K., S. Roberts, R. Stone, M. Oldfield, and B. French (2004, mar). Instantaneous Exhaust Temperature Measurements Using Thermocouple Compensation Techniques. *(p. 48)*

Kings, N., K. Knobloch, L. Enghardt, and F. Bake (2011). Indirect combustion noise : Experimental investigation of the vortex sound generation mechanism. *17th AIAA/CEAS Aeroacoustics Conference, Portland, OR* (June), 5–8. *(p. 7)*

Kings, N., W. Tao, M. Mazur, P. Scouflaire, F. Richecoeur, and S. Ducruix (2015). Experimental and numerical investigation on combustion noise sources in a model gas turbine combustor. In *X-NOISE/CEAS Wokrshop*. *(p. 115)*

Kings, N., W. Tao, P. Scouflaire, F. Richecoeur, and S. Ducruix (2016). Experimental and numerical investigation of direct and indirect combustion noise constributions in a leam premixed laboratory swirled combustor. In *Proceedings of ASME Turbo Expo 2016*. *(p. 115)*

Kroll, J. T., W. A. Sowa, G. S. Samuelsen, and J. D. Holdeman (2000, nov). Optimization of Orifice Geometry for Crossflow Mixing in a Cylindrical Duct. *Journal of Propulsion and Power 16*(6), 929–938. *(p. 36)*

Kröner, M., J. Fritz, and T. Sattelmayer (2003). Flashback Limits for Combustion Induced Vortex Breakdown in a Swirl Burner. *Journal of Engineering for Gas Turbines and Power 125*(3), 693. *(p. 101)*

Lamraoui, A., F. Richecoeur, T. Schuller, and S. Ducruix (2011). A Methodology for On the Fly Acoustic Characterization of the Feeding Line Impedances in a Turbulent Swirled Combustor. *Journal of Engineering for Gas Turbines and Power 133*(1), 011504. *(p. xviii, 142)*

Lapeyre, C. (2015). *Numerical study of flame stability, stabilization and noise in a swirl-stabilized combustor under choked conditions*. Ph. D. thesis. *(p. 84, 135)*

Lapeyre, C., M. Mazur, F. Scouflaire, Philippe Richecœur, S. Ducruix, and T. Poinsot (2015). Acoustically induced vortex core flashback in a staged swirl-stabilized combustor. *(p. 106)*

Lee, S. K., P. V. Lanspeary, and G. J. Nathan (2007). Strouhal Number of Naturally-Oscillating Triangular and Circular Jets Water in transducer. *16th Australasian Fluid Mechanics Conference* (December), 447–450. *(p. 102)*

Lefebvre, A. H. (1977). Lean premixed/prevaporized combustion. *Paper No.*

NASA CP-2016. *(p. 3)*

Legier, J. P., T. Poinsot, and D. Veynante (2000). Dynamically thickened flame LES model for premixed and non-premixed turbulent combustion. *Proceedings of the Summer Program*, 157–168. *(p. 87)*

Leitgeb, T., T. Schuller, D. Durox, F. Giuliani, S. Köberl, and J. Woisetschläger (2013, mar). Interferometric determination of heat release rate in a pulsated flame. *Combustion and Flame 160*(3), 589–600. *(p. 115)*

Levine, H. and J. Schwinger (1948). On the radiation of sound from an unflanged circular pipe. *Physical Review 73*(4), 383–406. *(p. 24, 25, 33)*

Leyko, M., S. Moreau, F. Nicoud, and T. Poinsot (2011, aug). Numerical and analytical modelling of entropy noise in a supersonic nozzle with a shock. *Journal of Sound and Vibration 330*(16), 3944–3958. *(p. 21)*

Leyko, M., F. Nicoud, S. Moreau, and T. Poinsot (2009, jun). Numerical and analytical investigation of the indirect combustion noise in a nozzle. *Comptes Rendus Mécanique 337*(6-7), 415–425. *(p. 10, 21)*

Lieuwen, T. and J. H. Cho (2005, jan). Coherent acoustic wave amplification/damping by wrinkled flames. *Journal of Sound and Vibration 279*(3-5), 669–686. *(p. 5)*

Lieuwen, T. C. (2012). Overview and basic equations. In *Unsteady Combustor Physics*, Chapter 1. Cambridge Univ Press. *(p. 5)*

Lighthill, M. J. (1952, mar). On Sound Generated Aerodynamically. I. General Theory. *Proceedings of the Royal Society A: Mathematical, Physical and Engineering Sciences 211*(1107), 564–587. *(p. 4, 5)*

Lilley, G. M., H. E. Plumblee, W. C. Strahle, S.-Y. Ruo, and P. E. Doak (1972, jul). The Generation and Radiation of Supersonic Jet Noise. Volume IV. Theory of Turbulence Generated Jet Noise, Noise Radiation from Upstream Sources, and Combustion Noise. *(p. 5)*

Lucca-Negro, O. and T. O'Doherty (2001, jan). Vortex breakdown: a review. *Progress in Energy and Combustion Science 27*(4), 431–481. *(p. 101)*

Luong, T., M. Howe, and R. McGowan (2005, dec). On the Rayleigh conductivity of a bias-flow aperture. *Journal of Fluids and Structures 21*(8), 769–778. *(p. 89)*

Marble, F. and S. Candel (1977). Acoustic disturbance from gas nonuniformities convected through a nozzle. *Journal of Sound and Vibration 55*(2), 225–243. *(p. 6, 7, 18, 19, 20, 21, 22, 24, 64, 141)*

Mazur, M., W. Tao, P. Scouflaire, F. Richecoeur, and S. Ducruix (2015, jun). Experimental and Analytical Study of the Acoustic Properties of a Gas Turbine Model Combustor With a Choked Nozzle. In *Volume 4B: Combustion, Fuels and Emissions*, pp. V04BT04A001. ASME. *(p. xviii, 81, 142)*

Melling, T. (1973). The acoustic impendance of perforates at medium and high sound pressure levels. *Journal of Sound and Vibration 29*(1), 1–65. *(p. 90)*

Mendez, S. and J. Eldredge (2009). Acoustic modeling of perforated plates with bias flow for Large-Eddy Simulations. *Journal of Computational Physics 228*(13), 4757–4772. *(p. 88)*

Mi, J. and G. Nathan (2004). Self-excited jet-precession Strouhal number and its influence on downstream mixing field. *Journal of Fluids and Structures 19*(6), 851–862. *(p. 102)*

Miles, J. H. (2010). Core Noise Diagnostics of Turbofan Engine Noise Using Correlation and Coherence Functions. *Journal of Propulsion and Power 26*(2), 303–316. *(p. 2)*

Mishra, A. and D. J. Bodony (2013, feb). Evaluation of actuator disk theory for predicting indirect combustion noise. *Journal of Sound and Vibration 332*(4), 821–838. *(p. 6)*

Moase, W. H., M. J. Brear, and C. Manzie (2007, aug). The forced response of choked nozzles and supersonic diffusers. *Journal of Fluid Mechanics 585*, 281. *(p. 6, 7, 8, 18, 21, 64)*

Morse, P. M. and K. U. Ingard (1970). *Theoretical Acoustics*, Volume 38. *(p. 24)*

Motheau, E., F. Nicoud, and T. Poinsot (2014, may). Mixed acoustic–entropy combustion instabilities in gas turbines. *Journal of Fluid Mechanics 749*, 542–576. *(p. 9)*

Moureau, V., G. Lartigue, Y. Sommerer, C. Angelberger, O. Colin, and T. Poinsot (2005, jan). Numerical methods for unsteady compressible multi-component reacting flows on fixed and moving grids. *Journal of Computational Physics 202*(2), 710–736. *(p. 86)*

Muthukrishnan, M., W. C. Strahle, and D. H. Neale (1978, apr). Separation of Hydrodynamic, Entropy, and Combustion Noise in a Gas Turbine Combustor. *AIAA Journal 16*(4), 320–327. *(p. 10)*

Nathan, G. J., S. J. Hill, and R. E. Luxton (1998). An axisymmetric 'fluidic' nozzle to generate jet precession. *Journal of Fluid Mechanics 370*, 347–380. *(p. 102)*

Ni, R.-H. (1982, nov). A Multiple-Grid Scheme for Solving the Euler Equations. *AIAA Journal 20*(11), 1565–1571. *(p. 87)*

Nicoud, F. and T. Poinsot (1998). Wall-Adapting Local Eddy-Viscosity models for simulations in complex geometries. In *6th ICFD Conference on numerical Methods for Fluid Dynamics*, pp. 1–7. *(p. 86)*

Nicoud, F., H. B. Toda, O. Cabrit, S. Bose, and J. Lee (2011, aug). Using singular values to build a subgrid-scale model for large eddy simulations. *Physics of Fluids 23*(8), 085106. *(p. 86)*

Nomura, Y., I. Yamamura, and S. Inawashiro (1960, mar). On the Acoustic Radiation from a Flanged Circular Pipe [Nomura, Yamamura, Inawashiro].pdf. *Journal of Physical Society of Japan 15*(3), 510–517. *(p. 24)*

O'Reilly, P. G., R. J. Kee, R. Fleck, and P. T. McEntee (2001). Two-wire thermocouples: A nonlinear state estimation approach to temperature

reconstruction. *Review of Scientific Instruments 72*(8), 3449. *(p. 51, 56)*

Peters, M. C. A. M., A. Hirschberg, A. J. Reijnen, and A. P. J. Wijnands (1993). Damping and reflection coefficient measurements for an open pipe at low Mach and low Helmholtz numbers. *Journal of Fluid Mechanics 256*(-1), 499. *(p. 33)*

Phillips, O. M. (1960, sep). On the generation of sound by supersonic turbulent shear layers. *Journal of Fluid Mechanics 9*(01), 1. *(p. 5)*

Poinsot, T. and S. Lele (1992, jul). Boundary conditions for direct simulations of compressible viscous flows. *Journal of Computational Physics 101*(1), 104–129. *(p. 87)*

Poinsot, T. and D. Veynante (2005). *Theoretical and Numerical Combustion*, Volume 2005. *(p. xv, 5, 8, 17, 79, 80, 81, 87, 141)*

Price, R., I. Hurle, and T. Sugden (1969, jan). Optical studies of the generation of noise in turbulent flames. *Symposium (International) on Combustion 12*(1), 1093–1102. *(p. 4)*

Richecoeur, F., T. Schuller, A. Lamraoui, and S. Ducruix (2013, jan). Analytical and experimental investigations of gas turbine model combustor acoustics operated at atmospheric pressure. *Comptes Rendus Mécanique 341*(1-2), 141–151. *(p. 141)*

Rienstra, S. and A. Hirschberg (2013). *An Introduction to Acoustics*. *(p. 24)*

Savitzky, A. and M. J. E. Golay (1964, jul). Smoothing and Differentiation of Data by Simplified Least Squares Procedures. *Analytical Chemistry 36*(8), 1627–1639. *(p. 54)*

Scarpato, A., N. Tran, S. Ducruix, and T. Schuller (2012, jan). Modeling the damping properties of perforated screens traversed by a bias flow and backed by a cavity at low Strouhal number. *Journal of Sound and Vibration 331*(2), 276–290. *(p. 82)*

Schmid, P. J. (2010, aug). Dynamic mode decomposition of numerical and experimental data. *Journal of Fluid Mechanics 656*, 5–28. *(p. 108, 109)*

Schmid, P. J. (2011, apr). Application of the dynamic mode decomposition to experimental data. *Experiments in Fluids 50*(4), 1123–1130. *(p. 108)*

Schmid, P. J., L. Li, M. P. Juniper, and O. Pust (2011, jun). Applications of the dynamic mode decomposition. *Theoretical and Computational Fluid Dynamics 25*(1-4), 249–259. *(p. 108)*

Schönfeld, T. and M. Rudgyard (1999, nov). Steady and Unsteady Flow Simulations Using the Hybrid Flow Solver AVBP. *AIAA Journal 37*(11), 1378–1385. *(p. 86)*

Sensiau, C. (2013). Investigation of combustion noise on Snecma turbofans. In *Seminar on Combustion Noise-Scientific Days Onera*. *(p. xiii, 2)*

Sheen, H., W. Chen, S. Jeng, and T. Huang (1996, may). Correlation of swirl number for a radial-type swirl generator. *Experimental Thermal and Fluid Science 12*(4), 444–451. *(p. 98)*

Shivashankara, B., W. Strahle, and J. Handley (1974, jan). An evaluation of combustion noise scaling laws by an optical technique. In *12th Aerospace*

Sciences Meeting, Volume 13, Reston, Virigina, pp. 623–627. American Institute of Aeronautics and Astronautics. *(p. 4)*

Sisco, J., Y. Yu, V. Sankaran, and W. Anderson (2011). Examination of mode shapes in an unstable model combustor. *Journal of Sound and Vibration 330*(1), 61–74. *(p. 8)*

Smagorinsky, J. (1963, mar). General Circulation Experiments With the Primitive Equations. *Monthly Weather Review 91*(3), 99–164. *(p. 86)*

Smith, T. J. B. and J. K. Kilham (1963, may). Noise Generation by Open Turbulent Flames. *The Journal of the Acoustical Society of America 35*(5), 715–724. *(p. 4)*

Stow, S. R., A. P. Dowling, and T. P. Hynes (2002, sep). Reflection of circumferential modes in a choked nozzle. *Journal of Fluid Mechanics 467*(x), 215–239. *(p. 7)*

Strahle, W. C. (1978). Combustion noise. *Progress in Energy and Combustion Science 4*(3), 157–176. *(p. 3, 4, 6)*

Strahle, W. C. and M. Muthukrishnan (1976, nov). Thermocouple time constant measurement by cross power spectra. *AIAA Journal 14*(11), 1642–1644. *(p. 50)*

Syred, N. and J. Beér (1974, oct). Combustion in swirling flows: A review. *Combustion and Flame 23*(2), 143–201. *(p. 101)*

Tagawa, M. and Y. Ohta (1997, jun). Two-thermocouple probe for fluctuating temperature measurement in combustion—Rational estimation of mean and fluctuating time constants. *Combustion and Flame 109*(4), 549–560. *(p. 51)*

Tagawa, M., T. Shimoji, and Y. Ohta (1998). A two-thermocouple probe technique for estimating thermocouple time constants in flows with combustion: In situ parameter identification of a first-order lag system. *Review of Scientific Instruments 69*(9), 3370. *(p. 51)*

Taine, J. and E. Iacona (2011). *A first course in heat transfer*. Dunod. *(p. 49)*

Thomas, a. and G. T. Williams (1966, oct). Flame Noise: Sound Emission from Spark-Ignited Bubbles of Combustible Gas. *Proceedings of the Royal Society of London. Series A, Mathematical and Physical Sciences 294*(1439), 449–466. *(p. 4)*

Tran, N. (2009). *Influence of inlet acoustic boundary condition on large amplitude combustion instabilities : design of a robust impedance control system*. Ph. D. thesis, Ecole Centrale Paris. *(p. 91)*

Tran, N., S. Ducruix, and T. Schuller (2009a). Damping combustion instabilities with perforates at the premixer inlet of a swirled burner. *Proceedings of the Combustion Institute 32*(2), 2917–2924. *(p. 82)*

Tran, N., S. Ducruix, and T. Schuller (2009b). Passive Control of the Inlet Acoustic Boundary of a Swirled Burner at High Amplitude Combustion Instabilities. *Journal of Engineering for Gas Turbines and Power 131*(5), 51502. *(p. 82, 88)*

Truffaut, J.-M., G. Searby, and L. Boyer (1998, dec). Sound emission by

non-isomolar combustion at low Mach numbers. *Combustion Theory and Modelling 2*(4), 423–428. *(p. 5)*

Truffin, K. and T. Poinsot (2005, sep). Comparison and extension of methods for acoustic identification of burners. *Combustion and Flame 142*(4), 388–400. *(p. 3)*

Tsien, H. S. (1952). The Transfer Functions of Rocket Nozzles. *Journal of the American Rocket Society*, 139–143. *(p. 6, 7, 18)*

Vranos, A., D. Liscinsky, B. True, and J. Holdeman (1991). Experimental study of cross-stream mixing in a cylindrical duct. *AIAA*. *(p. 36)*

Yang, V. and W. E. Anderson (2008). *Liquid Rocket Engine Combustion Instability*. *(p. 8, 17)*

Yu, Y. C., J. C. Sisco, V. Sankaran, and W. E. Anderson (2010, jun). Effects of Mean Flow, Entropy Waves, and Boundary Conditions on Longitudinal Combustion Instability. *Combustion Science and Technology 182*(7), 739–776. *(p. 8)*

Zhu, M., A. Dowling, and K. N. C. Bray (2001). Self-Excited Oscillations in Combustors With Spray Atomizers. *Journal of Engineering for Gas Turbines and Power 123*(4), 779. *(p. 9)*

Zukoski, E. E. and J. M. Auerbach (1976). Experiments concerning the response of supersonic nozzles to fluctuating inlet conditions. *Journal of Engineering for Power* (75), 60–64. *(p. 10)*

ÉCOLE DOCTORALE
Sciences mécaniques et énergétiques, matériaux et géosciences (SMEMAG)

Titre: Méthodologie pour la séparation du bruit direct et indirect de combustion basée sur les mesures de température et de pression résolues dans le temps

Mots-clés: Bruit de combustion, onde d'entropie, bruit de combustion indirect, fonction transfert d'une tuyère

Résumé: L'objectif de la thèse est le développement d'une stratégie pour quantifier expérimentalement le bruit indirect et le séparer du bruit direct, puisque le bruit direct et indirect co-existent dans la plupart des applications. La configuration retenue pour l'étude est un banc expérimental avec une tuyère et la stratégie proposée a pour l'objectif de mesurer les fonctions de transfert de la tuyère. Le premier chapitre définit les fonctions de transfert de la tuyère utilisée dans l'étude comme référence pour la validation de la stratégie. Le deuxième chapitre présente une configuration originale qui génère simultanément le bruit direct et indirect sans introduire la combustion. Le troisième chapitre détaille les méthodes pour évaluer les ondes acoustiques et d'entropie à partir des mesures de température et de pression. Le quatrième chapitre termine la première partie de la thèse en décrivant la stratégie avant de la tester avec les signaux expérimentaux et numériques de haute fidélité. La deuxième partie se concentre sur l'utilisation de la stratégie dans les simulations à grandes échelles d'un brûleur à combustion turbulente. Les simulations sont validées par des données expérimentales tandis que les signaux sont traités à quantifier le bruit direct et indirect de combustion dans la chambre.

Title: Time resolved temperature and pressure based methodology for direct and indirect combustion noise separation

Keywords: combustion noise, entropy wave, indirect combustion noise, nozzle transfer functions

Abstract: The objective of the thesis is the development of a practical strategy to quantify experimentally indirect noise and to discriminate it from direct noise as they co-exist in most practical conditions. The configuration retained for the study is a test bench with a nozzle and the proposed the strategy relies on nozzle transfer functions. The first chapter defines the nozzle transfer functions used in the study as references for the validation of the strategy. The second chapter introduces an original setup that generates simultaneously direct and indirect noise without handling combustion. The third chapter details the methods to evaluate the acoustic and entropy waves from raw temperature and pressure signals. The fourth chapter closes the first part of the study by describing the strategy then testing it on high-fidelity simulation and experimental signals. The second part focuses on the use of the strategy in Large Eddy Simulations of a turbulent combustion test bench. Simulations are validated by experimental data then raw signals are processed to quantify the direct and indirect noise sources as well as the direct and indirect noise contributions.